Immunogenic signaling in lung cancer in response to ionizing radiation

Protocol development and optimization

Martine Dorthea Engelhardt-Olsen Ruud

Thesis for the Degree of

Master of Science

Department of Physics

Faculty of Mathematics and Natural Sciences

University of Oslo

December 2020

2020

Immunogenic signaling in lung cancer in response to ionizing radiation

http://www.duo.uio.no

Trykk: Reprosentralen, Universitetet i Oslo

Acknowledgement

The work presented in this thesis was carried out at the section for Biophysics and Medical physics at the Department of Physics, University of Oslo.

First, I would like to thank my supervisor Nina F. Jeppesen Edin. Thank you for always being straight to the point, and never letting me win at badminton. I have never met anyone with such an enthusiasm for her field of research as you, which has been a true inspiration during my time at the University of Oslo.

Second, thank you to my supervisors Eirik Malinen, Ingunn Hanson, and Anne Marit Rykkelid. Julia Marzioch and Stefan Schrunner also deserves a thank you. Einar Sagstuen, thank you for welcoming me to the department early on, and a huge thank you to Eli O. Hole for always keeping her office door open when I needed someone to talk to. I am truly grateful for all the help I have received, without it, none of this would have been possible.

A huge thank you to Live Wang Jensen for keeping me company during my years at the University of Oslo. Also, the biggest thank you to Marte Julie Sætra for being my inspiration and lending me all of her books. I would also like to thank my family for the support during these years.

Finally, I want to thank Haakon for all you have done for me, and for all that you are to me.

Dedication

This master thesis is dedicated to my mom. You inspired me every day of your life and will continue to do so for the rest of my life.

Abstract

Radiation therapy has for decades been used as palliative and curative treatment method for cancer. In later years, immunotherapy has established itself as the fourth pillar of cancer treatment. As a part of malignant development of a tumor, immunoevasive cancer cells are selected which are not targeted by the host immune system. A part of this mechanism is acquisition of low immunogenicity, which means that cancer cells are able to hide from the immunosurveillance. In later years however, an immunostimulatory form of cell death involving pre-mortem emission of damage-associated molecular patterns (DAMPs) called immunogenic cell death (ICD) has been linked to the induction of an anti-tumor immune response. DAMPs function as an "eat me"-signal for the immune system, which in turn can make the immune system recognize the cancer cells as foreign. One such DAMP is the membrane bound protein calreticulin after translocation from the endoplasmatic reticulum in response to ionizing radiation. The benefit of cell membrane-bound calreticulin is that it can lead to increased sensitivity to cytotoxic T-lymphocyte killing of tumor cells. We thus want to use radiation to induce immunogenic response in cells to make the immune system target and kill cancer cells, which could improve the outcome of the cancer patients.

Another response to ionizing radiation which potentially stimulates an immune response, is the formation of micronuclei in cells following ionizing radiation. Micronuclei, which are extra-cellular bodies containing damaged chromosome fragments, can be detected by the cytosolic DNA sensor cyclic GMP-AMP synthase (cGAS) resulting in activation of an immune response.

This thesis aimed to measure the membrane bound calreticulin and the formation of micronuclei in A549 cells (human lung carcinoma) after ionizing radiation. The cells were irradiated with X-rays, varying the dose from 2 Gy – 16 Gy. The samples were analyzed 48- and 24-hours after irradiation respectively, using flow cytometry to measure the membrane bound calreticulin and confocal microscopy to analyze the micronuclei.

For both experiments it turned out that protocol development was necessary to obtain experimental data. A major part of this thesis is therefore protocol development. The other half is obtaining experimental data using X-ray radiation to measure the level of membrane bound calreticulin after ionizing radiation. The experimental data from the membrane bound calreticulin measurement shows that autofluorescence will occur when using flow cytometry

to analyze the A549 cells after the calreticulin assay because the cells are not fixated. Therefore, the experimental calreticulin data obtained in this thesis were corrected for autofluorescence and can be regarded as highly reliable. Due to time constraints, no experimental data for the micronuclei assay were obtained.

It was also found that A549 cells have an increase in the membrane bound calreticulin in response to X-ray radiation following 2 Gy – 16 Gy, given as both one fraction and two fractions. Our data indicate that the membrane bound calreticulin expression in A549 cells is dose dependent with a threshold dose for induction and another for saturation. In addition, two experiments giving T98G cells (human glioblastoma) 8 Gy X-ray irradiation as one fraction were run. No increase in the membrane bound calreticulin could be seen for the T98G cells.

Table of Contents

Abbreviations

A

ATP: adenosine triphosphate · 35

AU: Airy Units · 50

B

balanced salt solution: BSS · 52

base pairs: bp · 39

bovine serum albumin: BSA · 62

C

Cdks: cyclin-dependent protein kinases · 26

CE: Compton scattering · 12

CellBrite 488: CellBrite · 68

CLSM: confocal laser scanning microscope · 49

CS: compton scattering · 12

cyclic GMP-AMP: cGAMP · 39

Cytochalasin B: Cyt-b · 58

cytochalasin-B: Cyt-B · 41

cytokinesis-block micronucleus: CBMN · 41

D

DAMP: damage associated molecular pattern · 35

Deoxyribonucleic acid: DNA · 2

DNA: deoxyribonucleic acid · 18

DOF: depth of field · 48

double-stranded DNA: dsDNA · 2

DSB: double strand break · 31

Dulbecco’s Modified Eagle’s Medium: DMEM · 52

DyLight Alexa Fluor 488: DyLgiht · 88

E

endoplasmatic reticulum: ER · 20

S

SNR: signal-to-noise ratio · 49

SSB: single strand break · 31

SSC: sideways scatter · 46

Stimulator of Interferon Genes: STING · 39

T

The International Atomic Energy Agency: IAEA · 44

the mitotic phase: M phase · 22

Type I interferon: IFN · 2

U

University of Oslo: UiO · 51

1 Introduction

Already in 1950, two independent studies conducted by Doll and Hill (Doll and Hill, 1950), and Wynder and Graham (Wynder and Graham, 2005) reportedly found a link between smoking and lung cancer. Today it is known that smoking can induce lung cancer, and eight out of ten lung cancer cases are linked to smoking in Norway (Kreftregisteret, 03.03.2020). In Norway alone, 3351 new cases of lung cancer was reported in 2017 and lung cancer stood for almost 20 % of cancer deaths (Kreftregisteret, 03.03.2020). Also, patients with cancer of the lung, pancreas, and brain are most likely to die of their cancer (Zaorsky et al., 2017). The high number of mortalities has proven that treating and curing lung cancer is difficult, and better treatment options are needed.

One way to treat cancer is by using radiotherapy, a clinical modality using ionizing radiations to treat malignant neoplasias as well as benign diseases (Mehta et al., 2010). Radiotherapy has been used as a local tumor treatment in addition to being the most commonly used cancer treatment strategy today (Rodríguez-Ruiz et al., 2018). Approximately 60 % of patients with solid tumors that receive either curative or palliative cancer treatment will receive radiation as a part of their cancer treatment (Carvalho and Villar, 2018). When using radiotherapy, the occurrence of systemic antitumor effects manifesting as regression of tumors outside of the irradiated field, so-called abscopal effect, has occasionally been observed. However, between 1969 and 2014, only 46 cases of abscopal effect has been reported (Rodríguez-Ruiz et al., 2018). Only recently, the abscopal effect has been connected to the induction of immunogenicity resulting in a tumor immune response to irradiation (Ko et al., 2018).

Today, immunotherapy has established itself as the fourth pillar of cancer treatment but only a minority of cancer patients benefits from immunotherapy (Dobosz and Dzieciątkowski, 2019). It is believed that the patients who benefits from immunotherapy are those who already have an immunogenic tumor signature possibly through a high mutation rate, which allows the immune system to recognize the cancer cells.

The problem using immunotherapy is to make the body recognize the cancer cells as foreign (non-self) as the immune system is trained not to respond to self-molecules in order to avoid autoimmunity (Houghton and Guevara-Patiño, 2004). Using radiation to induce an immunogenic response in cells to make the immune system recognize the cancer cells as non-self could improve the outcome of immunotherapy. In fact, several investigations have reported the use of radiotherapy as an inducer of immunogenic cell death (ICD) (Huang et al., 2019). When ICD occurs, there will be a release of damage-associated molecular patterns (DAMPs) with potential to induce adaptive immune responses. These DAMPs have predominantly non-immunological functions inside the cell before their exposure on the cell surface or their secretion (Krysko et al., 2012). DAMPs can function as either adjuvant or danger signals for the immune system. Some DAMPs, such as cell surface-exposed calreticulin, secreted adenosine triphosphate (ATP), and passively released high mobility group protein B1 (HMGB1), are vital for the ICD of cancer cells (Krysko et al., 2012). When calreticulin is translocated to the cell surface membrane, it will act as an "eat me"-signal for phagocytosis of dying cells. This plays an essential role in activating anti-tumor immunity since radiation has the potential to initiate adaptive and innate immune responses that can result in antitumorigenic effects inside and outside of the irradiation field (Carvalho and Villar, 2018). Golden et al. found that there was a dose-dependent increase in the cell-surface calreticulin when the cells (TSA mammary carcinoma) were treated with X-ray radiotherapy (Golden et al., 2014).

Another response to ionizing radiation is the formation of micronuclei in cells. Deoxyribonucleic acid (DNA) within normal cells is typically excluded from the cytosol and contained within the nucleus and mitochondria (Samstein and Riaz, 2018). When cancer cells undergo mitosis following ionizing radiation induced unrepaired DNA double-strand breaks (DSBs), it can lead to the formation of micronuclei. Micronuclei are extra-cellular bodies that contain damaged chromosome fragment and/or whole chromosomes that were not incorporated into the nucleus after cell division (Luzhna et al., 2013). The micronuclei have defective membranes that easily break down, exposing double-stranded DNA (dsDNA) to the cytosolic DNA sensor cyclic GMP-AMP synthase (cGAS) that is a pattern recognition receptor (Rodríguez-Ruiz et al., 2018). Following activation by aberrant cytosolic DNA, the enzyme cGAS produces the mammalian 2',3'-cGAMP, which in turn activates the STING protein and thereby leads to the production of Type I interferon (IFN) and other pro-inflammatory cytokines that boost the immune response (Bose, 2017). This can potentially stimulate an immune response following ionizing radiation.

In this thesis, we aimed to investigate the measured membrane bound calreticulin, and the formation of micronuclei after X-ray radiation. However, for both experiments, it turned out that protocol development was necessary to obtain experimental data. Thus, the aim of this thesis became extended to include reliable protocols for micronuclei counting and calreticulin measurements. The calreticulin response after X-ray irradiation given in one or two fractions was measured, and the data were corrected for autofluorescence and can therefore be regarded as highly reliable. Due to time constraints, the supervisors thought the best priority was to obtain reliable experimental calreticulin data. Therefore, no experimental data for the micronuclei assay were obtained.

2 Theory

“Those who have not been trained in chemistry or medicine may not realize how difficult the problem of cancer treatment really is. It is almost – not quite, but almost – as hard as finding some agent that will dissolve away the left ear, say, and leave the right ear unharmed. So slight is the difference between the cancer cell and its normal ancestor.”

– William Woglom

2.1 Radiation Physics and Interactions in Radiotherapy

The following section is mainly based on “Radiation Physics for Medical Physicists” (Podgoršak, 2005) and “Introduction to radiological physics and radiation dosimetry” (Attix, 1986).

The study and use of ionizing radiation started with three crucial discoveries in the 19th century: X-rays by Wilhelm Röntgen in 1895, natural radioactivity by Henri Becquerel in 1896, and radium by Pierre and Marie Curie in 1898 (Podgoršak, 2005). In 1896, barely a year after Röntgen had made his discovery of X-rays, Emil Grubbe, a medical student, had the inspired idea of using X-rays to treat cancer. Grubbe had previously worked in a factory that produced vacuum X-ray tubes, and he saw with his own eyes how X-rays impacted the skin of the workers at the factory, such as swollen and peeling skin. Grubbe quickly extended the logic of this impact, cell death, to tumors (Mukherjee, 2010). It was on March 29th, 1896, that Grubbe began to treat an older woman with breast cancer with his own improvised X-ray tube. He irritated her breast every night for eighteen consecutive days, and even though the so-called treatment was painful, it was somewhat successful (the woman died later due to spreading of the cancer to her spine, brain and liver). The result was that the tumor in the breast ulcerated, tightened and shrank. This was the first documented local response in the history of X-ray therapy (Mukherjee, 2010). The potential benefit of X-rays in medicine had officially emerged, and a new branch of cancer medicine, radiation oncology, was born.

In cancer treatment today, several types of treatment methods are used. This includes surgery, chemotherapy, radiotherapy, and immunotherapy (Dobosz and Dzieciątkowski, 2019). The most frequently used type of radiation in cancer treatment today is high energy X-rays, but particle radiation therapy centers are increasing in numbers (Tian et al., 2018). This includes the use of electrons, protons, and heavier ions such as carbon ions and α-particles. However, the latter will not be discussed in this thesis, as the experiments conducted have been done using only X-rays.

2.1.1 Ionizing and Non-Ionizing Radiation

Radiation physics are often divided into two main categories: ionizing radiation and non-ionizing radiation, which can be seen in Figure 1. Radiation refers to energy in transit (Vallabhajosula, 2009). Non-ionizing radiation does not have enough energy to ionize the matter as its energy is lower than the ionization potential of atoms or molecules of the absorbing material. Examples of non-ionizing radiation are microwaves, visible light and radio waves. Unlike non-ionizing radiation, ionizing radiation can ionize matter either directly or indirectly because its quantum energy exceeds the ionization potential of the atoms and molecules of the absorbing material.

Furthermore, it is also common to divide the radiation into directly ionizing radiation and indirectly ionizing radiation, as seen in Figure 1. The energy deposition of directly ionizing radiation involves direct processes where the fast-charged particles deliver their energy to matter directly through many small Coulomb-force interactions along the particles' track. The indirectly ionizing radiation includes X- and γ-ray photons and neutrons, which first transfer their energy to the charged particles in the matter they traverse, in relatively few, but larger, interactions. The resulting electrons will then deliver the energy to the matter as described for directly ionizing radiation (Attix, 1986).

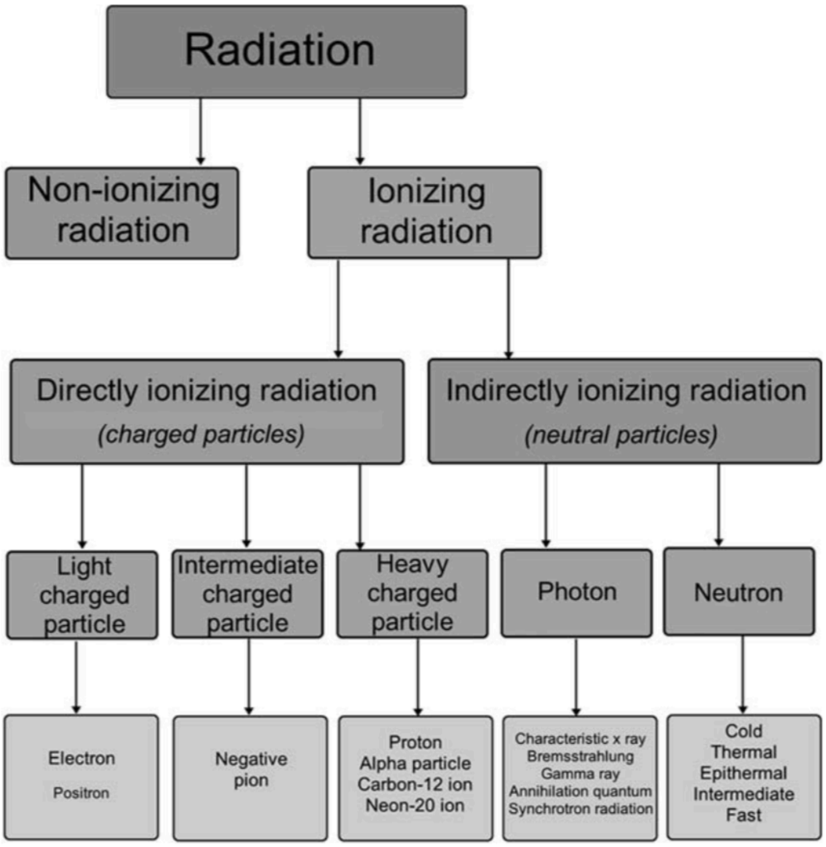

Figure 1: Radiation is divided into non-ionizing radiation, and ionizing radiation. The latter includes for example charged particles and X-rays. (Podgoršak, 2005).

As indicated above, radiation is said to be ionizing when the radiation has sufficient energy to eject one or more orbital electrons from the atom or molecule (Hall and Giaccia, 2019). The energy needed to cause a valence electron to escape an atom is of the order 4 – 25 eV. This means that for the radiation to be ionizing, it must carry kinetic energy of this magnitude or above. The important characteristic of ionizing radiation is the localized release of large amounts of energy. The energy dissipated per ionizing event is about 33 eV, which is enough energy to break a strong chemical bond, such as the double-strand in a DNA-molecule.

2.1.2 X-rays

Most experiments with biologic systems have involved X-ray or γ-rays. Both are electromagnetic radiation, and they do not differ in nature or in properties. The difference lies in how they are produced. X-rays are produced in an electrical device where electrons are accelerated to high energies and stopped in a target (usually a Tungsten-target) as described below. γ-rays are emitted by radioactive isotopes, and they are excess energy that is emitted when the excited nucleus after a decay relaxes to reach a stable form. When cells are exposed to irradiation, the cells respond to the damage induced by the radiation by dying or, more often, by ceasing to divide. Using X-rays as a treatment for cancer, the X-ray preferentially kills the most rapidly proliferating cells in the body (Mukherjee, 2010). Here, the focus will only be on X-ray production used in diagnostic and therapeutic settings.

2.1.3 Ionizing Radiation Devices: The X-ray Tube

The following section is based on “Radiation Physics for Medical Physicists” (Podgoršak, 2010) and “Introduction to Radiological Physics and Radiation Dosimetry” (Attix, 1986).

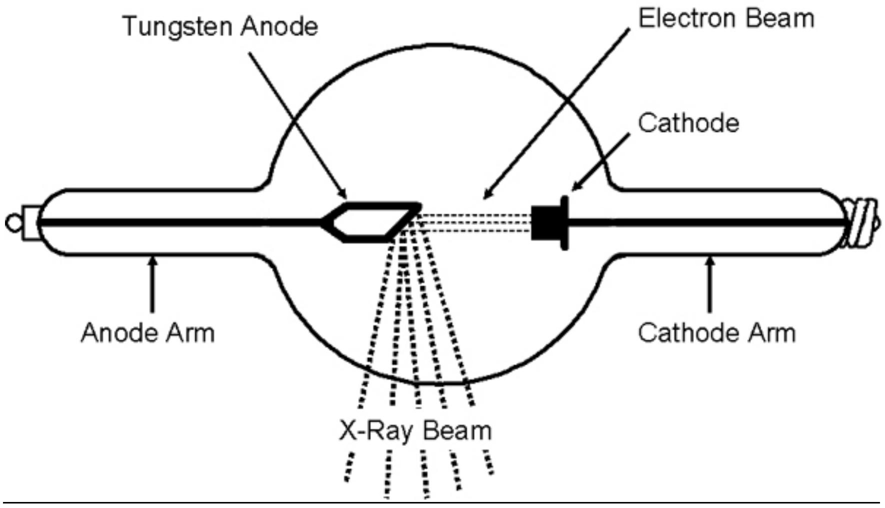

Figure 2: A Coolidge X-ray tube. Electrons are released from the cathode and hit the target (the anode) when a high potential difference is being applied over the cathode and the anode. The electrons will interact with the target creating what is known as bremsstrahlung, i.e., X-rays. Excessive heat is also being produced, setting high demands of cooling of the X-ray tube with the use of for example oil. (Universitites, 1999).

An X-ray tube, as seen in Figure 2, is a vacuum tube that converts electrical input power into X-rays. It consists of a cathode and an anode which is the target. The target has a high atomic number Z, and it is usually made of Tungsten due to the high atomic number and high melting point. A high voltage power source, called the tube voltage, is connected across the cathode and the anode, creating a high potential difference. The heated cathode emits electrons, and these electrons are accelerated towards the positively charged anode. When the electrons hit the anode, they change direction and emit bremsstrahlung, i.e., X-rays. The maximum energy of the X-rays is the same as the kinetic energy of the electrons hitting the anode, but it is only roughly 1 % of this energy that is being released as bremsstrahlung (Eirik Malinen, personal communication, 2020). In addition to bremsstrahlung, we get ionizations and excitations, and most of the electron energy will be deposited by these interactions. This requires cooling of the anode due to the excessive heat being produced, and the layer between the tube envelope and the housing therefore contains oil to ensure tube cooling and electric insulation.

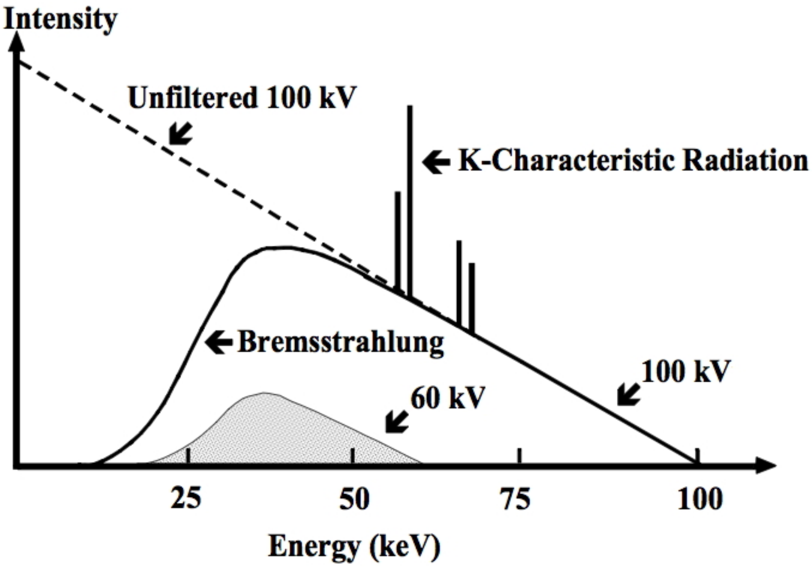

Figure 3: A typical X-ray spectrum. The dotted lines simulate the unfiltered bremsstrahlung portion of the spectrum, but by using a filter to filter out the low energy bremsstrahlung, we will get a specter represented by the solid lines. The spikes in the spectrum are called K-lines, and it shows the characteristic X-rays. (Kieranmaher, 2001).

In an X-ray tube, we will get a spectrum of X-ray energies, as seen in Figure 3. Figure 3 shows an unfiltered X-ray spectrum from a 100-kV electron beam with a continuous bremsstrahlung spectrum. The average energy of the beam is about one-third of the maximum energy. If an electron has a high enough energy, it can hit one of the orbital electrons in the inner shell and knock it out. An electron in a higher energy level will then fall down to the inner shell releasing the energy difference between the two shells as a photon. This is what is called characteristic radiation and can be seen as the four peaks in Figure 3. When using X-rays in a diagnostic or therapeutic setting, a homogenous x-ray spectrum is desired. It is therefore common to use filtering when using the X-ray machine, such as copper and/or aluminum. The filters will remove X-rays with lower energies, which only contribute to the dose in the skin of the patient, as well as the characteristic radiation. In total, we will get a lower intensity of the X-ray beam, but higher energies.

2.1.4 Interaction of Ionizing Radiation with Matter: Photons

The following chapter is based on “Introduction to Radiological Physics and Radiation Dosimetry” (Attix, 1986).

When photons of short wavelengths (X-rays or γ-rays) interact with condensed matter, they release electrons from the atoms they interact with. The processes by which their energy is transferred to the medium are stochastic events. Due to the statistical nature of the absorption process and the fact that photons are strongly scattered during their interactions with atoms, a photon beam entering condensed matter spreads rapidly and has no defined range. The photon interactions of most importance in medical physics and radiation dosimetry include photoelectric effect, Compton scattering, and pair production. These three mechanisms account for more than 99 % of the interactions between photons and matter. The probability of each event depends on the energy of the photon and the material with which it interacts (Kim, 2015). Note that these interactions are best described by quantum physics, and a specific interaction is described by probability.

The Photoelectric Effect

When a photon interacts with a tightly bound orbital electron of the absorber, e.g., the tissue, we get what is called the photoelectric effect. The incoming photon has the energy $E = h\nu$ which is absorbed by the atom, and the orbital electron is ejected with a kinetic energy E_k. E_k corresponds to the initial energy of the incoming photon minus the binding energy of the electron, E_b (see Figure 4). After the photoelectric effect has occurred, the atom is left with a vacancy. An electron from an outer shell, which has a higher energy, will fill this vacancy which also results in the emission of a photon with energy corresponding to the difference in the binding energy between the two electron shells, called characteristic radiation.

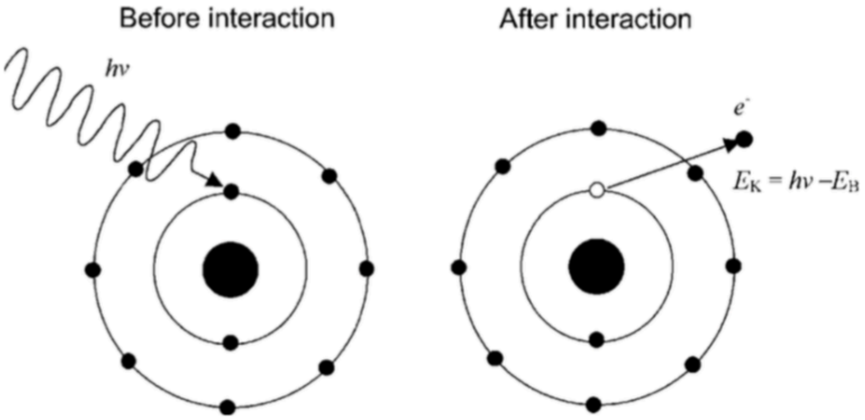

Figure 4: A schematic view of the photoelectric effect. The incoming photon with energy $E = h\nu$ is absorbed and interacts with the tightly bound orbital electron. The orbital electron will be ejected with the kinetic energy E_k,

which has the energy of the incoming photon hν minus the binding energy of the orbital electron E_b*. (Podgoršak, 2005).*

The atomic cross-section, which is the interaction probability of a particle for the photoelectric effect, is given by equation 1:

$$\tau^4 \propto \frac{Z^4}{(h\nu)^3} \qquad 1$$

Where τ is the cross-section, Z is the atomic number of the absorbing material, and $h\nu$ is the energy of the incoming photon. For a high Z material and low photon energies, there will be a high cross-section.

Compton Scattering

In the case of Compton scattering, which is also known as incoherent scattering, the incident X-ray photon will eject an electron from an atom. The incident photon will lose some of its energy to the ejected electron, and it will continue to move in a direction different from the initial direction of the photon. The resulting incident photon is called a scattered photon. We assume that the incident photon will interact with a free and stationary electron, not a bound electron, due to conservation of momentum. See Figure 5 for a schematic view of Compton scattering. In Compton scattering, the energy and momentum are conserved. The kinetic energy that is transferred to the stationary electron is the energy difference of the incident photon and the scattered photon, E' = hν – T. The scattering angle between the path of the incident photon and the scattered photon is referred to as θ, and the angle between the incident photon and the ejected electron is ϕ. When it comes to the clinical use of radiotherapy, Compton scattering is the most essential photon interaction to consider due to the fact that Compton scattering is most significant at an energy range of 100 keV to 10 MeV which is the energy range of clinical use of radiotherapy.

For Compton scattering, the atomic cross-section, σ_c^a, is given by equation 2:

$$\sigma_c^a \propto Z \qquad 2$$

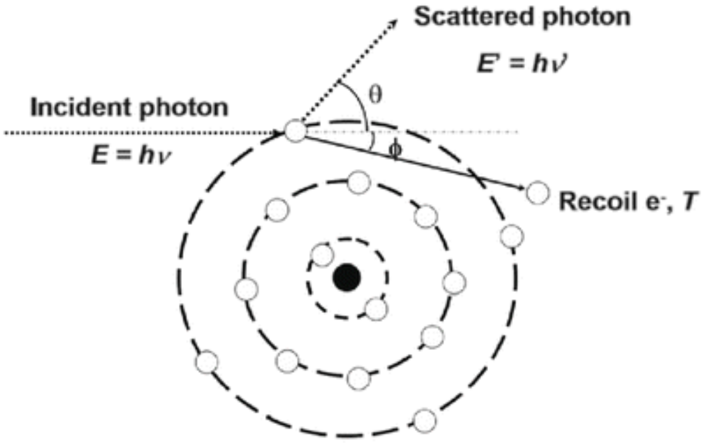

Figure 5: When Compton scattering occurs, the incident photon from the left will strike an electron, and the electron will be ejected out from the atom to which it was initially bound. Here, E is the energy of the incident photon, T is the kinetic energy of the ejected electron, and E' is the energy of the scattered photon. The incident photon energy is transferred to the ejected electron. The least amount of energy is transferred to the electron when the incident photon has no scattering, while the most amount of energy is transferred when the incident photon is backscattered. Compton scattering is most significant at an energy range of 100 keV to 10 MeV, and it is almost independent of the atomic number of the interacting material. (Kim, 2015).

Pair Production

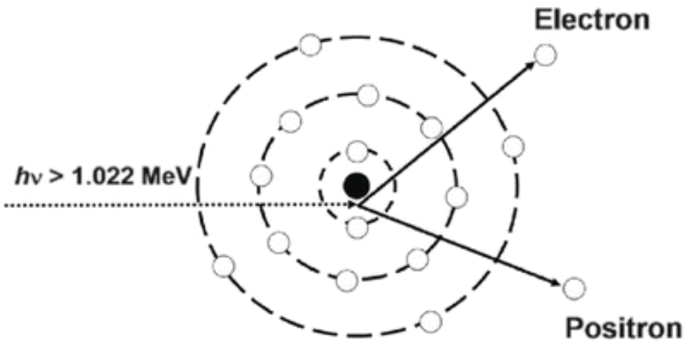

Figure 6: An overview of pair production. When an incoming photon with energy equal to or higher than 1.022 MeV comes very near the nucleus of an atom, it interacts with the nuclear Columbic field. It can then create a pair of an electron and a positron. The total kinetic energy T of the electron and position is the energy of the incident photon minus 1.022 MeV. Note that the probability of pair production is proportional to the atomic number of the target material and the incident photon energy. (Kim, 2015).

In pair production, an incoming photon with energy equal to or higher than 1.022 MeV comes very close to the nucleus of an atom, and it will interact with the nuclear Columbic field. The photon can then create a pair of an electron and a positron. Note that pair production only occurs when the incident photon has an energy of 1.022 MeV or higher, which is the minimum energy required to create an electron and a positron since the electron has a rest mass of 511 keV. The total kinetic energy T of the electron and position is the energy of the incident photon minus 1.022 MeV. This interaction is illustrated in Figure 6. The positrons are very short-lived and disappear with the creation of two 0.511-MeV photons each, which is a process called annihilation.

The total kinetic energy T transferred to the electron and positron pair is equal to the incident photon energy minus the energy of the incident photon, 1.022 MeV. Pair production is of importance when we have high energy photons passing through the matter of high atomic number Z. The atomic cross-section for pair production, $\kappa^a,$ is given in equation *3*:

$$\kappa^a \propto Z^2 \tag{3}$$

Mass energy transfer, mass absorption coefficient and absorbed dose

The mass energy-transfer coefficient describes how much energy equivalent mass is transferred to the absorbing medium. We neglect any photonuclear contribution, and the total coefficient can be found as a sum of the coefficients of the three processes of Photoelectric effect (PE), Compton scattering (CS) and pair production (PP), as shown in equation 4.

$$\frac{\mu_{tr}}{\rho} = \frac{\tau_{tr}}{\rho} + \frac{\sigma_{tr}}{\rho} + \frac{\kappa_{tr}}{\rho} \ (\mathrm{cm}^2/\mathrm{g}) \tag{4}$$

Where $\frac{\mu_{tr}}{\rho}$ is the total energy-transferred coefficient, $\frac{\tau_{tr}}{\rho}$, $\frac{\sigma_{tr}}{\rho}$ and $\frac{\kappa_{tr}}{\rho}$ are the energy-transferred coefficients for PE, CS, and PP interactions respectively. The mass energy-absorption coefficient, $\frac{\mu_{en}}{\rho}$, is related to the mass energy-transfer coefficient by equation 5.

$$\frac{\mu_{en}}{\rho} = \frac{\mu_{tr}}{\rho}(1-g) \ (\mathrm{cm}^2/\mathrm{g}) \tag{5}$$

Where g is the average fraction of secondary-electron energy that is lost in radiative interactions.

The mass energy-transfer and mass energy-absorption coefficients, and the g fractions, are tabulated for different photon energies and absorbing materials. Looking at radiation with respect to either diagnostic use or therapeutic use, we are interested in how much energy has been absorbed by the medium in question. We use the quantity absorbed dose D, describing the energy imparted to matter by all kinds of ionizing radiation, but delivered by the charged particles.

The absorbed dose D can best be defined in terms of the related stochastic quantity energy imparted ϵ. ϵ imparted by ionizing radiation to a matter of mass m in a finite volume V is defined in equation 6.

$$\epsilon = (R_{in})_u - (R_{out})_u + (R_{in})_c - (R_{out})_c + \Sigma Q \tag{6}$$

Where

$(R_{in})_u$ = the radiant energy of uncharged particles entering V,

$(R_{out})_u$ = the radiant energy of uncharged particles leaving V,

$(R_{in})_c$ = radiant energy of charged particles entering V,

$(R_{out})_c$ = radiant energy of charged particles leaving V,

ΣQ = net energy derived from rest mass in V.

The absorbed dose D, with unit Gy corresponding to [J/kg], is defined as the energy imparted at point P per unit mass inside the volume V, as seen in equation 7.

$$D = \frac{d\epsilon}{dm} \tag{7}$$

Here, ϵ is the expectation value of the energy imparted in the finite volume V during some time interval, dϵ is the expectation value of the energy imparted for an infinitesimal volume dv during some time interval at point P, and dm is the mass in dv.

2.1.5 Interactions of Ionizing Radiation with Matter: Charged Particles

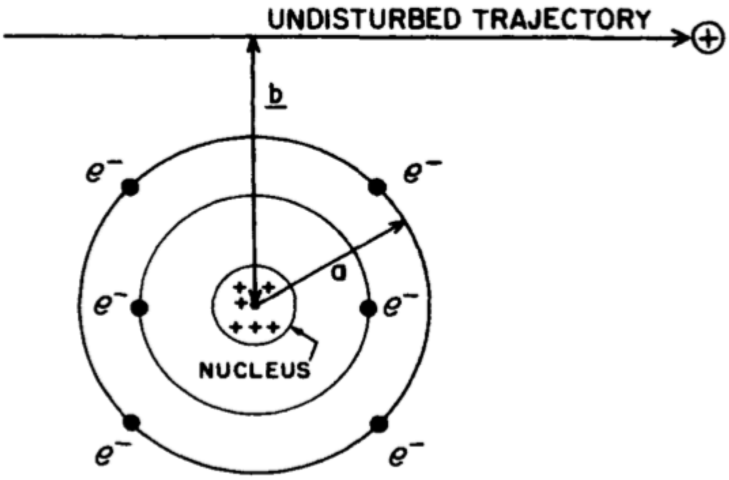

Figure 7: A schematic overview of essential parameters in charged particle collisions with atoms: a is the classical atomic radius, b is the classical impact parameter which both are further described in the text. (Attix, 1986)

A charged particle is surrounded by its Coulomb electric field, which interacts with orbital electrons and the nucleus of all atoms it encounters, as it penetrates into matter (Podgoršak, 2005). The incoming energy of the charged particle is transferred through many Coulomb interactions. Charged particle Coulomb-force interactions can be simply characterized in terms of the relative size of the classical impact parameter b vs the atomic radius a, as shown in Figure 7 (Attix, 1986). We will look at the cases when b >> a, b ~ a, and b << a, which are important for charged particle interaction with matter.

b >> a: Soft (distant) collisions

When an incoming charged particle passes an atom at a distance, the influence of the particle's Coulomb force field will affect the whole atom. Soft collision is the most probable interaction type, and soft collisions account for roughly half of the energy transferred to the absorbing medium (Attix, 1986). In a soft collision, the charged particle will distort the atom and excite it to a higher energy level, or sometimes it can cause the atom to eject a valence-shell electron (loosely bound electron), which will ionize the atom. Only a small amount of energy is transferred from the charged particle to the absorbing medium.

b ~ a: Hard (close) collisions

Hard collisions, or "knock-on" collisions, is when the impact parameter is of the order of atomic dimensions, i.e., when b is approximately equal to the radius a of the atom. Here, it is more likely that the incident charged particle will interact primarily with a single atomic electron instead of the whole atom, and the electron is then ejected from the atom with high kinetic energy and is called a delta ray. The delta ray will have enough energy to undergo additional Coulomb-force interactions on their own, and a delta ray dissipates its kinetic energy along a separate track from that of the primary charged particle (Attix, 1986). Hard collisions, compared to the number of soft collisions, are fewer, yet they still account for roughly half of the total energy transferred from the primary charged particle to the absorber.

b << a: Coulomb-Force Interactions with the External Nuclear Field

When the impact parameter is much smaller than the atomic radius a, the Coulomb-force interaction takes place mainly with the nucleus of the atom. This type of interaction is most important for electrons, and in most cases, the electrons are scattered elastically, and do not emit an X-ray photon or excite the nucleus (Attix, 1986). In 2 – 3 % of the cases when an electron passes near the nucleus, instead of losing only a small amount of energy, an inelastic radiative interaction occurs. The electron is deflected, and up to 100 % of the kinetic energy is transferred to an X-ray photon. These photons are referred to as bremsstrahlung.

b << a: Nuclear Interactions by Heavy Charged Particles (HCP)

If an heavy charged particle (HCP) has sufficiently high kinetic energy (approximately 100 MeV) and the impact parameter is less than the nuclear radius a, the HCP may interact inelastically with the nucleus of the atom. Here individual nucleons such as protons and neutron may be driven out of the nucleus in an intranuclear cascade process. The nucleus is left highly excited, and it will decay by emission of nucleons and γ-rays, which carry the kinetic energy they have gained away from the point of interaction (Attix, 1986).

The Stopping Power

During its motion through an absorbing medium, a charged particle will experience a large number of interactions. In each interaction, the charged particle's path may be altered and lead to a loss of kinetic energy. The energy will be transferred to the medium in which the charged particle interacts, called collision loss, or to photons, called radiation loss (Podgoršak, 2010). To describe the rate of energy loss/transfer by the charged particle as it traverses through the matter, we use what is known as the stopping power. The stopping power is a property of the material in which a charged particle propagates (Podgoršak, 2005). The stopping power can be seen as a material property (depending on electron density), which describes the energy absorbed by matter (Linz, 2012). The expectation value of the stopping power is given by equation 8.

$$S = \frac{dT}{dx}_{Y,T,Z} \quad (8)$$

Here, the T is the kinetic energy of the incoming charged particle, x is the unit length path, Y is the type of charged particle and Z is the atomic number of the medium of interest (Attix, 1986). The unit is typically given in units of [MeV/cm] or [J/m]. If we want the mass stopping power, we can divide the stopping power S by the density ρ of the absorbing medium. The unit for mass stopping power is typically given in [MeV/cm^2] or [J m^2/kg], and the mass stopping power is given in equation 9.

$$\frac{S}{\rho} = \frac{dT}{\rho dx} \quad (9)$$

With regard to charged particle interaction, two types of stopping power are known: radiation stopping power, S_r (also called nuclear stopping power), and collision stopping power, S_c (also called ionization or electronic stopping power) (Podgoršak, 2005). S_r is the result of charged particle Coulomb interaction with the nuclei of the absorber and mainly includes bremsstrahlung and delta rays. Note that S_r is only relevant for light particles, such as electrons and positrons, in calculations. By combining all of these stopping powers, we get the total stopping power expressed as the sum in equation 10.

$$S_{tot} = S_{rad} + S_{col}^{soft} + S_{col}^{hard} \quad (10)$$

The Bethe-Bloch formula gives the mean rate of energy loss (stopping power) of a heavy charged particle, and it is given in equation *11.*

$$-\frac{dT}{dx} = \frac{4\pi e^2 (ze)^2}{mv^2} nZ(\ln \frac{2mv^2}{I} - \ln(1 - \beta^2) - \beta^2) \quad (11)$$

Where v is the velocity of the incoming particle, ze is the charge of the incoming particle, m is the mass of the electron, n is the number of atoms per cm^3, Z is the effective atomic number, I is the mean ionization potential, and β is the velocity of the particle relative to the speed of light. The Bethe-Bloch formula can be used to see how the rate of energy loss depends on the material it interacts with, i.e., the rate of energy loss by the charged particle increases when the material it interacts with has a high density of electrons (NZ). The rate of energy loss is also dependent on the speed of the incoming particle. In addition, as the particle loses energy (hence the speed decreases), the rate of energy loss also increases.

2.1.6 Linear Energy Transfer (LET)

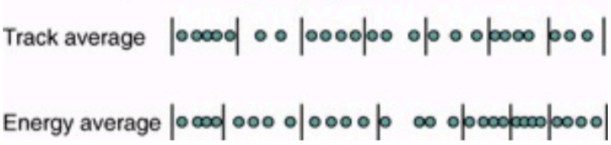

Figure 8: Linear energy transfer (LET) is the average energy deposited per unit length of the track. To calculate the track average, the track is divided into equal lengths and the average of the energy deposited in each length is found. The energy average is calculated by dividing the track into equal energy intervals and averaging the lengths of the track that contain this amount of energy. (Hall and Giaccia, 2019).

Stopping power focuses on the energy loss by an energetic charged particle which traverses through an absorber. Instead, it is possible to look at the ionization density produced by ionizing radiation in the medium it traverses. It depends on what is called the linear energy transfer (LET) of the ionizing radiation beam. LET is used in radiobiology and radiation protection to specify the quality of an ionizing radiation beam (Podgoršak, 2010). For a spectrum of particles, there are different methods for calculating spectrum average LET values. This thesis will not discuss these methods, but in general, the LET is usually calculated as a track average or energy average, as seen in Figure 8.

LET is generally expressed in units of [keV/μm] with 10 keV/μm separating the low LET (sparsely ionizing) radiation from the high LET (densely ionizing) radiation (Podgoršak, 2005). LET has long been viewed as a significant parameter to discern qualitatively the biological effect of different kinds of radiation, but it can be problematic since LET is not a constant value and the limitations of LET become particularly prominent when ions of different atomic number are compared (Linz, 2012). As the charge and energy of a projectile ion change along the particle’s path, the LET value also changes. Even though LET is not a suitable parameter to describe the full spectrum of biological radiation effects, it is still a widely used quantity to categorize ion-induced damage. Typical LET values for X-rays and protons are listed in Table 1.

Table 1: The table shows typical LET values for various radiations. Notice that the LET value decrease when the radiation energy increase. (Hall and Giaccia, 2019).

Radiation	LET value [keV/ μm]
250-kV X-rays	2.0
10-MeV protons	4.7
150-MeV protons	0.5

2.2 Cell Biology

"Almost all aspects of life are engineered at the molecular level, and without understanding molecules we can only have a very sketchy understanding of life itself."

– *Francis Harry Compton Crick*

The following section is based on "Molecular Biology of the Cell" (Alberts, 2015).

All of the cells in the human body are derived from the fertilized egg, which is one single cell. The cell forms the basic unit of life in all forms of living organisms. The fertilized egg undergoes trillions of cell divisions in order to become an individual human being. The cells reproduce by duplication of their contents and then dividing into two equal halves. The reproduction of a somatic cell involves two sequential phases: the mitosis which is the process of nuclear division, and the cytokinesis which is the actual cell division. The life cycle of the cell is the period from one cell division to the next, but the duration of the cell cycle varies significantly from one cell type to another.

Cells are divided into two major classes: prokaryotes and eukaryotes, the former including bacteria, blue-green algae and rickettsia, and the latter including yeasts and plant and, animal cells. The eukaryotes are far more complex and complicated than the prokaryotes. In eukaryotes the cells are organized into organelles, each outlined by a membrane. The deoxyribonucleic acid (DNA) is the hereditary material in humans and almost all other organisms. Most of the DNA is in the cell nucleus, called nuclear DNA, but a small amount of DNA can also be found in the mitochondria, the mitochondrial DNA. See Figure 9 for a schematic drawing of a eukaryotic cell, and Table 2 for an overview of the different cell structures and their functions.

2.2.1 The Cell Structure and Function

See Figure 9 for a schematic drawing of a eukaryotic cell, and in Table 2, the major cell structure and functions are listed.

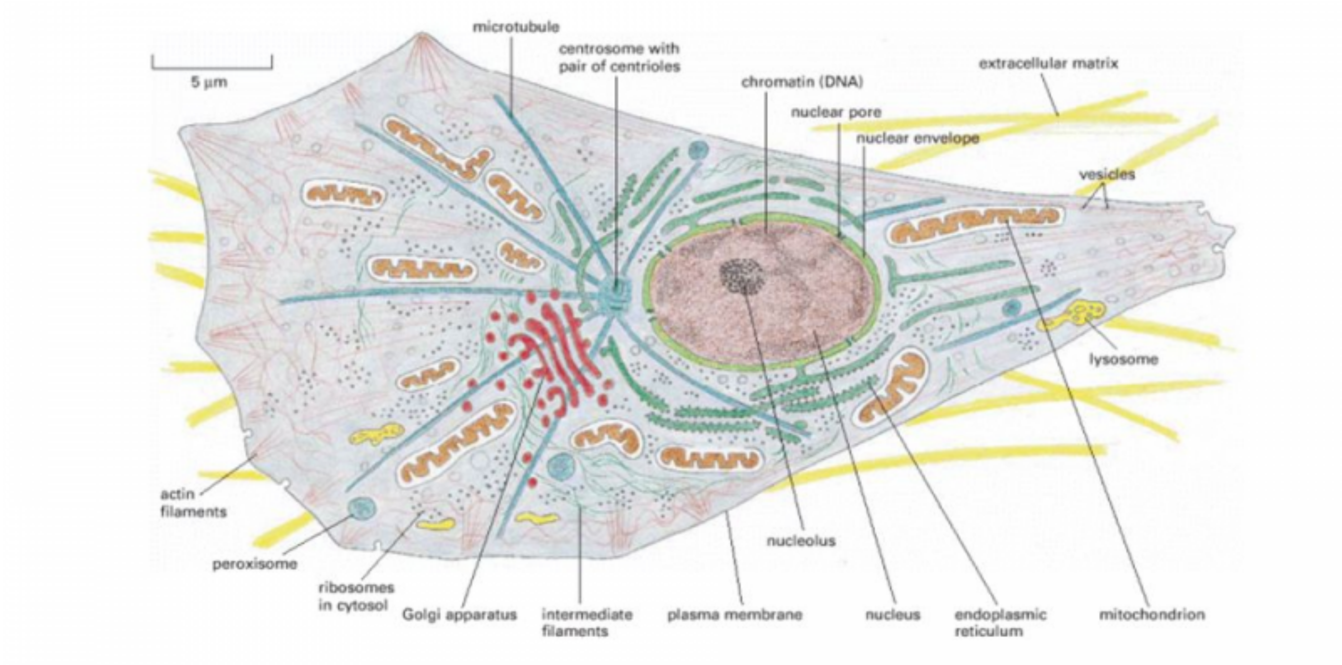

Figure 9: A schematic drawing of an animal cell and its main components. A more detailed description of the most relevant cell structures and their functions can be seen in Table 2. (Alberts, 2015).

Table 2: A list of the most relevant cell structures and their functions.

Cell structure	Major functions
Plasma membrane	Cell morphology and movement, transport of ions and molecules, cell-to-cell recognition, cell surface receptors
Endoplasmic reticulum (ER)	Formation of compartments and vesicles, membrane synthesis, synthesis of proteins and lipids
Lysosomes	Digestion of worn-out mitochondria and cell debris, hydrolysis of proteins, carbohydrates, lipids, and nucleic acids
Golgi complex	Modification and sorting of proteins for incorporation into organelles and for export, forms secretory vesicles

Microbodies	Isolation of particular chemical activates from the rest of the cell body
Mitochondria	Cellular respiration, oxidation of carbohydrates, proteins and lipids
Nucleus	DNA synthesis and repair, RNA synthesis, control center of the cell, directs protein synthesis and reproduction
Chromosomes	Contain hereditary information in the form of genes
Ribosomes	Sites of protein synthesis in cytoplasm
Cytoskeleton	Structural support, cell movement, cell morphology

2.2.2 The Cell Membrane

The plasma membrane, which encloses the cell, defines its boundaries and separates the cell from the outside environment, also known as the extracellular environment. It maintains the essential difference between the cytosol and the extracellular environment. Inside the eukaryotic cells, the membranes of the nucleus, endoplasmatic reticulum (ER), Golgi apparatus and other membrane-enclosed organelles help to maintain the characteristic differences between the contents of each organelle and the cytosol. In all cells, the plasma membrane contains proteins called receptors, and they act as sensors of external signals. This allows the cells to change their behavior in response to environmental signals. This includes signals from other cells. Receptors transfer information – not molecules – across the membrane.

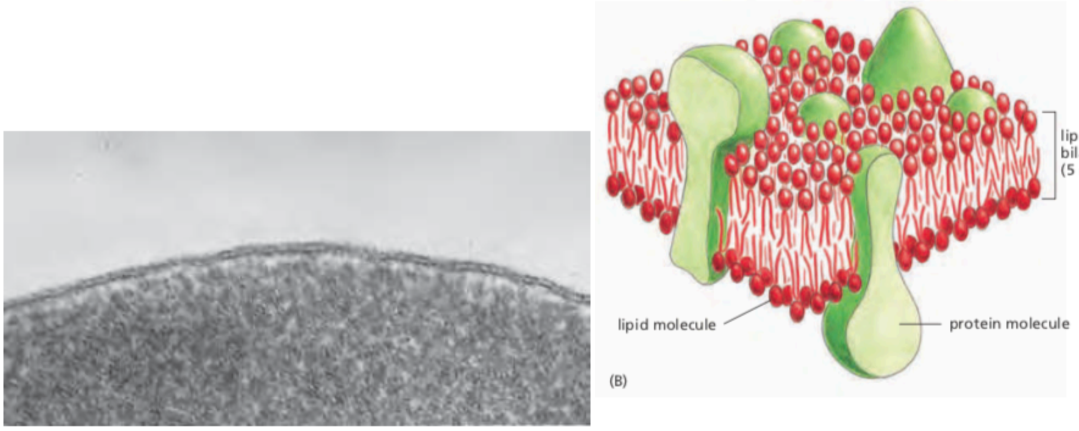

Figure 10: Two views of a cell membrane. Left panel shows an electron micrograph of a segment of the plasma membrane of a human red blood cell in cross-section. The micrograph shows the bilayer structure of the cell membrane. Right panel shows a schematic drawing of a cell membrane and the general disposition of its lipid and protein constituents. (Alberts, 2015).

All biological membranes have a common general structure, although they differ in functions. See Figure 10 showing both an electron micrograph of a human red blood cell, and a three-dimensional drawing of a cell membrane and its components. As seen in the right panel in Figure 10, each cell membrane is a very thin film of lipid and protein molecules, which are held together by mainly noncovalent interactions. The cell membrane is composed of a double layer of fat called the lipid bilayer in which membrane proteins are embedded. It provides the basic fluid structure of the membrane and serves as a relatively impermeable barrier to the passage of most water-soluble molecules. It is called a “lipid layer” because it is composed of two layers of lipids molecules organized in two sheets. The lipid molecules are arranged as a continuous double-layer about 5 nm thick.

There are two important regions of a lipid that provides the structure of the lipid bilayer. Each lipid contains a hydrophilic region and a hydrophobic region. The hydrophilic region is attracted to aqueous water conditions while the hydrophobic region is repelled by aqueous water conditions. The most abundant class of lipid molecule found in the plasma membrane is the phospholipid. It contains a phosphate group, and sports two nonpolar fatty acid chain groups as its tail. This tail is composed of a string of carbons and hydrogens, as seen in Figure 11.

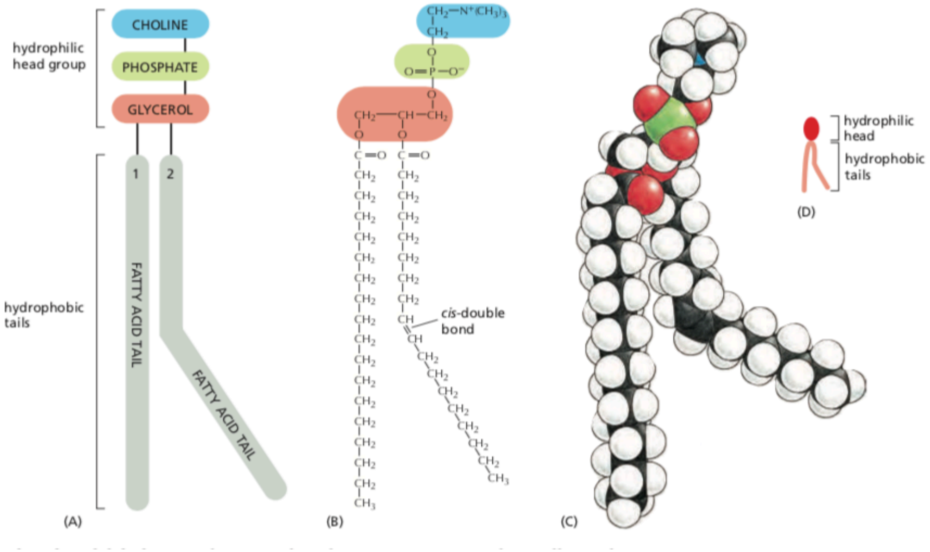

Figure 11: An overview of a typical phospholipid molecule. This example is a phosphatidylcholine, and in (A) we see it represented schematically, in (B) by a formula and in (C) as a space-filling model and in (D) as a symbol. (Alberts, 2015).

In the bilayer, the phospholipids organize themselves so that they hide their hydrophobic tail regions, and they expose the hydrophilic regions to water. This structure forms the layer that is the wall between the inside and the outside of the cell. The most important property of the bilayer, as stated above, is that it is a highly impermeable structure which means molecules cannot freely pass across the bilayer. For large molecules and small polar molecules to be able to pass through the bilayer, they will need the assistance of other structures.

In addition to the lipid bilayer, the plasma membrane also contains a number of membrane proteins. While the lipid bilayer provides the structure for the plasma membrane, membrane proteins perform most of the membrane's specific tasks and therefore serving as a specific receptor, enzymes, transporters and so on.

2.2.3 The Cell Cycle

Before a cell can divide, it must complete several tasks. The cell must grow and copy its genetic material, and physically split into two daughter cells. The cell cycle of eukaryotic cells is divided into several phases of growth and maturation, but the two major phases are the mitotic phase (M phase) and the interphase. See Figure 12 for the four phases of the cell cycle.

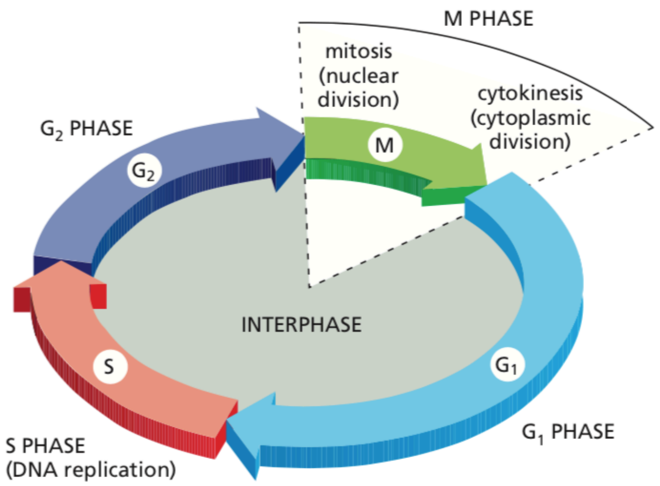

Figure 12: The cell cycle is a four-stage process. It consists of the Gap 1 (G1) phase, Synthesis, Gap 2 (G2), and mitosis. An active eukaryotic cell will undergo these cell cycle steps as it grows and eventually divides. (Alberts, 2015).

The interphase: G_1, S- and G_2-phase

The interphase can be divided into three phases: G_1, S and G_2. It is during the G_1-phase, also known as the first gap phase, that the cell physically grows larger. It also copies organelles and makes the molecular building blocks the cell will need in later steps. To produce two similar daughter cells, the complete DNA instructions in the cell must be duplicated. This duplication of the DNA happens during the S-phase, also known as the synthesis phase. In the second gap phase, the G_2-phase, the cell grows even more, make protein and organelles, and it begins to reorganize its content in preparation for mitosis. The G_2-phase ends when mitosis begins.

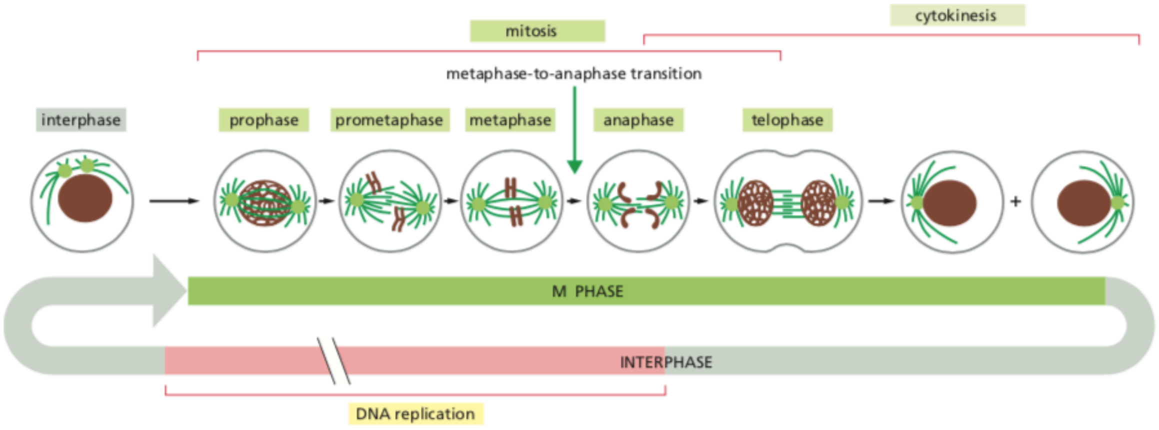

Figure 13: A detailed overview of the events of eukaryotic cell division as seen under a microscope. The mitotic phase (the M phase) is divided into the mitosis (the nuclear division) and cytokinesis (cell division). It is further divided into prophase, prometaphase, metaphase, anaphase, telophase, and cytokinesis. The M phase typically

occupies a small fraction of the cell cycle. The interphase occupies a longer fraction of the cell phase, and it includes the S phase and the gap phase (discussed in the text). (Alberts, 2015).

The mitotic phase: M-phase

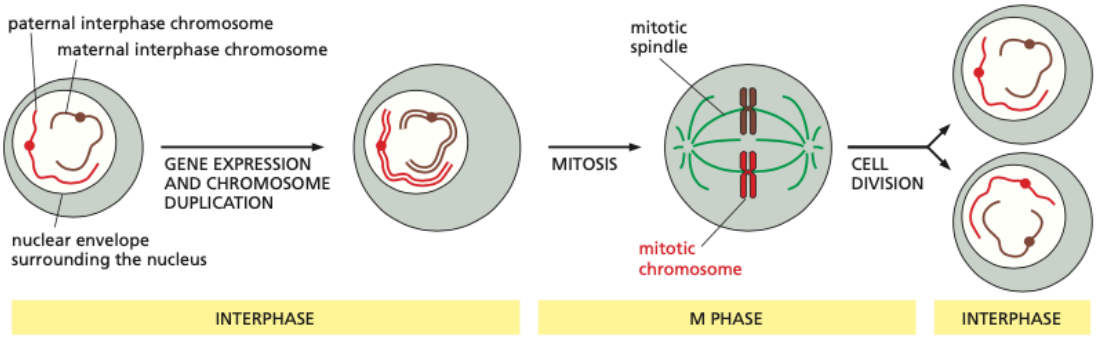

Figure 14: A very simplified view of the eukaryotic cell cycle. During the interphase, the DNA is replicated, and each chromosome is duplicated to produce two closely paired sister DNA molecules. A cell with only one type of chromosome is illustrated here. Once the replication of the DNA is complete, the cell can enter the M phase where the nucleus is divided into two daughter nuclei. During this stage of the cell cycle, the chromosomes condense, the nuclear envelope breaks down, and the mitotic spindle forms from microtubules and other proteins. The condensed mitotic chromosomes are captured by the mitotic spindle and pulled to each end of the cell by separating the members of each sister-chromatid pair. A nuclear envelope re-forms around each chromosome set, and it is in the final step of the M phase that the cell actually divides and produce two identical daughter cells. (Alberts, 2015).

During the mitotic phase (M phase), as seen in Figure 14, the cell divides its copied DNA and cytoplasm to make two new functional daughter cells. The M-phase involves two distinct division-related processes: mitosis and cytokinesis (see Figure 13). In mitosis, the nuclear DNA of the cell condenses into visible chromosomes and is pulled apart by the mitotic spindle. The M-phase is again divided into four phases: the prophase, metaphase, anaphase and telophase.

During the prophase, which is the first stage in mitosis, the chromosomes condense and become visible. Spindle fibers emerge from the centrosomes, and the nuclear envelope breaks down. In the metaphase, which is the second stage of mitosis, the chromosomes continue to condense and become distinguishable as they align in the center of the dividing cell. During the anaphase, the mitotic spindle is fully developed, and the centrosomes are at opposite poles of the cell. The sister chromatids are pulled apart and drawn to opposite poles, thus completing the accurate division of the replicated genome. Anaphase is the fourth step in mitosis, and in anaphase, cohesion proteins binding the sister chromatid together break down. Sister chromatid (now called chromosomes) are pulled toward opposite poles, and nonkinetochore spindle fibers lengthen, lengthening the cell. In telophase, the chromosomes arrive at opposite poles and begin to decondense. Nuclear envelope material surrounds each set of chromosomes, and the mitotic spindle breaks down. The physical division of the cytoplasm and the cell into two daughter cells are called the cytokinesis, which is the sixth and final step of mitosis. The duration of S, G_2, and M phase is relatively constant from cells of a given species. G_1 and G_0 phase can vary widely.

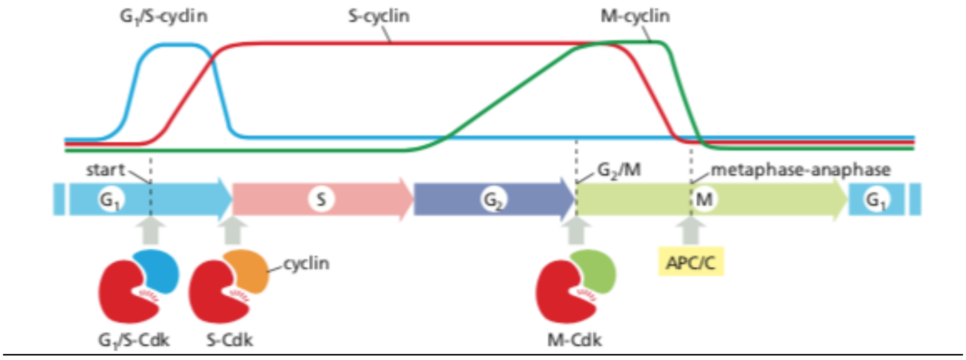

Figure 15: Cyclin-Cdk complexes of the cell-cycle control system. The concentration of the three major cyclin types will rise and fall during the cell cycle, indicated with light blue, red and green lines respectively, while the concentration of Cdks (not shown) do not change and exceed cyclin amounts. (Alberts, 2015).

2.2.4 The Cell-Cycle Control System

Cell-cycle checkpoints are control mechanisms in eukaryotic cells, which supervise the cell cycle and ensure that we have a proper cell division, represented by Figure 16. The cell-cycle control system can also trigger certain events in the cell division. These include the G_1 checkpoint, G_2 checkpoint, and an M checkpoint, as well as the ability to switch to the G_0 phase, which is an inactive phase-out of the cell cycle. In fact, if a cell has received a signal to grow and divide, but the extracellular conditions are unfavorable, the cell will enter the G_0 resting phase. Here, the cell can remain for extended periods of time if for example the cell has differentiated or if there is no need for the cell to divide. The G_0 resting phase is one of the most powerful mechanisms in preventing uncontrolled cell proliferation.

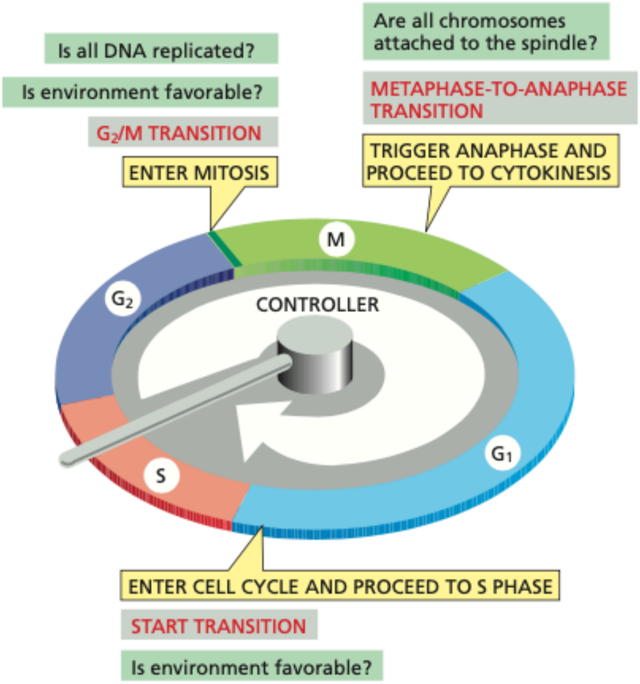

Figure 16: A schematic overview of a cell-cycle control system which triggers the essential processes of the cell cycle. In this figure, the control system is represented as a central arm that rotates clockwise. This triggers essential processes when it reaches specific transitions on the outer dial (yellow boxes). Information about the completion of different cell-cycle events and signals from the environment can cause the control system to arrest the cycle at these transitions to prevent a damaged cell from replicating. The green boxes represent different criteria that need to be fulfilled for the cell cycle to continue. (Alberts, 2015).

The cell-cycle control system depends on cyclically activated cyclin-dependent protein kinases (Cdks). These proteins are activated at different points in the cell cycle. See Figure 15 for an overview of the different Cyclin-Cdk complexes of the cell-cycle control system. The Cdks are split into four groups depending on what part of the cell cycle they control. The cyclins bind to Cdks and form a Cyclin-Cdk complex. This Cyclin-Cdk complex trigger cell cycle events depending on which cyclin the Cdks bind to.

In late G_1, rising G_1/S-cyclin levels lead to the formation of G_1/S-Cdk complexes that trigger progressing through the Start transition. S-Cdk complexes form at the start of S phase. This triggers the DNA replication, as well as some early mitotic events. M-Cdk complexes form during G_2 but are held in an inactive state. They are activated at the end of the G_2/M transition. All cyclin levels fall after they have activated their respective processes.

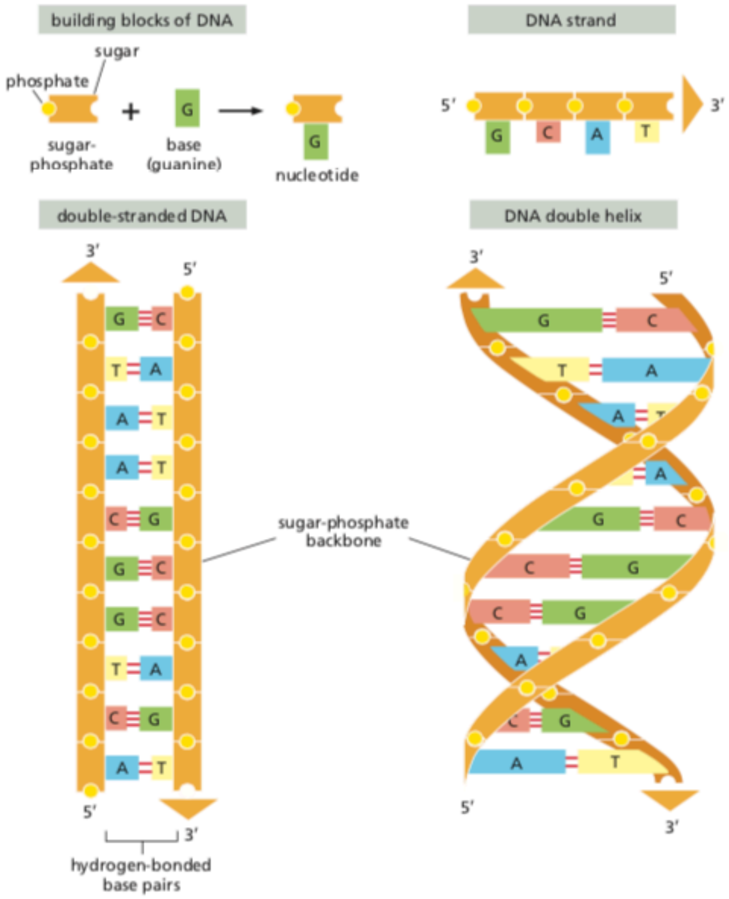

Figure 17: The DNA and its building blocks. The DNA is made up of four nucleotides which are covalently linked into a polynucleotide chain (the DNA strand) with a sugar-phosphate backbone from which the bases (A, C, G and T) extend. A DNA molecule is composed of two antiparallel DNA strands that are being held together by hydrogen bonds between the paired bases. To the left is a straightened DNA, but the DNA strand is, in reality, a double helix which is twisted as seen to the right. (Alberts, 2015).

2.2.5 Cell Death

As crucial as cell division is for the development and maintenance of an organism, cell death is just as an essential mechanism of the cell to maintain a healthy organism. Cell death is the event of a biological cell ceasing to carry out its functions, not necessarily actual death in the sense of disappearing. We have several different cell deaths, and it may be the result of natural processes to e.g., maintain the tissue size of the organism (such as for grown-up individuals, where cells are continually being replaced), where the old cells die and are replaced by new ones. It could also be the result of other causes such as infections and diseases. Apoptosis and autophagy are both what is called programmed cell death. Another vital cell death is the immunogenic cell death eliciting an immune response. This will be discussed in section 2.4.

Cells that die during programmed cell death usually undergo apoptosis. This involves a series of morphological changes such as shrinking and condensing of the cell, collapse of the cytoskeleton and disassembling of the nuclear envelope. The nuclear chromatin also condenses and breaks up into fragments. Also, if the cell is large, it can break up into membrane-enclosed fragments called apoptotic bodies. The surface of the cell or of the apoptotic bodies becomes chemically altered and, in this way, the surrounding cells or macrophages can engulf the membrane-enclosed fragments avoiding any spill-out of the content of the dead cell. Apoptosis is a neat way of cell death which causes no inflammatory response.

Another cell death is necrosis which is a non-physiological process that occurs as a result of infection or injury. Necrosis can occur when a cell has been damaged, e.g., through external force such as trauma or infections. During necrosis, a cell undergoes swelling, followed by uncontrolled rupture of the cell membrane with cell contents being expelled. Unlike apoptosis, these cell contents often then go on to cause inflammation in nearby tissue. The two cell death processes, apoptosis and necrosis, can be seen in Figure 18.

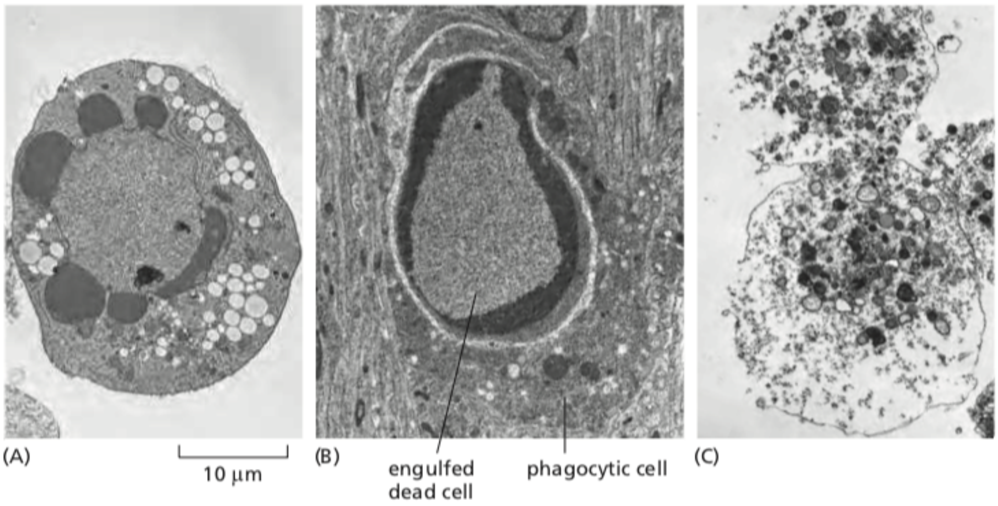

Figure 18: The figure shows the two forms of cell death seen in (A) as apoptosis and in (C) necrosis. In (A) the cell died in a culture dish, and in (B), the cell has been engulfed by a phagocyte in developing tissue. In (C), the cell died in a culture dish. (Alberts, 2015).

2.3 Radiobiology

The following section is based on “Radiology for the Radiologist” (Hall and Giaccia, 2019) and “Nuclear Medicine Physics: A Handbook for Teachers and Students” (Bailey et al., 2014).

2.3.1 Direct and Indirect Action of Radiation

Radiobiology is the study of the impact of ionizing radiations on living things (Hall and Giaccia, 2019). In this section, the focus is on how ionizing radiation impact cancer cells.

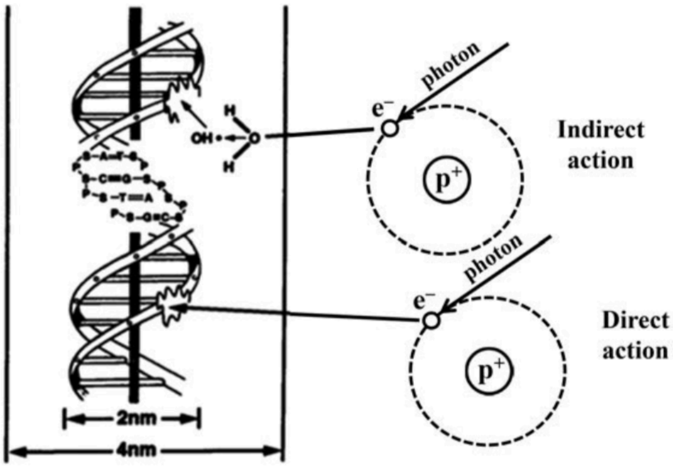

Figure 19: A schematic overview over the difference between direct and indirect damage to the cellular DNA (seen left). A direct action is when a primary charged particle or secondary electron acts directly on the DNA-molecule in the cell nucleus and causes damage. Indirect action is when non-charged particles, e.g., photons, interact with e.g. cellular water. The energy absorbed by the water molecule results in the formation of ion pairs and reactive oxygen metabolites such as hydroxyl radicals. These free radicals can interact with cellular atoms and molecules and it is these free radicals that cause the damage. (Bailey et al., 2014).

When ionizing radiation is absorbed in biological material, the effect of the radiation can be classified as either direct or indirect actions, as seen in Figure 19 . When the ionizing radiation interacts directly with the atoms of the target molecule (the DNA) and causes ionizations and excitations, the process is characterized as direct. This can then initiate the chain of events that eventually lead to a biologic change. Direct action of radiation is dominant when we have radiation with a high LET value, such as neutrons and α-particles.

An indirect action is a two-step process. Here the incoming radiation will first interact with other atoms or molecules such as water, which constitutes approximately 80 % of the cell. This will result in free radicals. A free radical is an atom that has an unpaired orbital electron in the outer shell, and they are highly reactive and able to transfer chemical damage to the molecules they interact with. The free radicals can diffuse a distance from where the interaction with the incoming ionizing radiation took place, and it is the free radicals that cause the damage in the DNA. Indirect action is predominant for radiation with low LET values, such as X-rays.

In Table 3 we see the two main processes of how water radicals are formed. One process involves the ionization of a water molecule by ionizing radiation. When the IR interacts with the water molecule, an electron is released from the water molecule as seen in step 1. The resulting molecule and ejected electron can then undergo further processes as seen in step 2, which lead to the formation of the two water radicals H^* and OH^*. Process two occurs when the ionizing radiation excites the water molecule. The water molecule will then release its excess energy to reach a stable state by separating the two water radicals.

Table 3: The table lists the chemical reaction of when water molecules are produced through the interaction between biological material and incoming ionizing radiation. It is a two-step process and for simplicity we assume that the interaction is with H_2O since our cells are composed of 80 % water. The table is adapted from Emma Thingstads master thesis. (Thingstad, 2019).

	Step 1	**Step 2**
Ionization	$H_2O + IR \rightarrow H_2O^+ + e^-$	$H_2O^+ \rightarrow H^+ + OH^-$ $e^- + H_2O \rightarrow OH^- + H^*$
Excitation	$H_2O + IR \rightarrow H_2O^*$	$H_2O^* \rightarrow H^* + OH^*$

2.3.2 Relative Biological Effectiveness (RBE)

The amount or quantity of radiation is expressed in terms of absorbed dose with unit Gray [Gy] as discussed above. The absorbed dose is a measure of the energy absorbed per unit mass of tissue, e.g., 1 J/kg equals 1 Gy. However, equal doses of different types of radiation may not produce equal biological effects. Therefore, using dose to describe the biological effect is often not adequate. When we are to compare different radiations and their impact on tissue, it is customary to use X-rays as the standard reference. For example, 1 Gy of neutrons will produce a greater biologic effect when compared to the effect of 1 Gy of X-rays. The National Bureau of Standards defined in 1954 what is known as the relative biologic effectiveness (RBE), which is a more adequate way of describing the biologic effect of radiation, and it is defined as follows:

> *"The RBE of some test radiation (r) compared with X-rays is defined by the Ratio D_{250}/D_R, where D_{250} and D_r are, respectively, the doses of X-rays and the test radiation required for equal biological effect."*

The reference radiation is normally a low-LET quality radiation, such as 250-kV X-rays. Figure 20 shows the RBE of ion beams as a function of LET for different cells. The RBE rises to a maximum at an LET of about 100 keV/µm and then falls for higher values of LET.

At 100 keV/µm we have the optimum LET value in terms of biological damage due to the density of ionizations at this energy. The average distance between ionizations at 100 keV/µm is approximately 2 nm. The diameter of the double-helix is also 2 nm, which means that for sparsely ionizing radiation such as X-rays, the probability of causing a DSB is low. It is therefore usually required to have more tracks to achieve DSBs for sparsely ionizing radiation. For more densely ionizing radiation (>100 keV/µm), the number of ionizations is higher than the diameter of the double-helix. To create a DSB in the double-helix, only one ionization per 2 nm is required, and for densely ionizing radiation we will have more ionizations per 2 nm which is a waste of energy and we get what has been interpreted as "overkill" effect, i.e., more dose is deposited in a cell than is necessary to kill it (Linz, 2012).

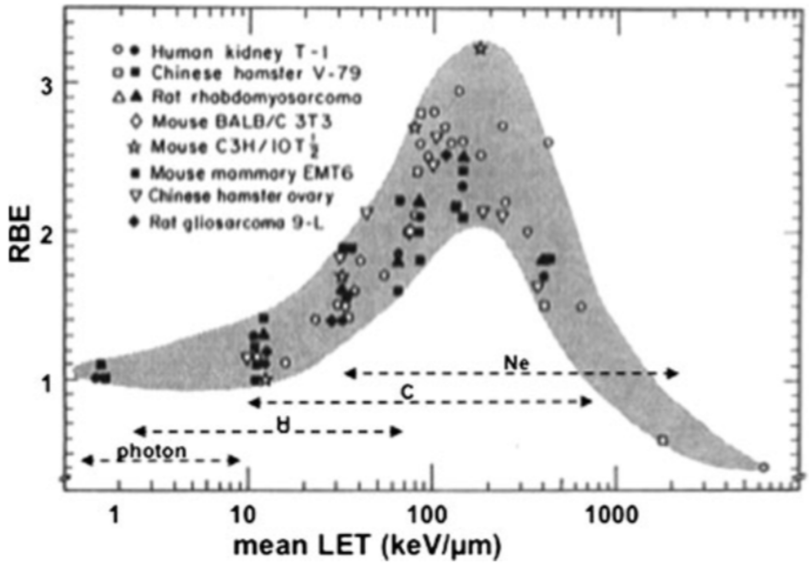

Figure 20: Relative biological effectiveness (RBE) of ions beams as a function of linear energy transfer (LET). The compilation for a number of cell types shows that there is a trend but no simple relationship between the two. The dashed arrows indicate the approximate LET range for photons and various ions, such as Carbon ions. (Linz, 2012).

2.3.3 DNA Damage and Repair

Radiation damage produces a wide range of lesions in the DNA, such as single strand breaks (SSBs), double strand breaks (DSBs), and base damage to name a few. There are several repair mechanisms for DNA damage, further discussed below. The percentage of lesions causing cell death is very small, and by a dose of 1 – 2 Gy, the numbers of lesions induced in the DNA of a cell are approximately:

- Base damage: more than 1000
- SSBs: approximately 1000
- DSBs: approximately 40

When it comes to cell death, DSBs play a central role. DSBs are also important when it comes to carcinogenesis and hereditary effects. They are the most complicated damage to repair, however, not impossible. During the S phase or the G_2 phase, the damage can be repaired by using the sister chromatid as a template. This is called homologous repair (HRR) and can be seen in Figure 21. HRR requires that the sister chromatid is undamaged in the same area where the repair is needed. If the damage occurs in G_1 phase, where a chromatid that can be used as a template is non-existent, non-homologous end joining (NHEJ) is the repair mechanism.

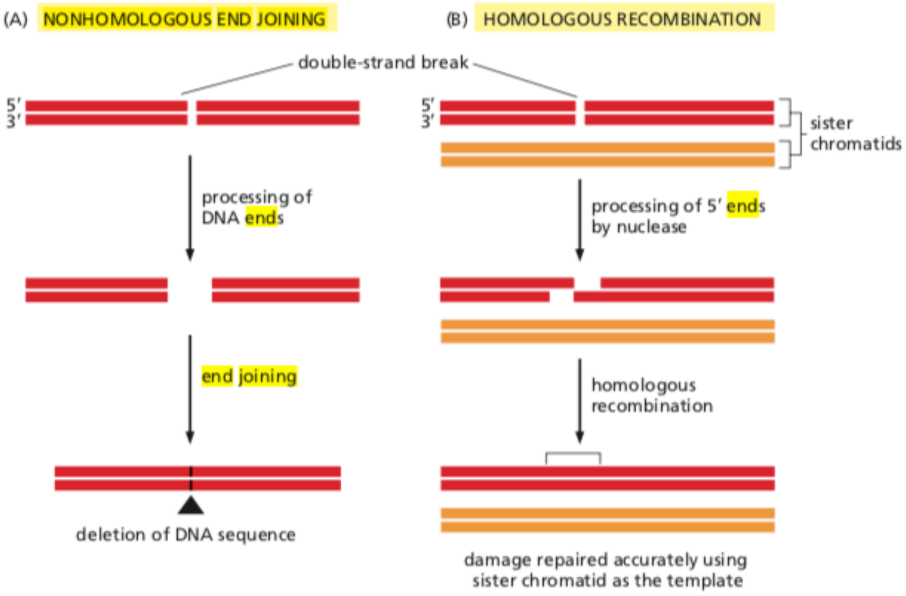

Figure 21: An overview of two ways to repair double strand breaks in the DNA strand of the cell. To the left, (A), is the mechanisms of nonhomologous end joining (NHEJ). The first step is the degradation of the broken nucleotides that cannot be ligated. After this, the ends are ligated together. NHEJ usually takes place when cells have not yet duplicated their DNA. To the right, (B), we see homologous recombination repair (HRR). Repairing the DNA double-strand breaks by HRR is more difficult to accomplish due to the need of an undamaged DNA strand to serve as a template. The 3' end of the damaged DNA strand invades the intact strand in search of homologous sequences through base pairing. DNA polymerase synthesizes DNA on the broken strand and then the repaired strand can be used as a template for the remaining broken strand. (Alberts, 2015).

NHEJ repairs DNA DSBs through the orchestration of end-to-end joining without attempt to replace missing base pairs. HRR is an error-free process because repair is performed by copying information from the undamaged homologous chromatid/chromosome, while NHEJ is error-prone because it does not rely on sequence homology. Misrepaired or unrepaired damage of the DNA could lead to mutations and chromosome damage in the exposed cell, which in the end might lead to the development of cancer or hereditary effects. However, severe chromosome damage often leads to cell death.

2.3.4 Fractionations

This section is based on "Application of Current Radiation Delivery Systems and Radiobiology" (Loeffler et al., 2012).

Using radiotherapy in the treatment of cancer patients can be done in different ways. One way is to give the dose as one fraction, i.e., giving all the irradiation in one treatment. However, often is conventional radiotherapy fractionated into daily doses. This is thought to result in reduced effect of radiation on the normal tissue. Fractionation allows for DNA repair to occur, and normal tissue has a better ability to repair DNA damage than tumor tissue. Fractionation also allows for the reoxygenation of hypoxic areas. This will result in increased sensitivity of malignant cells that previously were hypoxic. Also, another important aspect of using fractionation when giving radiotherapy is that it allows for reassortment of cells in the cell cycle. Cells are most sensitive to radiation during the G_2/M phase of the cell cycle and most resistant to radiation during the lase S phase and G_1 phase. Giving radiation in daily fractions will then allow those cells that are in resistant phases of the cell cycle move to more sensitive phases of the cell cycle. The downside of using fractionation is that it also allows for repopulation of tumor cells during the treatment.

2.4 Immunology

This section is based on the book "The Immune System" (Parham and Janeway, 2015).

Our immune system protects us from infection through various lines of defense. Immunology is the study of the immune system. If the immune system is not working as it should, it could result in infections, diseases such as cancer and allergy or even autoimmunity, the latter being a misdirected immune response that occurs when the immune system goes awry and attacks the body itself.

Immunology has changed the face of modern medicine, from Edward Jenner's work in the 18th century which eventually leads to vaccination in its modern form, to scientific breakthroughs in the 19th and 20th century which have made us able to perform organ transplants or even the global use of monoclonal antibodies. The immune system can act as both a suppressor and promotor of cancer, known as cancer immunoediting, which poses a challenge from a therapeutic perspective. The immune system is also able to selectively recognize and kill cancer cells, a process which is called immunosurveillance. As a counter strategy, cancer cells have evolved to bypass this process and instead they are able to use the immune system to promote tumorigenesis (Bose, 2017). Of interest with regards to this thesis is the abscopal effects seen after ionizing radiation, and the immunogenic cell death, both further discussed below.

2.4.1 Abscopal Effects and Immunogenic Cell Death

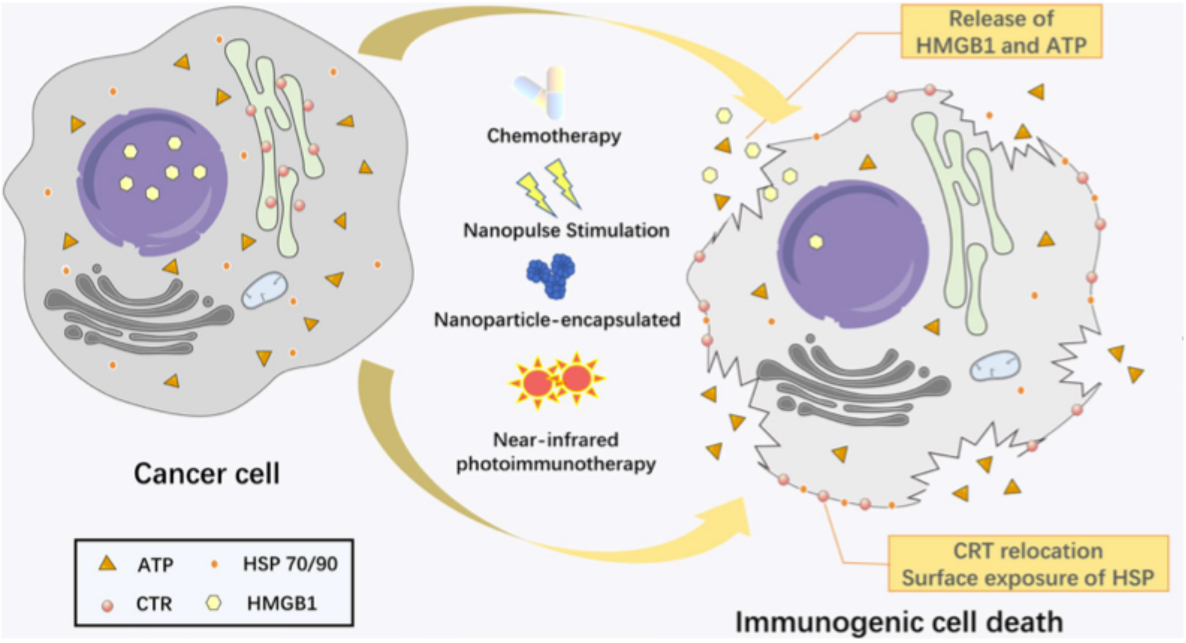

Figure 22: Schematic representation of the induction of immunogenic cell death (ICD). After treatment with e.g., ionizing radiation, cancer cells are induced to undergo apoptosis. This leads to swelling and bursting. Then, the dying cells release damage-associated molecular pattern (DAMPs). One example of a DAMP is the translocation of the protein calreticulin from the endoplasmatic reticulum to the cell surface. (Zhou et al., 2019).

In recent years, pre-clinical and clinical research has revealed what is known as the abscopal effect of radiation therapy (from the Latin ab Scopus, meaning away from the target) (Huang et al., 2019). The abscopal effect is a systemic anti-tumor immune response. After ionizing radiation, we can have a regression of non-irradiated metastatic lesions at a distance from the primary site of irradiation (Liu et al., 2018). This is not a common effect of radiation therapy, in fact, a recent literature review of abscopal effects of radiation therapy reported only 46 cases of abscopal effect between 1969 and 2014. Thus, the abscopal effect has remained obscure and ignored up until the advent of cancer immunotherapy (Rodríguez-Ruiz et al., 2018). The abscopal effect is believed to be induced by immunogenic cell death (ICD), further discussed below.

In 1994, Polly Matzinger proposed what is known as the "danger theory" which states that the immune system can distinguish between dangerous and innocuous endogenous signals (Krysko et al., 2012). It was shown that dying, stressed or injured cells release molecules on their cell surface which functions as danger signals for the innate immune system. These danger signals were later known as damage associated molecular patterns (DAMPs). ICD (seen in Figure 22) is defined by chronic exposure of DAMPs in the tumor microenvironment (Zhou et al., 2019). Some DAMPs are secreted or released as adenosine triphosphate (ATP) and high mobility group protein B1 (HMGB1), while other DAMPs are exposed on the outer plasma membrane on the cells, such as the protein calreticulin. ATP acts like a "find-me" signal while HMGB1 acts as a danger signal resulting in the secretion of pro-inflammatory cytokines. The protein calreticulin acts as an "eat-me" signal and promotes the uptake of irradiated tumor cells by antigen-presenting cells such as dendritic cells and phagocytic cells. After activation by DAMPs, T cells, especially CD8+ T cells, play a major role in the anti-tumor immune response. Once activated, these begin to propagate and circulate through the blood stream where they are able to destroy cancer cells in unirradiated parts of the body (hence the abscopal effect) (Liu et al., 2018).

What is worth noticing is that most of the DAMP molecules do not function as immunological signals when they are inside the cells, only when the DAMPs are exposed on the cell surface or when DAMPs are secreted. A new hypothesis for improving today's cancer treatment is to use radiation to stimulate secretion/translocation of DAMPs to signal to the immune system that the cancer cells are dangerous. Hence, radiation could function as an in-situ vaccine. However, the abscopal effect also depends on the dose and fractionation regime. Today, the convention is to use 1.8 – 2.2 Gy per fraction, but it has also been shown that higher doses per fractionation could potentially be a better option to induce abscopal effects (Liu et al., 2018). However, too high doses could counteract the abscopal effect, demonstrating the need for more research on how to induce abscopal effect and how it can be implemented in cancer treatment.

2.4.2 Calreticulin

This section is based on the article “Functional Roles of Calreticulin in Cancer Biology” (Lu et al., 2015).

Calreticulin was identified in 1974 as a soluble protein in the lumen of the endoplasmatic reticulum (ER) and the structure of calreticulin can be seen in Figure 23. Calreticulin is typically retained in the ER but has also been identified in the cytosol and on the cell surface (Dudek and Michalak, 2018). Calreticulin is a chaperone protein, which sequesters calcium and prevents misfolded proteins from leaving the ER to name a few (Golden et al., 2014). A more detailed overview of the roles of calreticulin can be seen in Table 4.

This highly conserved, 46 kD Ca^{2+}-binding protein has three domains followed by a four-amino acid ER retention sequence (KDEL) at the carboxyl terminus (Krysko et al., 2012). According to an article by Lu, Weng and Lee, structural predictions of calreticulin demonstrated that the protein is composed of three domains; N-domain, P-domain and C-domain (Lu et al., 2015).

The N-domain is a globular domain containing eight antiparallel β-strands. These β-strands can interact with α-intergrins and DNA-binding site of steroid receptors. The disulfide bond formed by cysteine residues in the N-domain of calreticulin may interact with the P-domain to generate important chaperone function of calreticulin. The P-domain is composed of multiple copies of two types of repetitive amino acid sequences which form the lectin-like chaperone structures. These structures are responsible for the protein-folding function of calreticulin. In addition, the P-domain is also a high-affinity and low-affinity capacity Ca^{2+}-binding region. The last domain, C-domain, is a highly acidic region which is important for Ca^{2+}-buffering functions. It binds to Ca^{2+} with, unlike the P-domain, high capacity and low affinity manner. It is known that Ca^{2+} binding to this region plays a critical role in the interaction with other chaperone proteins in ER. Also, there is a KDEL sequence for retrieval of the calreticulin already destines to be transported out of the ER-lumen at C-terminal of calreticulin, as seen to the right in Figure 23, and due to this, calreticulin is a protein which is highly enriched within the ER lumen.

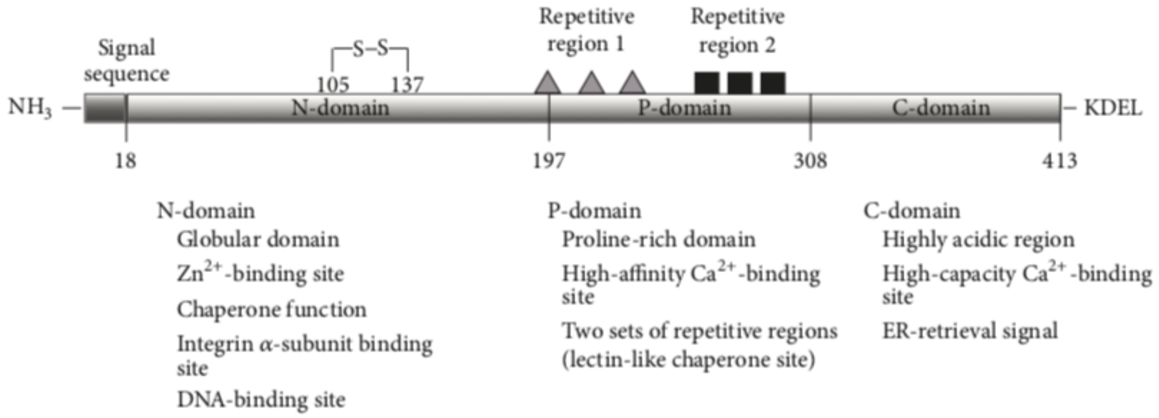

Figure 23: The figure represents a schema of the structure and supposed functions of calreticulin and shows the three domains: N-domain, P-domain and C-domain. There is a signal sequence at N-terminal and a KDEL ER retrieval peptide at C-domain. (Lu et al., 2015).

In the ER lumen, calreticulin performs two major functions: chaperoning and regulation of Ca^{2+} homoeostasis and signaling. Calreticulin also assists in the proper assembly of major histocompatibility complex class I molecules (MHC1) and the loading of antigen (Krysko et al., 2012). In addition to this, calreticulin also has other functions outside of the ER, including cell migration and adhesion, RNA stability, and cell proliferation (Martino, 2017).

As stated above, calreticulin on the surface of the cell is considered as a so-called “eat-me” signal and promotes phagocytic uptake of cancer cells by the immune system. Calreticulin exposed on the cell surface play an important role in the destruction of cancer cells by triggering an immune response. Also, several studies have shown that calreticulin expression levels were positively correlated with tumorigenesis and most of them have indicated that tumor tissues express a higher level of calreticulin in comparison to normal tissue (Martino, 2017). There have been studies on the alteration of calreticulin expression in lung cancer, ovarian cancer and urinary tract cancer and several types of cancer have shown higher expression of calreticulin (Harada et al., 2017). This includes acute myeloid and lymphoblastic leukemias, non-Hodgkin lymphoma, bladder cancer, glioblastoma and ovarian cancer (Chao et al., 2010).

Table 4: A list over the functions of calreticulin, adapted from Emma Thingstads master thesis, and adjusted. (Thingstad, 2019).

Function	Action
Protein chaperone	CRT helps with the correct folding of proteins, prevents the

	proteins from being exported from the ER to the Golgi apparatus
Calcium homeostasis	CRT is a Ca^{2+} regulator
Cell migration and adhesion	CRT is crucial in regulating the cell migration through focal contact dependent manners and regulating cell adhesion and migration through various mechanisms
RNA stability	CRT works as a novel mRNA binding protein by being a transacting factor
Phagocytic signal	CRT works as a signal to induce phagocytic uptake in dying cancer cells
Cell proliferation	CRT has been found to upregulate or downregulate cell proliferation depending on cell type

2.4.3 CGAS/STING Pathway

This section is based on the article "cGAS/STING Pathway in Cancer: Jekyll and Hyde Story of Cancer Immune Response" (Bose, 2017) and the article "DNA sensing by the cGAS-STING pathway in health and disease" (Motwani et al., 2019).

The innate immune system deploys a variety of sensors to detect signs of infection. Nucleic acid represents a major class of pathogen signatures, for example viruses that can trigger robust immune responses (Cai et al., 2014). DNA in the cytoplasm of mammalian cells act as a danger signal which activate an innate immune response. How these cytosolic DNA trigger an immune response was unclear up until recently, when it was shown that DNA sensing by the newly discovered cGAS-cGAMP-STING pathway triggers the immune system as well as autoimmunity, through the pathway discussed below.

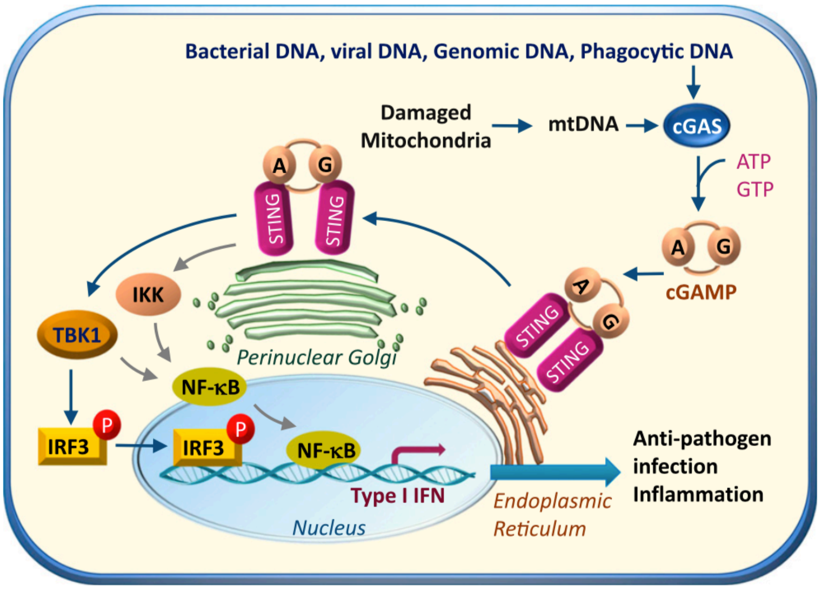

Figure 24: The figure shows how the activation and regulation of the cGAS/cGAMP/STING pathway works in cells. The cGAS is activated by viral and bacterial DNA, and also by mitochondrial DNA and phagocytosed DNA localized in the cytosol of the cell. Once the cGAS is activated, it uses ATP and guanosine GTP as substrates to catalyze the formation of the second messenger, cGAMP, which will bind to the STING localized on the endoplasmatic reticulum (ER). Once the cGAMP has been bound to STING, it promotes STING translocation from the ER to the Golgi apparatus. During this translocation of STING, STING recruits and activates TBK1. TBK1 will then in turn activate the phosphorylation and nuclear translocation of IRF3 and NF-κB. NF-κB can also be activated by the IκB kinase (IKK), which can lead to increased synthesis of IFN and other inflammatory genes. This will lead to DNA-driven immune response, such as host defense, inflammation and tumor immunity. See the text for a more detailed description of the cGAS/STING pathway. (Bai and Liu, 2019).

The DNA-sensing cyclic GMP-AMP synthase (cGAS) is an example of a nucleic acid sensor. Together with its second-messenger product cyclic GMP-AMP (cGAMP) and the cGAMP sensor, Stimulator of Interferon Genes (STING), it forms a major DNA-sensing mechanism in the cytoplasm of mammalian cells. During infection with cytosolic bacterial pathogens and some DNA viruses, the cGAS-cGAMP-STING pathway will be activated and lead to the transcriptional induction of type I interferons and the nuclear factor-κB-dependent expression of proinflammatory cytokines. The activation of STING also activates additional cellular processes. The DNA sensor cGAS is activated by DNA through direct binding, as seen in Figure 24. This will trigger conformational changes that induce enzymatic activity. It is worth mentioning that any DNA, both non-self and self, can cause an activation of the cGAS, but the length of the DNA is of importance. If there is a short length of the DNA, of approximately 20 base pairs (bp), it can bind to the cGAS, but longer double stranded DNAs with a length larger than 45 bp can form more stable ladder-like networks of cGAS dimers which result in stronger enzymatic activity. Active cGAS converts guanosine triphosphate (GTP) and ATP into cyclic GMP-ATP (cGAMP), which is an endogenous second messenger. It contains unusual mixed phosphodiester linkages between the 2'-hydroxyl group of GMP and the 5'-phosphate of AMP. In addition, it contains linkage between the 3'-hydroxyl group of AMP, and the 5'-phosphate of GMP. This forms a novel 2',3'-cGAMP isomer.

The 2',3'-cGAMP isomer product binds to STING which is an endoplasmatic reticulum (ER)-localized adaptor. In addition, STING can bind to cyclic dinucleotides produced by bacteria directly. In general, the 2',3'-cGAMP isomer is thought to bind with higher affinity to STING than to bacterial cyclic dinucleotides. This suggests that STING is more strongly activated when the cGAS receptor is engaged. Furthermore, STING undergoes a conformational change upon cGAMP binding. Two wings of the STING protein are brought into juxtaposition with the ligand situated deep inside the binding pocket. Also, a lid consisting of four anti-parallel beta-sheet strands is rearranged on top of this binding pocket. This results in a closed conformation. This will lead to a 180-degree rotation of the ligand-binding domain and leads to formation of STING oligomers through side-by-side packing of dimeric STING molecules.

2.4.4 Micronuclei

This section is based on "Micronuclei in genotoxicity assessment: from genetics to epigenetics and beyond" (Luzhna et al., 2013) and "Cytokinesis-block micronucleus cytome assay" (Thomas and Fenech, 2011).

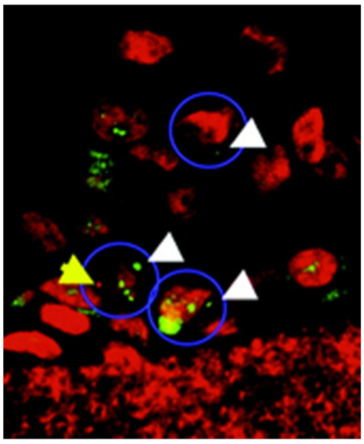

Figure 25: The figure shows micronucleated cells in the artificial human 3D Air-100 epithelial tissue. Nucleic and micronuclei are stained with propidium iodide which is the red color. The blue outline is micronucleated cells. The green color is micronuclei positive for $\gamma - H2AX$. (Luzhna et al., 2013).

Micronuclei are tiny extra-nuclear bodies originating from acentric chromatid/chromosome fragments or whole chromatids/chromosomes that lag behind at the anaphase of dividing cells and are not included in the main nucleus during telophase (see Figure 25). Instead, they are enwrapped by the nuclear membrane and resemble the structure of the daughter nucleus, although being much smaller in size (Luzhna et al., 2013).

To form an acentric chromosome fragment, DNA DSBs should either occur in one sister chromatid or extend to the whole anaphase chromosome. This only happens when the level of DSBs exceeds the misrepair capacity of DSBs repair or in the case of the dysfunctional of homologous recombination or defects in enzymes of the non-homologous end-joining (NHEJ) pathway. Chromosome malsegregation during anaphase is another way of the formation of micronuclei. Malsegregation of sister chromatids usually happens due to the absence or inappropriate attachment of spindle microtubules to chromosome kinetochores. Stable amphitelic microtubule attachments generate tension at kinetochores, locking the correct chromatid orientation in place. Unstable microtubule-kinetochore attachments such as syntelic (i.e., both sister chromatids are attached to the same spindle pole), monotelic (i.e., only one kinetochore is attached leaving the second sister chromatid unattached), or merotelic (i.e., one kinetochore is attached to both spindle poles) do not result in significant tension, thus making the bond sensitive to dissociation. If this is not corrected, such attachments lead to inappropriate segregation and chromosome loss, thus resulting in aneuploidy and micronucleus formation. See Figure 26 for an overview of the formation of micronuclei.

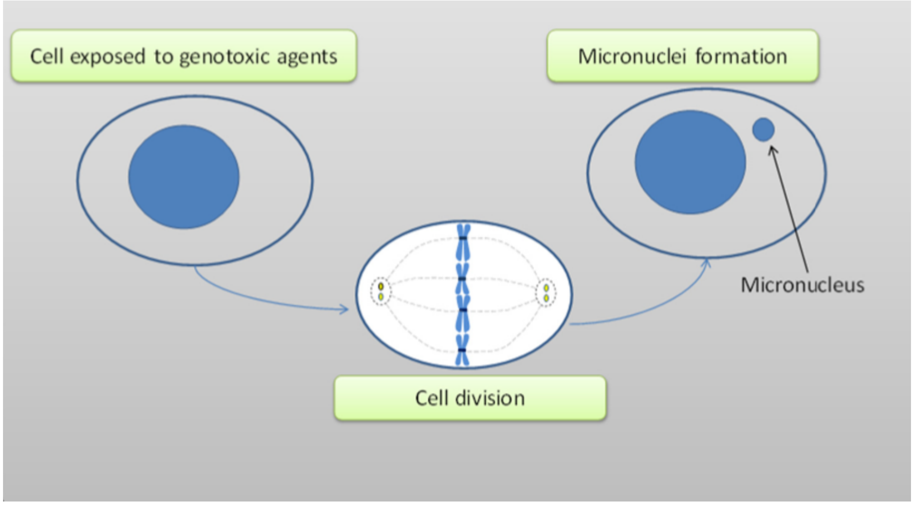

Figure 26: The figure shows a very simplified version of the formation of micronuclei in the cell after being exposed to genotoxic agent, such as ionizing radiation.. (Luzhna et al., 2013).

To be able to measure the chromosomal damages and scoring (i.e., counting) of micronuclei, the micronucleus technique was proposed by Fenech and Morley in 1986, called the cytokinesis-block micronucleus (CBMN). Here they used cytochalasin-B (Cyt-B) which is an inhibitor of the spindle assembly, to prevent the cytoplasmic division after the nuclear division has occurred (Sommer et al., 2020). The inhibition by Cyt-B allows one to discriminate between cells that did not divide after treatment and cells that did, thus preventing the confounding effects caused by differences in cell division kinetics (El-Zein et al., 2008). The CBMN assay was proven to be more efficient in studying X-ray-induced chromosomal aberrations than other methods. The main advantage of the CBMN assay is its ability to differentiate micronuclei formed as a result of clastogenic or/and aneugenic treatment. By blocking the cells at the binucleated stage it is possible to recognize the chromosomal loss, breakage and nucleoplasmic bridges. If the cell is allowed to divide, the nucleoplasmic bridges disappear. The CBMN method allows accumulating virtually all cells at the binucleated stage regardless of their division kinetics which makes the CBMN assay highly sensitive.

A variety of genotoxic agents may induce formation of micronuclei leading to cell death, genomic instability or cancer development. The potential of ionizing radiation to directly or indirectly cause damage to DNA is a good example of a genotoxic agent. Understanding of the mechanisms of the micronuclei formation induced by genotoxic agents is therefore of great significance for both the detection of diseases such as cancer and their treatment. Dawson and Bury found in a study that irradiation of lymphocytes in vitro caused a linear relationship between the dose and micronucleus induction (Luzhna et al., 2013). They also proposed the micronucleus technique as a method for measuring chromosomal damages caused by cytotoxic agents in vivo.

The role of ionizing radiation in micronuclei production is relatively well understood. The production of micronuclei in human lymphocytes after X-ray irradiation was observed at the time of the first mitosis, 48 hours after the culture was started. The frequency of micronuclei was much lower when the fractionated dose of X-rays was applied. X-rays and UV light caused a dose-dependent micronuclei induction with a slope factor of 1.8 and 10.3 for X-rays and UV light respectively. Individuals predisposed to cancer tend to form micronuclei more rapidly than persons without hereditary history. The ultimate test of the CBMN Cyt assay is its ability to predict disease outcomes prospectively. The Human Micronucleus project completed a cohort study involving 6718 subjects from ten countries, screened for micronuclei frequency between 1980 and 2002, showing a significant increase of all cancer incidence was found for subjects in the groups with medium and high micronuclei frequency relative to those with low micronuclei frequency. These initial results indicate the potential predictive value of the CBMN Cyt assay with respect to cancer risk, hence micronuclei screening may serve as a valuable method in predicting cancer.

Micronuclei have defect membranes which easily break down exposing double-stranded DNA (dsDNA) to the cytosolic DNA sensor cyclic GMP-AMP synthase (cGAS) which is a pattern recognition receptor (Rodríguez-Ruiz et al., 2018). Following activation by aberrant cytosolic DNA, the enzyme cGAS produces the mammalian 2’,3’-cGAMP, which in turn activates the STING protein and thereby lead to the production of Type I interferon (IFN) and other pro-inflammatory cytokines which boost the immune response (Bose, 2017). The accumulation of dsDNA in the cytosol of irradiated cancer cells activates canonical defense pathways which are hard-wired in the immune system, and chiefly rely on CD8 T-cell activation to clear viral infections. Similarly, successful antitumor immunity elicited by ionizing radiation mediated by the cGAS/STING pathway in the irradiated tumor, and relies on activation of anti-tumor CD8 T-cells (Rodríguez-Ruiz et al., 2018).

2.5 Dosimetry

This section is based on “Handbook of Radiotherapy Physics” (Mayles, 2007) and “Introduction to radiological physics and radiation dosimetry” (Attix, 1986).

2.5.1 Ionization Chamber

Radiological physics is the study of ionizing radiation and how ionizing radiation interacts with matter, with special interest on the energy absorbed when ionizing radiation traverse through matter (Attix, 1986). Dosimetry has to do with determination of energy which is absorbed. The absorbed dose, defined in equation 7, may be determined by using what is known as ionization chambers. There are several different types of chambers, from small to large, but they are based upon similar concepts. The ionization chamber has a cavity that contains a sensitive medium, usually air, surrounded by a conducting material and with a central collecting electrode (anode and cathode, respectively). The radiation beam will ionize the gas in the ionization chamber and the resulting charged particles will create a current that can be related to the dose.

Applying a voltage over the cathode and anode, an ionization chamber will collect the ions from ionizing interactions. It is the gas volume within the cathode-anode system that define the mass in the delivered dose. Over this volume, the energy imparted (given in equation 6), is the number of ionizations times the average released energy. The ionization energy required to create an ion pair is given as $\overline{W}$. The ionization chamber measures the number of ions of negative charge M (for Measurement), and the energy imparted ϵ can be calculated as M x $\overline{W}$. Still, to get an accurate dose, the ionization chamber will need to be calibrated. It is important that it is properly calibrated by a certified calibration laboratory to reduce the uncertainties to a minimum. The calibration constant is given as:

$$N_{D,w} = \frac{D_w}{M} \tag{12}$$

Where D_w is the known dose to water and M is the ion chamber reading. To get the absorbed dose, assuming the dose-response is linear, we multiply the ionization chamber reading with the calibration constant.

2.5.2 Calibration

A primary standard of estimating absorbed dose to water for high energy photon and electron beams, offers the possibility of reducing the uncertainty in the dosimetry of radiation therapy beams (International Atomic Energy Agency, 2000). Based on such a standard, a coherent dosimetry practice is possible for practically all radiotherapy beams. The International Atomic Energy Agency (IAEA) published in 2000 a technical report series no. 398, which advises multiple corrections to the calibration constant (International Atomic Energy Agency, 2000). The calibration is only valid for the conditions at the time of the calibration, which means that differences in radiation source and the different conditions in the ionization chamber must be corrected for to get the accurate dose. In IAEA TECHDOC 1455, the absorbed dose to water at 5 cm depth in water, in a medium energy kilovoltage X-ray beam of quality Q and in the absence of the chamber, is given by equation 13 (International Atomic Energy Agency., 2010):

$$D_w = M_u N_k k_u \left(\frac{\mu_{en}}{\rho}\right)_{w,air} p_u \tag{13}$$

Where M_u is the reading of the dosimeter corrected for influencing quantities such as pressure and temperature. P_u is the perturbation factor of the ionization chamber for in-phantom measurements at the beam quality Q. N_k is the calibration constant for the ionization chamber, k_u is a correction for the difference in energy distribution in the beam as it travels through a phantom. (μ_{en}/ρ) is the mean mass-energy absorption coefficient, water to air. The correction constant, which is the correction factor for the differences in pressure and temperature, is given by equation 14:

$$k_{tp} = \frac{(273.2 + T)P_0}{(273.2 + T_0)P} \tag{14}$$

Where T_0 and P_0 are the temperature and pressure under the calibration at the standard laboratory while T and P are the conditions outside of the reference conditions. For the work performed during the work of this thesis, the influencing quantities are temperature and pressure that varied compared to the standard atmospheric conditions.

2.6 Methods of Analysis

2.6.1 The Flow Cytometer

The following section is mainly based on “Flow Cytometry: basic principles and applications” (Adan et al., 2017) and “Guidelines for the use of flow cytometry and cell sorting in immunological studies” (Cossarizza et al., 2017).

Cytometry is, in the simplest form, the measurement of cell characteristics. It was first used in the 1950s to measure the volume of cells in a rapidly flowing fluid stream as they passed in front of a viewing aperture, and todays modern flow cytometers are able to make measurements of cells in a solution as they pass by the instrument’s laser at rates of 10.000 cells per second or more. It is said that “the marriage between immunology and cytometry is one of the most stable and productive in the recent history of science” which clearly mark the importance of using flow cytometry in immunological studies (Cossarizza et al., 2017). Today, the flow cytometer can be used to measure the fluorescence intensity which are produced by fluorescent-labeled antibodies detecting ligands which bind to specific cell associated molecules (one example being propidium iodide (PI) which binds to DNA) and proteins, such as the protein calreticulin (abcam, 2020).

A schematic overview of the flow cytometer can be seen in Figure 27. The flow cytometer includes the cell sample, the fluid dynamics that move the sample into the flow cytometer, the laser system**,** and the optics that gather the lights. The detectors sense the light, and a computer system will process and output the data.

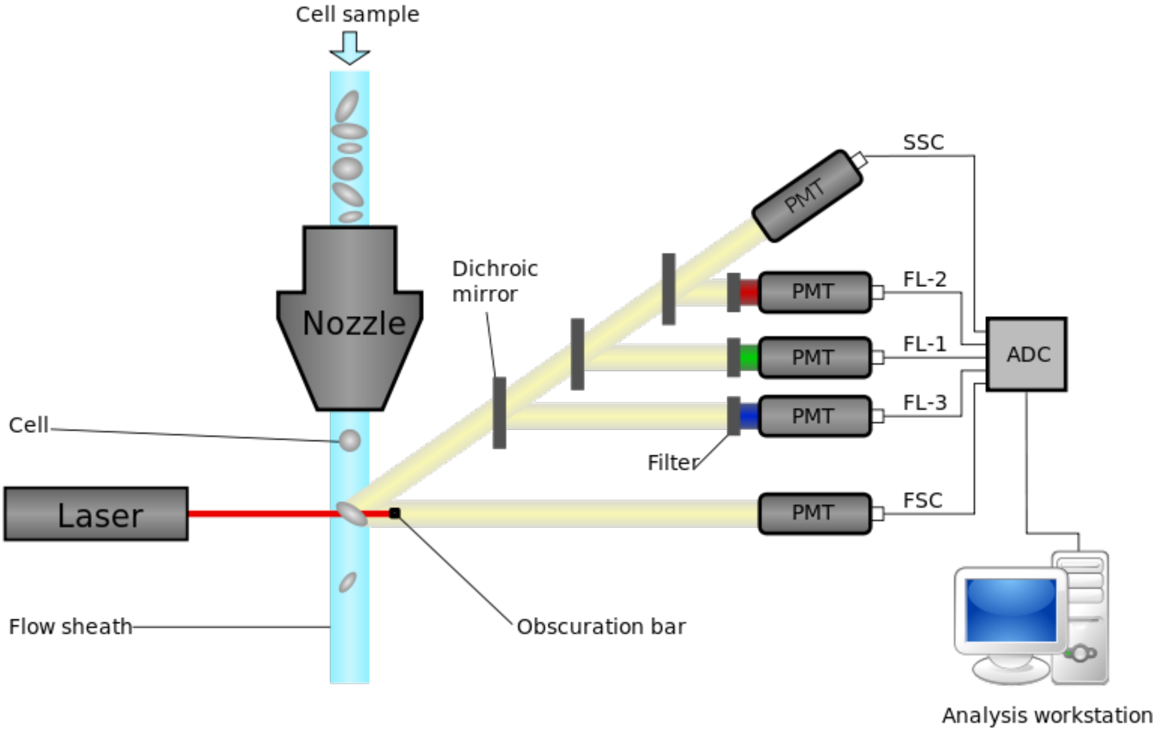

Figure 27: A schematic overview of the flow cytometer system. The laser can be seen on the left. The cells are in the cell sample and are sent through the nozzle so that single cells are irradiated by the laser. The bandpass filters are used to distinguish between different wavelength spectra and assign them to the corresponding photomultiplier tubes (PMTs). FSC corresponds to forward scatter and SSC corresponds to sideward scatter. Finally, the collected measurements are then processed and displayed on the computer where the data is ready to be analyzed by a data program. (Kierano, 2012).

Once a suspension of individual cells has been prepared for flow cytometry analysis, the prepared sample is placed on the flow cytometer. The machine will suck up the sample, mix the sample into a stream of saline solution sheath fluid in the cytometer, and lead the cell suspension through a narrowing channel so that we get individual cells passing through the laser at the interrogation point. As each cell passes through the laser beam, the laser beam will scatter in multiple directions. The flow cytometer detects light scattered in a forward manner direction, called forward scatter (FSC), and light scattered in a sideways manner direction, called sideways scatter (SSC). See Figure 28 for a schematic view of how FSC and SSC are used to characterize the size and granularity of the cell. The amount of FSC light for each cell is detected by a detector on the far side of the cell from the laser. FSC is proportional to the size of the cell. The amount of SCS is detected by a detector located perpendicular to the path of the laser beam. Side scatter is proportional to the shape and internal complexity of a cell. By analyzing the forward and side scatter data together, we can look at the size, shape and complexity of the cells. In addition, the analysis of the forward and side scattered data, can allow us to divide the (heterogeneous) population of cells into individual populations with varying size, complexity and shape. This makes us able to analyze multiple populations within a sample and this is the true strength of the flow cytometer technique.

In addition to separating cells based on the FSC and SSC, we can also separate the cells based on the expression of a particular protein. One example being the protein calreticulin. Here, a fluorochrome is often used to stain the protein we are interested in. The fluorochromes used for the detection of target proteins will emit light when excited by a laser with the corresponding wavelength. We then detect these fluorescent stained cells (or particles) individually. The FSC and SSC light, as well was fluorescence from the stained cells, is then split into defined wavelengths and channeled by a set of filters within the flow cytometer. The fluorescent light which is emitted will be filtered so that each sensor will detect fluorescence only at a specified wavelength. These sensors are called photo multiplying tubes (PMTs) (abcam, 2020). The PMTs will convert the energy of a photon into an electrical signal (a voltage). Analog-to-digital converters will process these voltage pulses to digital data, which can be plotted as histograms or plots.

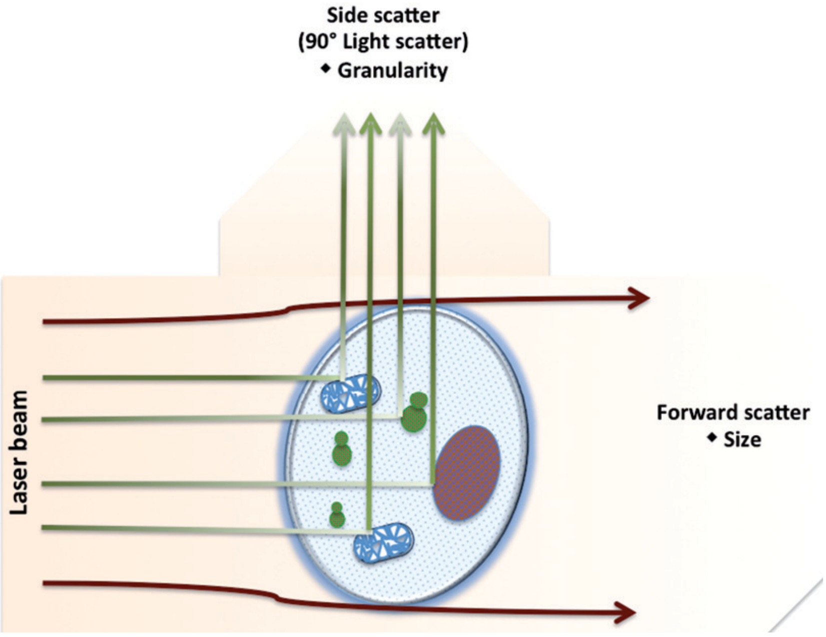

Figure 28: The laser beam coming in from the left, hitting the cell, and we get forwards scatter (FSC) and sideward scatter (SSC). FSC is proportional to the cell size while SSC is proportional to cell granularity or internal complexity of the incoming cell. (Adan et al., 2017).

2.6.2 Confocal Laser Scanning Microscopy

The following section is based on the book "Fluorescence Microscopy: From Principles to Biological Applications" (Kubitscheck, 2013).

The use of microscopy can be dated back to the 17th century, when Robert Hooke published the book Micrographia in 1665, and Hooke is considered to the father of optical microscopy (Hooke, 1667). In the late 1950s, Marvin Minsky invented the confocal microscope which was a new type of microscope and the principle of a confocal aperture is illustrated in Figure 29.

In conventional widefield fluorescence microscopy, the entire sample, e.g., a cell or a cell nucleus, is flooded evenly in light from a light source. Fluorochromes in all parts of the sample can be excited at the same time and the resulting fluorescence, just like in the flow cytometer, can be detected by the microscope's photodetector. The resulting image becomes the sum of the image throughout the sample depth, both those in the focal plane and those outside the focal plane. If the depth of field (DOF) is large, that is if the distance between the upper and the lower region of the focus region is large, out of focus light will not be a problem. However, if samples are imaged at high magnification, we require a low DOF and the out of focus light can become a problem.

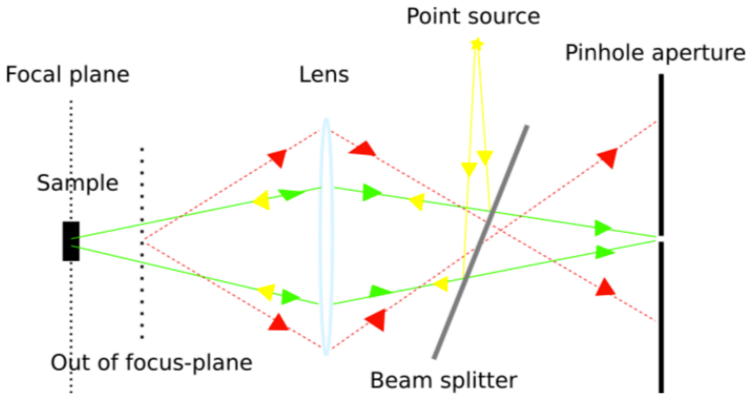

Figure 29: A schematic overview of the beam path from point source to sample, and from sample to the confocal aperture (pinhole) in a confocal laser scanning microscope. The confocal aperture allows only the in-focus light to reach the detector, giving a higher resolution. Illustration by Ingunn Hanson. (Hanson, 2018).

Minsky's solution to this was to develop a new microscope as illustrated in Figure 29. Instead of illuminating the whole sample at once (as in widefield microscopy), he scanned the sample point by point. For this to happen, the excitation light and the detector had to be in focus coincidentally – they had to be "confocal", hence the name confocal microscopy. By further implementing pinholes in the excitation pathway, Minsky was able to block the light which did not come from the focal region and in confocal microscopy only the emission light that passes through the pinhole is detected by a photomultiplier to form the final image. Because of this, the image optical resolution is much better in confocal microscopy compared to widefield microscopy. However, in addition to block the light which does not come from the focal region, the pin hole also blocks much of the light from the sample's fluorescence. The signal intensity will therefore be decreased. When using a pinhole aperture, we therefore require a stronger excitation light intensity to achieve the desired amount of fluorescence due to the blocking of the light and often we require longer exposure time. It is worth noting that when using a strong excitation light intensity to achieve the desired amount of fluorescence, it can cause phototoxicity which is defined as "damage inflicted on cells by light, in the presence of a photosensitizer and molecular oxygen" (Kubitscheck, 2013). Another aspect of confocal microscopy that needs to be considered when using confocal microscopy, is photobleaching. Photobleaching is a process of gradual loss of florescence intensity of the specimen of interest, arising from interaction between the exiting light and the fluorescent compound. Note that photobleaching will eventually happen to all fluorophores which are being exposed to excitation light, but it can be reduced using fluorophores which are more photostable and optimization of the intensity of exciting light.

In confocal microscopy, since only one point in the sample is illuminated at a time, to be able to get a full image, the imaged spot must be scanned across the sample. A microscope that scans across the sample and scans the focused emission-collection spot is called a confocal laser scanning microscope (CLSM). This is done by scanning the beam across the sample in the horizontal plane by using one or more oscillating mirrors. CLSM usually has a low reaction latency and the scan speed can be varied. However, it is important to keep in mind that slower speed provide a better signal-to-noise ratio (SNR) which results in better contrast in the final image. You can also scan the stage on which the sample sits but moving the sample can cause disturbances which in turn can distort the final image, especially in tissue samples. It is therefore usually preferred to move the laser instead of the stage, even though this can cause aberrations by the lenses.

Using pinholes to direct the laser beam will create an "optical section" within the sample. The microscope is then very efficient at rejecting out of focus fluorescent light and the result is that your final image comes from a thin section of the sample you are investigating, i.e., you have a small depth of field. It is the size of the pinhole which determines the depth of the optical section and it is measured in Airy Units (AU). The larger the AU, the wider the pinhole, and you get a thicker optical section. By scanning many thin sections of your sample, you can build up a three-dimensional image of the sample which can be useful in many settings.

3 Materials and Methods

3.1 Tumor-Cell Line and Techniques

The experiments performed during the work of this thesis have been carried out at the cell laboratory at the department of Biological and Medical Physics, University of Oslo (UiO).

3.1.1 Cell Line

A primary culture is defined as the first passage of cells or tissue in a culture where the cells survive for more than 24 hours. A cell line is defined as cells first established in a primary culture, which have been sub-cultivated at least once (Kielberg, 2001). A cell line can be used for research purposes. The cells used in the work with this thesis are A549 cells, which are established human epithelial lung carcinoma cells originating from a study by Donald J. Giard et al. (Giard et al., 1973). A549 cells originate from a 58-year-old Caucasian male and were purchased from the American Type Culture Collection. The A549 cells were chosen as they previously indicated a higher sensitivity to cell membrane bound calreticulin after X-ray irradiation (Thingstad, 2019). Two experiments running the calreticulin assay were conducted using T98G cells. T98G cells derive from a human glioblastoma multiforme tumor and originate from a 61-year-old Caucasian male (Stein, 1979). The T98G cells were also purchased from the American Type Culture Collection.

3.1.2 Cell Cultivation and Seeding: Medium and Growth Conditions

Cell Flasks

The cells were grown in cell flasks of various size, T25 (25 cm^2) or T75 flasks (75 cm^2) (Nunclon, Denmark), all depending on the required format of the experiment. The T25 flasks were used for the samples receiving irradiation and the T75 flasks were used for the control cells receiving no irradiation. In the finalized cytokinesis-block micronucleus (CBMN) assay, removable chamber slide (coverglass) (Nunk, Germany) is to be used. The coverglass allows the cultivation and analysis of cells directly on the microscope slide and coverglass is useful when Trypsin cannot be used to loosen the cells from the flask. After the cells were seeded into flasks they were placed on a sterile tray and put in the sterile CO_2 incubator which held 37°C (discussed more below).

The Medium

A medium that meets the basic requirements for the content of vitamins, salt, glucose and amino acids is called a basal medium (Kielberg, 2001). A basal medium should fulfill certain demands to maintain the right pH value, buffer capacity and osmolarity for the cells to grow in vitro. The medium in which the cells are grown, should imitate the fluid the cells are surrounded by in vivo. During the work with this thesis, the A549 cells were maintained in a BioWhittaker 1:1 mix of Dulbecco's Modified Eagle's Medium (DMEM) and F12 with 15 mM Hepes and L-glutamine which provides the right amount of nutrients, vitamins and inorganic salts for the cells to grow. Using this 1:1 combination of DMEM/F12 is common as DMEM is a nutrient heavy with amino acids, glucose and vitamins, and the F12 compliments the DMEM medium with a broad spectrum of vitamins and trace elements (Kielberg, 2001). In addition, 10 % of fetal bovine serum was added to the DMEM/F12 mix to provide missing growth factors and mitogens intended to stimulate cell growth and proliferation (Kielberg, 2001). To control the bacterial contamination, a mix of penicillin/streptomycin was also added to the medium. Prior to use, the bottle of DMEM/F12 medium was preheated for approximately 15 minutes in Grant JB Aqua 18 water bath set to 37°C.

The pH Level

During the incubation of the cells, a close eye was kept on the color of the medium in the cell flasks. Cells are optimally grown with a pH around 7.2 – 7.5 (Kielberg, 2001). To control the pH level in the cell flasks, a pH indicator was added to the cell medium. Also, if the cells were to be kept in the incubator for a long period of time, half of the medium was changed prior to the irradiation (approximately two hours prior) to maintain the appropriate pH level and maintaining enough nutrition for the cells to grow, divide and live.

The Buffer Solution

We aim to maintain the conditions for the cells in vitro as close to those in vivo, so to avoid large fluctuations in the pH level in the cell medium, the medium also contains a buffer system. The blood content of bicarbonate is through the capillary system of the lungs in equilibrium with the content of CO_2 in the lung air while maintaining a pH of approximately 7.4 (Kielberg, 2001). In open systems, the pH level is kept close to constant by incubating the cells in an incubator which keeps the CO_2 level at 5 %. A balanced salt solution consists of inorganic salts with glucose added and is often used together with the basal medium. This salt solution also functions as a buffer, maintaining the pH level at approximately 7.4 (Kielberg, 2001). Note that if a balanced salt solution is to be used alone, for example when resuspending the cell suspension, it should contain phosphate instead of bicarbonate to prevent pH changes when in contact with atmospheric air (Kielberg, 2001). This solution is called phosphate buffered saline (PBS) (Lonza, Belgium), and PBS is used in the assays included in this master thesis.

Trypsin

To loosen the cells from the cell flaks, pre-heated Trypsin with EDTA (Lonza, Belgium) was used. Trypsin is a proteolytic enzyme which cleaves the protein bonds between neighboring cells, and between the cells and the substrate on which they are attached. Trypsin was used when cells needed to be diluted due to their growth in the cell flask and in the assays performed in this thesis to loosen the cells from the cell flasks to be made into a cell suspension. The Trypsin used contains EDTA (Trypsin-EDTA) which enhance the effect of the Trypsin by binding Ca^{2+}-ion which the intracellular bindings between the cells are dependent on (Kielberg, 2001). For experiments that required more careful handling of the cells, TrypLE (Thermo Fisher Scientific Nunc A/S, Denmark) was used. TrypLE is highly purified, recombinant cell-dissociation enzyme which replaces porcine trypsin. TrypLE reagents are ideal for dissociating attachment-dependent cell lines in serum-containing as well as serum-free conditions. Another benefit is that it can be directly substituted for Trypsin without protocol changes (Thermo Fisher Scientific, 2020).

3.1.3 Cell Cultivation and Seeding: Seeding, Sterility and Incubation

Seeding

The experiments performed during this master thesis lasted for two to three days. The cells required to perform the experiments were ordered from Joe Alexander Sandvik, Ingunn Hanson, Anne Marit Rykkelid or Julia Marzioch at the department of Biological and Medical Physics, UiO. My work included only irradiation, incubating and analysis of the cells, no seeding of the cells.

Sterility

When working with cells in the laboratory, sterility is an important factor. Microorganisms such as bacteria, virus and fungi divide approximately fifty times faster than human cells and will easily outgrow a cell culture (Kielberg, 2001). Working at the cell lab required strict routines which were to ensure sterile conditions. All the equipment and chemicals were sterilized before use, using 70 % ethanol which is highly effective towards bacteria and fungi (Kielberg, 2001). Work that required the cells to be in contact with air (or solutions that were used when working with the cells which also were in contact with air) was mainly performed in the Laminar Air Flow (LAF) bench (Gelaire, Australia and Safe 2020, Thermo Scientific). In this LAF bench, the air is filtered through a high efficiency particulate air (HEPA) filter. The HEPA filter removes particulates such as micro-organisms from the air so that the air in the LAF bench is kept sterile. If the cell flasks required incubation time, the flasks were only treated in the LAF bench to keep the flasks sterile. Prior and after use of the LAF bench, it was cleaned with Virkon 5 % (DuPont, UK). After the Virkon had dried, MilliQ water was poured on the surface of the LAF bench and dried off using clean paper. The LAF bench was then sprayed with 70 % ethanol. Before entering the LAF-bench, the equipment that was being used was always sprayed with 70 % ethanol. Unsterile gloves (Nitrile, VWR) were used during the experiments, and sprayed with 70 % ethanol before being in contact with cell flasks.

Sterile pipettes tubes (Sarstedt, France), a container holding pipette tubes (Sarstedt, Germany) and a jar for disposed medium were used during the work with this thesis. Glass and metal equipment were wrapped in aluminum foil and sterilized in a heating oven (Termaks, Bergen) in 180°C for two hours. Rubber equipment and lab coats were sealed in autoclave bags made of paper and autoclaved at 120°C for twenty minutes.

Incubation

During the incubation of the cells, the flasks or dishes were maintained in either a Thermo Scientific Steri-Cycle CO_2 incubator (Thermo Scientific Forma, USA), a Steri-Cult 200 CO2 incubator (Thermo Forma 3307, USA) or a Thermo Forma Series II, Water Jacketed CO2 incubator (Forma Scientific, USA) at 37°C. $37 - 37.5$°C is the optimal temperature for mammalian cells in vitro (Kielberg, 2001). Also, the humidity of the incubators was set to 90 % since to prevent the medium in the cell flasks to evaporate. If this were to happen, the osmolarity of the cell medium would increase. An increase in the osmolarity of 5 – 10 % will have a toxic effect on most cells (Kielberg, 2001). Since the aim is to maintain the conditions for the cells as close to those in vivo, the concentration of CO_2 was kept at 5 % to maintain the right pH value in the cell flask.

3.2 X-ray Irradiation

3.2.1 Preparation

All experiments with X-ray irradiation were performed at the X-ray laboratory in the basement of the chemistry building at UiO, room VK08. When the X-ray system (PANTAK PMC 100, Pantak, USA) is to be used, a warm-up of the system is required for it to better prepare the tube to receive a high heat load (Percuoco, 2014). Thus, turning on the X-ray unit approximately 20 minutes before irradiation of the cells was required. Also, the heater was turned on for the temperature in the irradiation chamber to reach 37°C.

The cells irradiated were transported from the third floor from the cell lab, KV342, to the basement and room VK08 of the Chemistry building. In order to keep the conditions as sterile as possible, a Styrofoam box was cleaned with ethanol and left for air drying before the flasks were placed inside of the Styrofoam box with a lid on during transportation of the cells. A cell flask with heated water was also placed in the Styrofoam box to keep the temperature as stable as possible. The time when the cell flasks were collected from the incubator and put back after irradiation was kept as short as possible. The lids of the flasks were tightly closed when collected from the incubator and kept closed during the irradiation of the flasks to keep the condition of the cells sterile and maintain the CO_2 level inside the flasks.

3.2.2 X-ray Irradiation

The room which houses the X-ray unit has multiple safety features to maintain the security of the users of the X-ray machine. The panels and the door surrounding the X-ray room are plated with lead to protect the people using the X-ray tube from radiation. A safety switch is also in place, meaning that if the door to the X-ray room is not properly closed, the power of the X-ray tube cannot be switched on.

In the X-ray chamber (as seen in Figure 30), multiple positions are possible for the flat Perspex board that holds the container with the cell flasks. This allows for different distances between the source of the field and the cells. All experiments performed during the work with this thesis used a source-to-detector distance of 60 cm, meaning that the distance between the field source (located at the top of the chamber) and the Perspex board was 60 cm. This distance was chosen since it gave a high enough dose rate and a homogenous radiation field. The irradiation chamber door was also connected to a safety trigger to ensure that the X-ray irradiation could only be turned on with the door closed. Inside the irradiation chamber, a heating system kept the system at 37°C at all times during the irradiation.

The container for the cell flasks can be seen in Figure 30. It is made of Perspex, contains four cavities in the shape of a T25 flask and was always preheated before placing cell flasks to keep a stabile temperature. Also, using Perspex, which has a low atomic weight material, will only perturb the irradiation field minimally by scattering. The container's contribution to the backscatter dose is insignificant (Das and Chopra, 1995).

Table 5: Irradiation time needed to achieve a set dose. The X-ray machine was operated with 220 V tube voltage and the tube current was set to 10 mA. A primary filtration with 1.52 mm aluminum and 0.50 mm copper was always used. The distance between the X-ray source and the Perspex board where the cell flasks were placed, held a skin source distance of 60 cm.

Time	Dose
3 minutes and 10 seconds	2 Gy
6 minutes and 21 seconds	4 Gy
9 minutes and 31 seconds	6 Gy
12 minutes and 42 seconds	8 Gy
19 minutes and 2 seconds	12 Gy

During the X-ray irradiations, the voltage was set to 220 kV for all experiments and the current was set to 10 mA. The irradiation time of the cells determines the dose given to the cells. See Table 5 for an overview of the time needed to get the desired dose. The standard filtration used was 1.52 mm aluminum and 0.50 mm copper.

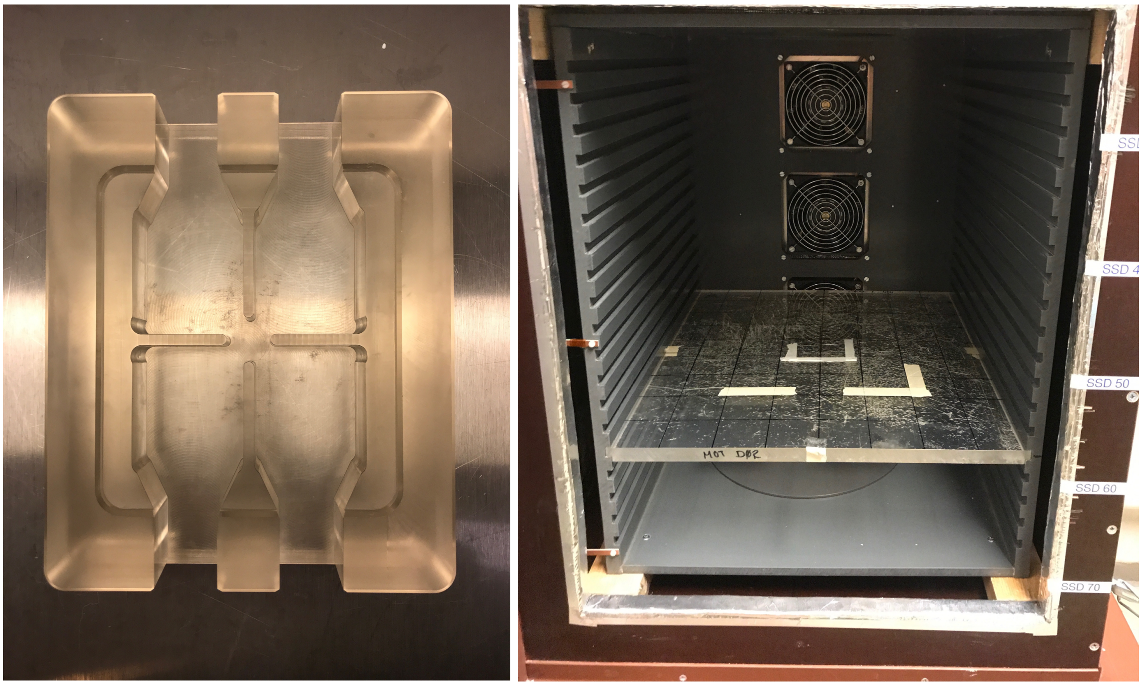

Figure 30: Left panel: the cell flask container which holds four T25 cell flasks. This container was preheated prior to use to maintain a stable temperature to prevent the cells from exiting the cell cycle. The right panel shows the irradiation chamber, with X-ray irradiation coming from above. The container to the left is placed on the Perspex plate seen in the right panel, which is placed 60 cm under the field source.

3.3 Cytokinesis-block Micronucleus (CBMN) Protocol Development

With regards to the cytokinesis-block micronucleus (CBMN), protocol development with an assay which stains and detects the cell membrane, cell nucleus and the micronuclei were to be established using confocal microscopy. Counting the number of micronuclei after ionizing radiation was also of interest. Only protocol development has been included in this thesis, no experimental data counting the micronuclei formation after ionizing radiation due to time constraints. In Appendix 7, a detailed overview of the different CBMN experiments testing different chemicals to stain the cell membrane, nuclei and micronuclei can be found.

3.3.1 Establishing a New Assay Protocol

The first steps of the protocol development of the CBMN assay were to find out how to stain only the cell nucleus and the micronuclei, making it possible to distinguish the nuclei and the micronuclei from the rest of the cell. Then, a method to stain the cell membrane in addition to the cell nucleus and the micronuclei was needed, as it proved difficult to see which nuclei and micronuclei belonged to the which cell. Several different chemicals were tested before the final protocol could be established. In the final protocol, cytochalasin B is added as a step in the protocol. Cyt-B prevents the cytoplasmic division after the nuclear division has occurred as we only want to count the cells with two nuclei since these have undergone cell division and possibly formed micronuclei in response to ionizing radiation (Sommer et al., 2020). The inhibition by Cyt-B allows one to discriminate between cells that did not divide after treatment and cells that did, thus preventing the confounding effects caused by differences in cell division kinetics (El-Zein et al., 2008). Note that Cyt-B does not stop karyokinesis, which means there will be a formation of binucleated cells with micronuclei present in their cytoplasm. However, in most cases, the usage of Cyt-B does not induce additional micronuclei, hence, the use of Cyt-B is recommended when performing the micronucleus assay (Sommer et al., 2020). Also, according to the mathematical model described by Fenech, micronuclei assays with Cyt-B applied to block the cytokinesis is superior over micronucleus assays without Cyt-B because it will lead to less false-negative results when using the CBMN assay (Sommer et al., 2020).

See section 3.3 for detailed description of the different steps of the CBMN protocol development. See Appendix 7 for a detailed overview of the different experiments conducted to establish the chemicals best suited for the CBMN assay.

3.4 Cytokinesis-block Micronucleus (CBMN) Assay

The detection of micronuclei was largely based on the protocol received from Anne Marit Rykkelid, the department of Biological and Medical Physics, UiO. See Appendix 2 for the final protocol to be used for the CBMN assay.

5 x 10^4 cells were seeded in coverglass flasks 24 hours prior to irradiation. Cytochalasin B (Cyt-B) (Sigma-Aldrich, Germany) was added to cell cultures at a final concentration of 3 $\mu g/ml$ right after irradiation. 24 hours later the medium was removed, and the cells were washed twice with PBS (37°C) and 1 mL working solution (1X in PBS) of CellBrite 488 (37°C) was added to coverglass flask. The coverglass flask was then incubated at 37°C for 30 minutes before the cells were washed twice with PBS (37°C). The cells were fixated with 2 mL methanol/glacial acetic acid (3:1) and incubated for 10 minutes. The cells were then washed twice with PBS. 1 mL NucSpot in PBS (1 $\mu L/ml$) was added to the coverglass before it was incubated for 10 minutes. The NucSpot 650 was removed from the coverglass flask, the coverglass was broken (e.g., you are left with only the cover slip), and the cells were left to dry under aluminum foil to avoid unnecessary exposure to light for approximately 30 minutes.

The cells were then mounted with approximately 5 - 10 µL VectaShield Mounting Medium (Vector Labs, USA). Note that this is an oil which can loosen the cells when left for long, so the amount of VectaShield Mounting Medium should be as small as possible. A cover slip was added and nail polished was used to fixate the cover slip on the glass. Each sample was directly analyzed in the confocal microscopy, making sure they were always wrapped in aluminum foil when not being analyzed. Also, the light in the room VK12 at the Chemistry building, where the confocal microscopy is located, was kept off when the microscope slides were placed under the microscope.

3.5 Confocal Microscopy Analysis

All experiments which included the use of the confocal microscopy (Leica SP2, Germany) were performed at the department of Biological and Medical Physics, UiO, located in the basement of the Chemistry Building. In Table 6, a list of settings for the microscope can be found. These settings were established by trial and error and can be used as a rough guideline saving time when conducting more experiments in the future.

When obtaining the images from the microscope, images were taken in several planes to be able to reconstruct the cell in 3D. This is necessary to include all micronuclei surrounding the nucleus. To reconstruct the cell in 3D, the height of the cell was measured using the confocal microscope (seeing where the cell begins and ends) and deciding how many images were needed to reconstruct the cell in 3D. This was typically between 7 and 12 images in the Z-direction.

Table 6: Confocal microscope settings used when scanning the coverslip where the A549 cells was mounted during the CBMN assay.

Channel	**4**
Laser wavelength	633 nm
Laser intensity	9 – 30 %
Detector range	660 – 720 nm
Detector gain	504 V
Pinhole size	180.13 µm

Zoom	8

3.5.1 CBMN Protocol Development: Micronuclei Counting

Manually counting the micronuclei after running the CBMN assay proved to be difficult, as the images obtained from the confocal microscopy showed what appeared to be few, or even no, micronuclei. Work began developing a data program which automatically masks out the micronuclei and counting the number of. This was done by Dr. Stefan Schrunner, the department of Biological and Medical Physics, UiO. Several methods were implemented into the software program by Dr. Stefan Schrunner. The implementation is based on existing R packages. This includes preprocessing of the image, where Gaussian blur was applied to smoothen the image to reduce noise artefacts. Then, the image gradient was calculated using a Sobel operator to identify large changes in the pixel values, and thresholding was applied using Otsu's method to obtain a binary image (i.e. a black and white image) (Wikipedia contributors, 2020b). Foreground-background separation was also applied, and the idea behind it is that with thresholding alone, the binary image will still be blurry, i.e., a lot of single white pixels in black neighborhood and vice versa. This is minimized using the DBSCAN-clustering method (Wikipedia contributors, 2020a). Postprocessing of the data was also implemented in the software program, with the final goal being able to mask out the micronuclei and separate the micronuclei from noise and other artefacts. Note that this program is in the early stages, and it will need further development before an automated counting of the micronuclei is possible.

3.6 Calreticulin Protocol Development

The detection of membrane bound calreticulin was largely based on the protocol received from Adrian Eek Mariampillai and his team of the Radiation Biology and DNA Damage Signaling group at the Institute for Cancer Research at Radiumhospitalet. This protocol was later adapted by Emma Thingstad during her work with her master thesis in the fall of 2018 and spring of 2019 (Thingstad, 2019). The protocol needed further adjustments to fit our experiments to be able to investigate the immune response in A549 cells after X-ray irradiation.

Since the experiments are done on live cells and the aim is to measure the membrane bound calreticulin expression, no fixation or permeabilization steps are included in the protocol for calreticulin detection.

3.6.1 Establishing a New Assay Protocol

When it comes to the calreticulin assay, the aim is to measure the amount of cell surface membrane bound calreticulin after ionizing radiation. To do so, the fluorescence intensity of the irradiated cells is measured and compared to the fluorescence intensity of the cells which does not receive radiation. Using what is known as fluorescent cell barcoding makes it possible to measure the relative fluorescent intensity. Individual cell samples are barcoded (or stained) with unique signature of fluorescent dyes. These barcoded cells can be mixed together with the irradiated cells, and analyzed as a single sample (Krutzik et al., 2011). This makes it possible to separate the irradiated cells and the control cells by the amount of barcode, and using equation 15, makes it possible to calculate the fluorescence intensity:

$$Ratio = \frac{Irradiated\ (p+s) - Irradiated\ (s)}{Control\ (p+s) - Control\ (s)} \tag{15}$$

where "irradiated" represents the cells receiving X-ray irradiation with a certain dose and "control" represents the cells not receiving any X-ray irradiation. "p" and "s" represents the primary and secondary antibody respectively.

Following the original protocol, where DyLight Alexa Fluor 650 (Thermo Scientific, Germany) was used as barcode, made it impossible to separate the unirradiated cells from the irradiated cells after running the sample through the flow cytometer. Instead, it was decided to use DyLight Alexa Fluor 488 (DyLight) as the barcode. Several months was spent trying to find the appropriate staining of the control cells to differentiate them from the irradiated cells. See Appendix 4 for a detailed list of the calreticulin protocol development trying to establish the right concentration of the DyLight. In the end, the correct concentration of DyLight to be used as a barcode was established. This made it possible to separate the control cells from the irradiated cells. The focus could then be shifted towards gathering experimental data after ionizing radiation, i.e., measure the membrane bound calreticulin level after X-ray radiation.

3.7 Calreticulin Assay

The cell suspension sample was analyzed 48 hours post X-ray irradiation. The cells which did not receive irradiation (the control cells) were flushed with 7.5 ml Phosphate Buffered Saline (PBS), then trypsinized with 4 ml TrypLE and incubated for about 4 minutes in the incubator holding 37°C. The control cells were then suspended to single cells with 2 ml pipette and 10 ml cell medium DMEM/F12 was added to the cell suspension before they were centrifuged for 4 minutes with 200xg. The control cells were then stained (barcoded) using 3 µl DyLight mixed with 350 µl medium for approximately 30 minutes in the dark.

The cell receiving X-ray irradiation were flushed with 7.5 ml PBS, then trypsinized with 2 ml TrypLE and incubated for about 4 minutes in the incubator holding 37°C. The cells were then made into a cell suspension with 4 ml of the complementing cell medium DMEM/F12. The irradiated cells were centrifuged (Beckman, USA) and resuspended in PBS. The barcoded cells were then added to the cell suspension containing irradiated cells, and each sample was split into two. After the splitting, the cell suspension was washed with PBS, centrifuged, washed with PBS and put on ice.

When the cells have been split, the next step of the calreticulin assay is to add the primary antibody, Anti-Calreticulin antibody ab2907, rabbit polyclonal (abcam, UK), to half of the samples (not including the control sample). The samples which are to receive the primary antibody are stained with ab2907 in bovine serum albumin (BSA) in PBS. The other split samples were not given the primary antibody, instead the samples were given the same volume PBS with BSA. Both the samples stained with the primary antibody ab2907 and the samples resuspended in PBS with BSA, were then incubated for 30 minutes in the dark, on ice. After this, the samples were washed twice with PBS before the secondary antibody, Alexa Fluor 647 goat anti-rabbit IgG (abcam, UK), was added to both samples. The samples were then incubated for 30 minutes in the dark on ice, followed by two washing steps with PBS. The samples were resuspended in PBS with BSA and put on ice, and immediately transported to the lab where the flow cytometry was located.

Right before running the flow cytometer analysis, 0.5 µl of 1 mg/µl propidium iodide (PI) (Thermo Scientific, Germany) was added to the cell suspension for live/dead staining. The final calreticulin assay can be found in Appendix 3. Note that each sample that was analyzed using the flow cytometer, contained a mixture of barcoded control cells which received no irradiation, and irradiated cells. Each sample containing the two cell populations had a complementary sample treated only with the secondary antibody. This was to correct for the signals which had unspecific bindings as well as autofluorescence, so that we are left with the relative fluorescence intensity based on the antibodies which only binds to the membrane bound calreticulin.

3.8 Flow Cytometry Analysis

The analysis of the detection of membrane bound calreticulin after X-ray irradiation was performed using the Accuri C6 flow cytometer (BD Biosciences, USA) which is located at the department of Biological and Medical Physics, UiO, room KV350b.

Table 7: Recommended channels in the flow cytometer for the specified fluorochromes. Adapted from Emma Thingstads master thesis and adjusted. (Thingstad, 2019).

Dye/antibody	Laser	Standard filters	Detector	Experimental use
DyLight 488 NHS-Ester dye	488 nm (blue)	533/30	FL-1	Barcoding
PI	488 nm (blue)	585/40	FL-2	Viability
-	488 nm	>670	FL-3	Not used
Alexa Fluor 647 goat anti	640 nm (red)	675/25	FL-4	Calreticulin (secondary antibody)

In Table 7, the recommended channels in the flow cytometer for the specified fluorochromes are listed. In the FL-1 channel of the flow cytometer, the fluorescence from DyLight is measured, used to distinguish between barcoded control cells and irradiated cells. The FL-4 channel was used to measure fluorescence from calreticulin-bound antibodies. The FL-2 channel was used to separate the dead cells from the live cells based on the uptake of proprium iodine (PI).

3.9 Statistical Analysis: The Mann-Whitney U Test

When data has been collected, one must interpret the data correctly. The data must be checked to see if there is an apparent relationship which is significant or just simply a coincidence. Several methods can be used to analyze data, such as the well know t-test. The t-test is also known as a ‘parametric’ test because it requires an estimation of the parameters that define the underlying distribution of the data (Whitley, 2002). In the case of the t-test, these parameters are the mean and standard deviation that define the normal distribution.

On the other hand, it is possible to use ‘nonparametric’ methods. Nonparametric methods require no (or very limited) assumptions to be made about the data to be analyzed. There is a wide range of methods that can be used in different circumstances with regards to the nonparametric methods. One method is the Mann-Whitney U test (Wenstøp, 2003). It is also called the Wilcoxon rank sum test.

The Mann-Whitney U test is utilized when two independent random samples are taken from two populations. To use the Mann-Whitney U test, two assumptions are made:

1) The two population distributions are identical and have the same central location, called the median (Newbold, 2010) This is the central hypothesis which may be falsified with the test.
2) It is equivalent to the t-test, but the Mann-Whitney U test is used when the assumptions of the t-test are not met and then the data are ordinal (Hinton et al., 2014).

The Mann-Whitney U test ranks the data in a scale from the lowest to the highest and it compares the ranks between the two populations. The test calculates two so-called U values for the populations and provides us with statistics which state if there is significant difference between the two samples. The test the significance of the differences in the data sets, the smaller of the two U values is chosen and the probability of getting this value, under the null hypothesis with no difference between the groups, is calculated (Hinton et al., 2014). If the probability is lower than the chosen significance level ($p < 0.05$), it will result in the rejection of the null hypothesis and the data would be considered significantly different (Neely et al., 2003). If the U values for both the populations are the same, it means that the population samples are very mixed amongst the ranks. Hence, it is not possible to conclude that there is a significant difference between the two populations. In the present thesis, an online Mann-Whitney U test calculator was employed, which use a two-tailed hypothesis (Stangroom, 2020).

4 Results and Analysis

4.1 Measurements of Micronuclei

Appendix 7 shows an outline of experiments performed during the work of this thesis with regards to the cytokinesis-block micronucleus (CBMN) assay, using cytochalasin-B as a cytokinesis inhibitor in the final experiments. A total of twelve experiments were run. The subject of interest was to measure the number of micronuclei in A549 cells after ionizing irradiation. It was clear that protocol development was needed to be able to perform the intended measurements. Due to time constraints, no experimental data were retrieved. The dose given during the protocol development was 8 Gy X-rays given as one fraction.

4.1.1 CBMN Protocol Development: Nuclei Staining

Some of the figures in the following sections have been edited in Photoshop 2020 to enhance the brightness and color of the images in order to make it easier to see the images when reading this paper. Unedited versions can be found in Appendix 5.

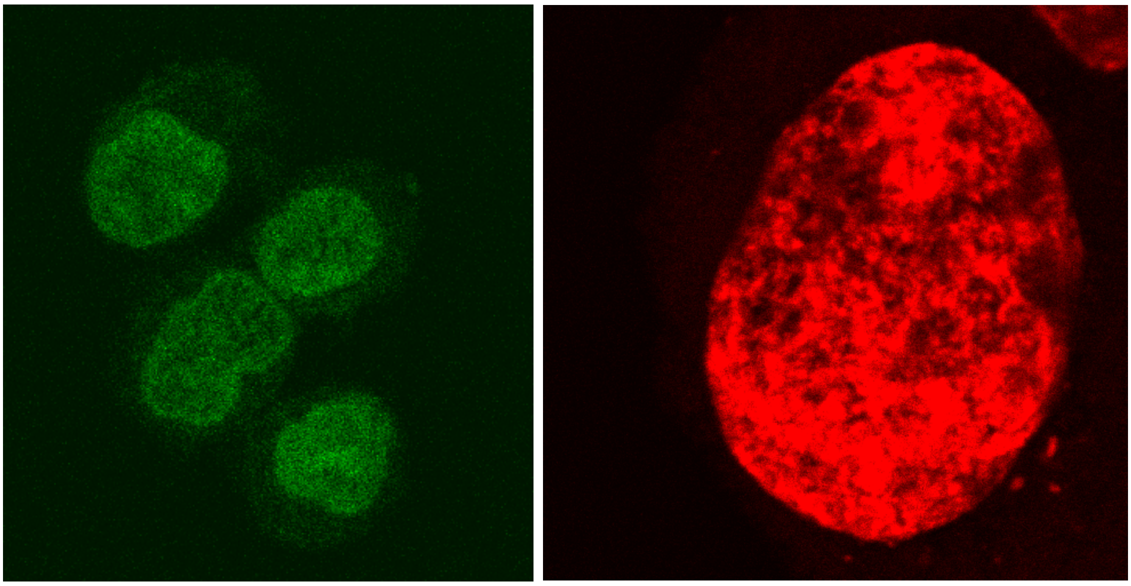

Figure 31: Left panel: the cell nuclei stained with PI and RNase. No micronuclei can be observed. Right panel: the cell nuclei were stained using NucSpot instead of PI and RNase. Micronuclei can be observed in the bottom right of the image. The cells were irradiated with 8 Gy X-rays.

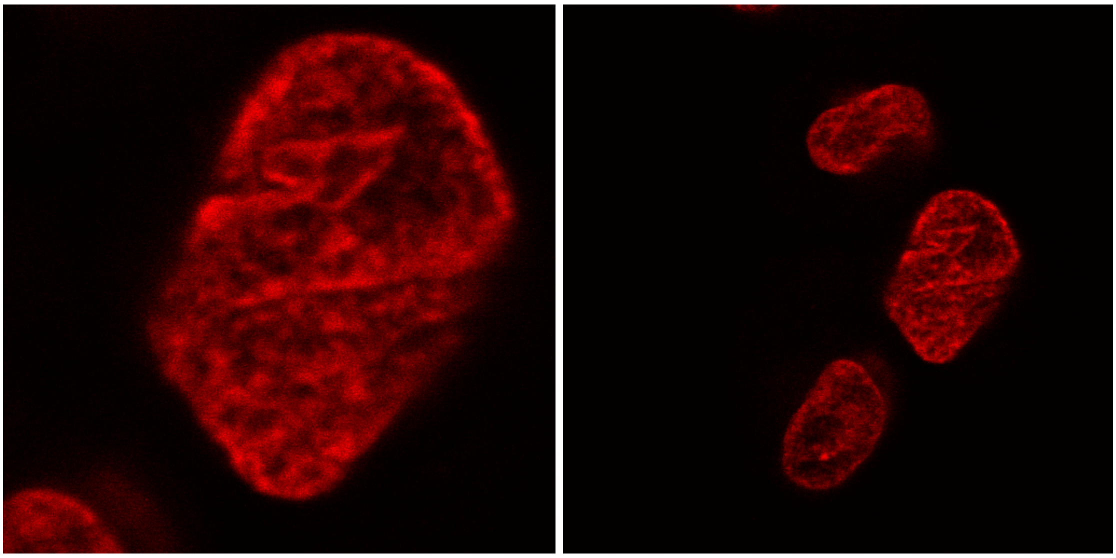

Figure 32: The figure shows the staining of the cells using NucSpot and RNase. Micronuclei cannot be observed. The cells were irradiated with 8 Gy X-rays.

Figure 31 and Figure 32 show some of the first data from the confocal microscopy analysis when trying to establish which chemicals were best for staining the cell nucleus and the micronuclei. Propidium iodide (PI) and ribonuclease (RNase) were first tried but did not give satisfactory results as the coloring of the cell nucleus was weak, and no micronuclei were observed (Figure 31, left panel). It was also problematic to establish whether it was the cell nucleus or the whole cell that had been stained. The next step was therefore to see if NucSpot Live Cell Nuclear Stain 650 (NucSpot) (Biotium, USA) with or without RNase would give a better result. The right panel in Figure 31 shows cells stained using NucSpot 650 only. Here, micronuclei can be observed at the bottom right.

In addition to staining with NucSpot, RNase was applied in the same experiment, and the results are shown in Figure 32. RNase removes the RNA in the cytosol of the cell, but not the DNA in the nuclei of the cell (Ingunn Hanson, personal communication, 2020). The hypothesis was that by using RNase, better contrast could be achieved by removing the background in the cytosol. This would make it easier to observe the micronuclei. However, adding RNase did not change the outcome. It was decided that NucSpot without RNase was the best choice for this assay to stain the nucleus of the cell and observe the micronuclei.

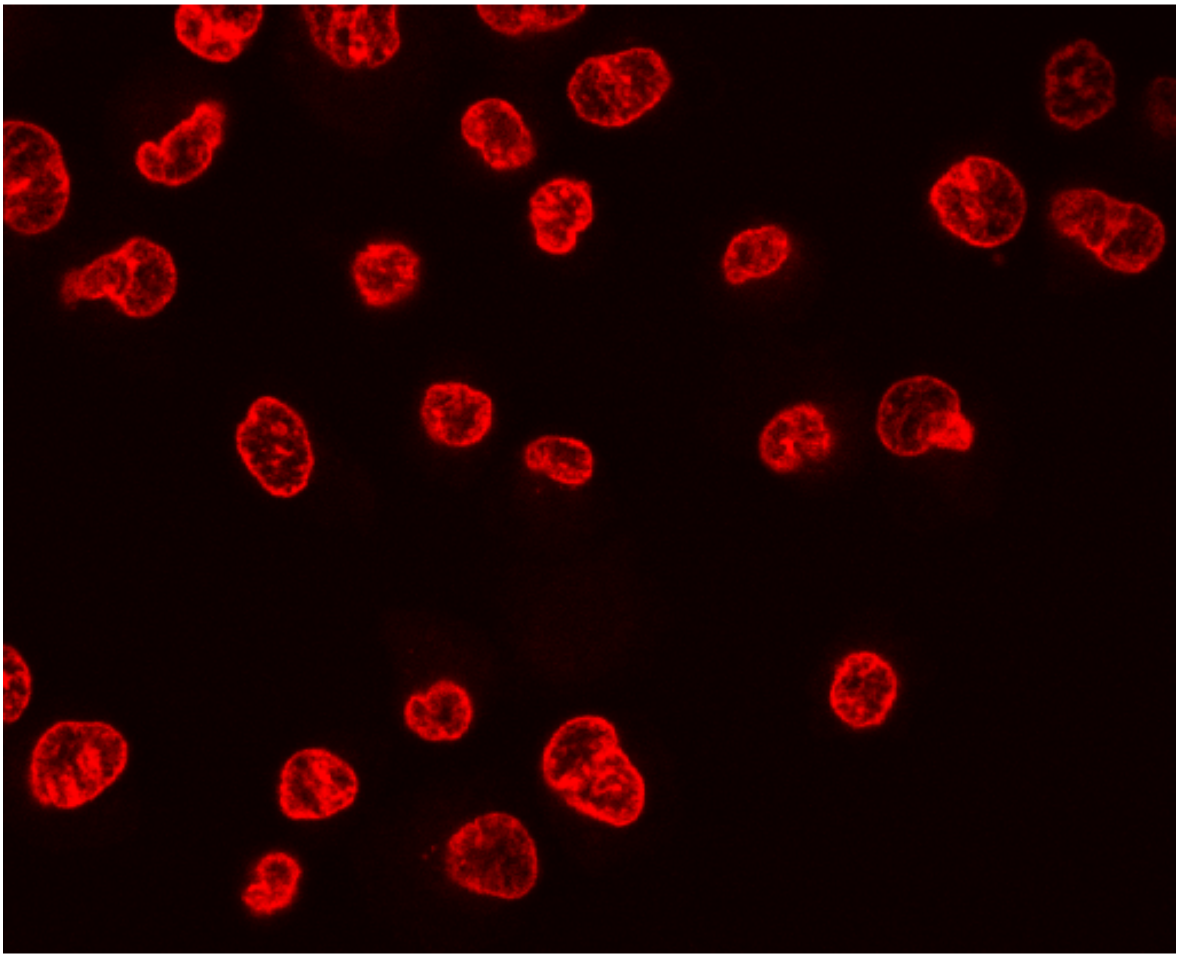

Figure 33: cells are stained using NucSpot and a few micronuclei can be observed after 8 Gy X-ray irradiation.

Figure 33 show the cells in the confocal microscope when only NucSpot has been used to stain the cells, and a dose of 8 Gy X-rays as one fraction was given. Micronuclei are visible. Figure 34 also shows the results of using NucSpot to stain the nuclei. It is difficult to establish whether more than one nucleus belongs to the same cell. Figure 33 and Figure 34 clearly demonstrates that in addition to staining the cell nuclei using NucSpot 650, an extra step in the protocol also staining the cell membrane is needed to separate each cell from one another.

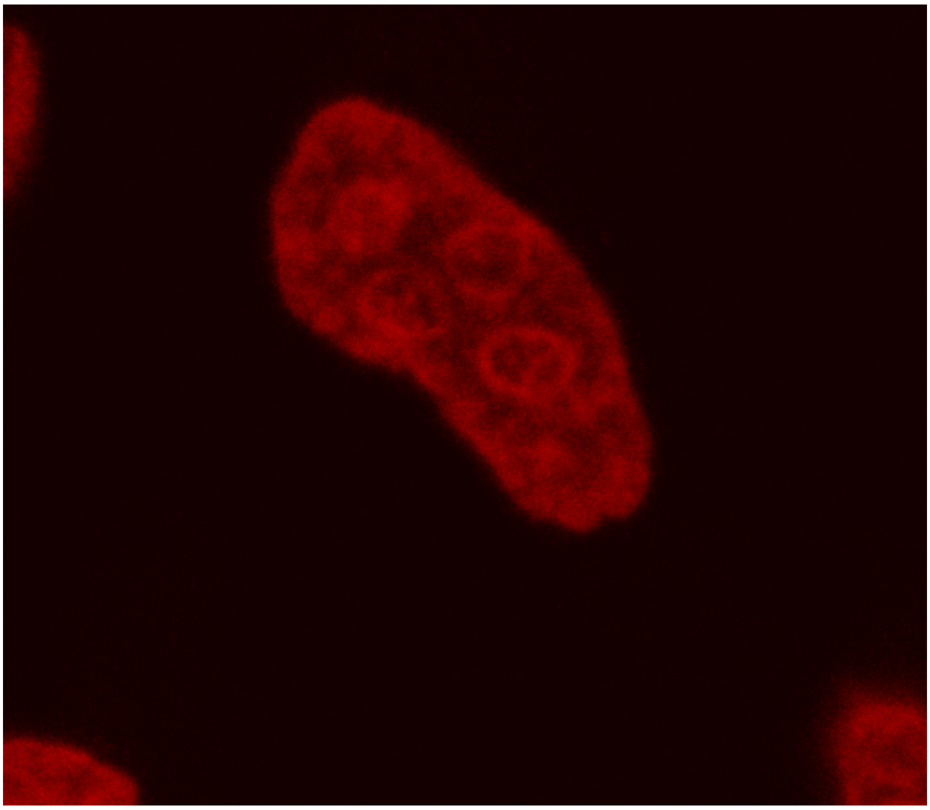

Figure 34: The cell nuclei staining using NucSpot 650 without the cell membrane color CellBrite 488. The cells were not irradiated.

4.1.2 CBMN Protocol Development: Membrane Staining

CellBrite 488 (CellBrite) (Biotium, USA) was ordered for staining the cell membrane to be combined with NucSpot. CellBrite can tolerate detergent permeabilization and methanol fixation and could be incorporated into the existing protocol (Biotium, 2015). The dye must also be able to stay on the membrane for 24 hours after the staining. Other options did not withstand methanol and were only stable for 60 – 90 minutes, making them unsuitable for incorporating them into our CBMN protocol.

The same protocol using NucSpot to stain the nuclei was followed, only adding a step with the CellBrite to stain the cell membrane. First, we used T25 cell flasks and Trypsin to loosen the cells from the cell flask to obtain a cell suspension. The stained cells were dripped on coverglass for microscopy analysis. When imaging of the cells was obtained, there appeared to be no coloring of the cell membrane. The hypothesis was then that the Trypsin damages the cell membrane coloring. To be able to skip the Trypsin to loosen the cells, coverglass was used instead of T25 flasks. By using coverglass, it was possible to grow the cells directly on the coverglass without transferring the cells to a microscope slide. PBS was used to wash the cells. Using coverglass and PBS to wash the cells improved the results, and a clear membrane staining was obtained as well as a nucleus staining.

Note that when using confocal microscopy, only one laser can be used at a time to excite the fluorophore in use. Therefore, in the left panel of Figure 35, when both NucSpot and CellBrite have been used to stain the cell membrane and cell nucleus, only the CellBrite staining is visible as the confocal microscopy has been set to detect that fluorophore. The green, bright area surrounding what appears to be the cell membrane indicates that the cell membrane staining has worked.

In Figure 36, the right panel in Figure 35 and Figure 34 have been merged together in Adobe Photoshop. By using CellBrite we see the cell membrane (the green area) surrounding the cell nuclei (the red area). Note that it may look like it is a binucleated cell as the cell membrane has no clear outline to the bottom right of the figure, and a red area can be seen, which indicates a second nucleus within the cell. When using NucSpot to stain the cell nucleus and CellBrite to stain the cell membrane, Cytochalasin-B (Cyt-B) can be added to the cell suspension right after irradiation. Cyt-B prevents the cytoplasmic division after the nuclear division has occurred as we only want to count the cells with two nuclei since these have undergone cell division and possibly formed micronuclei in response to ionizing radiation (Sommer et al., 2020).

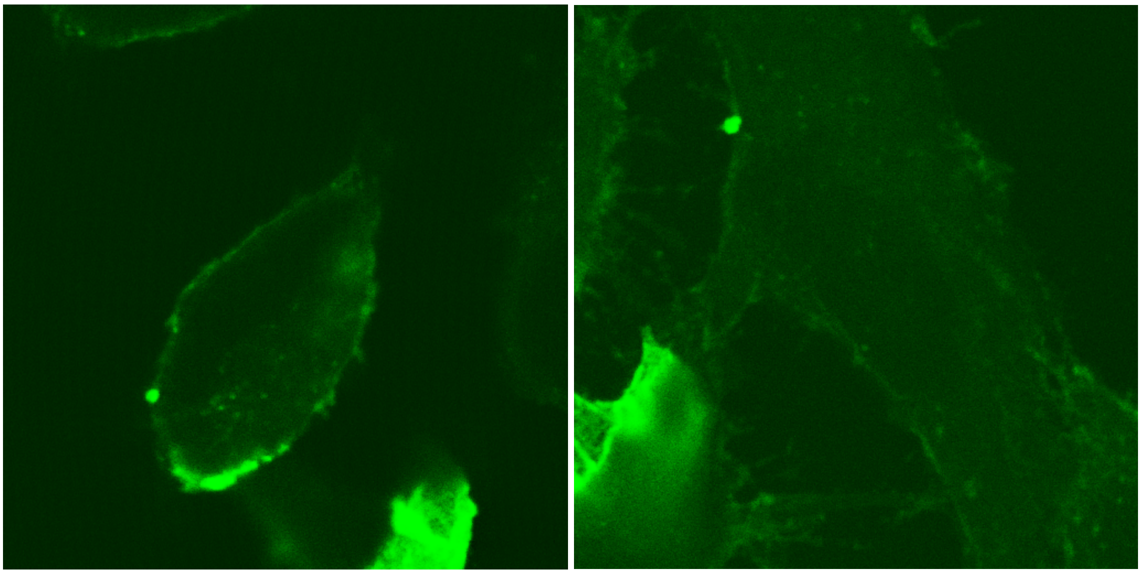

Figure 35: Both NucSpot 650 and CellBrite have been used to stain the cell. No nuclei can be seen, as the laser is only set to detect the CellBrite. Left panel: the outline of the cell membrane is visible, but there are brighter areas in the image, indicating that the staining did not work evenly in the cells. The same can be seen in the right panel. The cells were not irradiated.

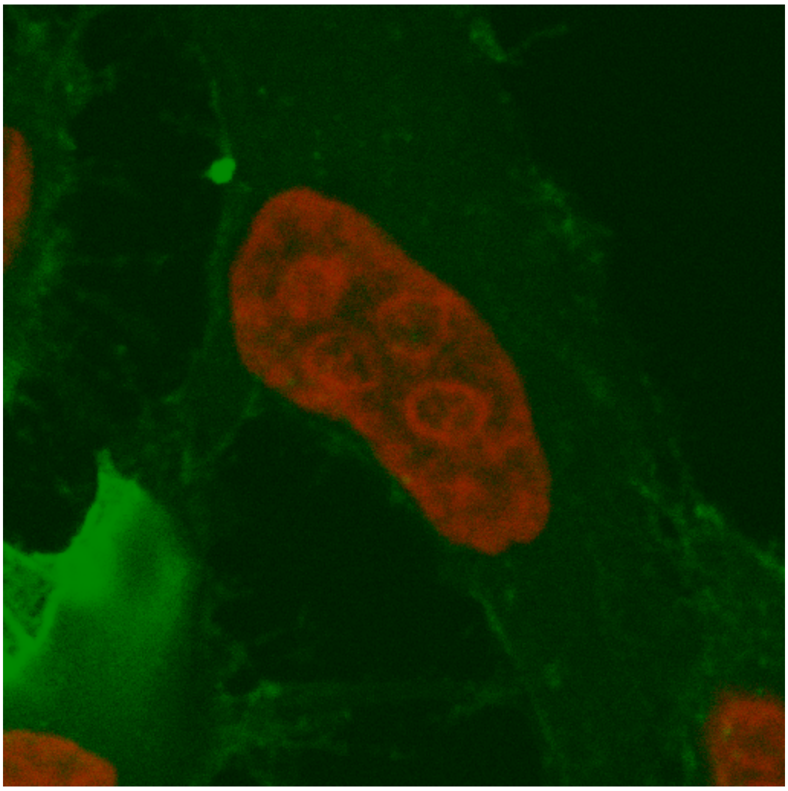

Figure 36: Figure 34 and the right panel of Figure 35 have been merged using Adobe Photoshop. The cell nuclei (red area) and the cell membrane (green area), using NucSpot and CellBrite, can be seen. The cells were not irradiated.

4.1.3 CBMN Protocol Development: Micronuclei Counting

After establishing NucSpot as the best choice for coloring the cell nucleus and micronuclei, and CellBrite as the best choice for coloring the cell membrane, the development of how to count the number of micronuclei began. The left panel of Figure 37 shows confocal microscopy of an A549 cell after 8 Gy radiation. Few, or no, micronuclei can be observed by manually counting. The right panel of Figure 37 shows the same image as in the left panel, after processing by a data analysis program written by Dr. Stefan Schrunner (described under section 3.5.1). An apparent increase in the number of micronuclei can be seen. It was obvious that counting the number of micronuclei by hand would not be accurate enough and highly time-consuming.

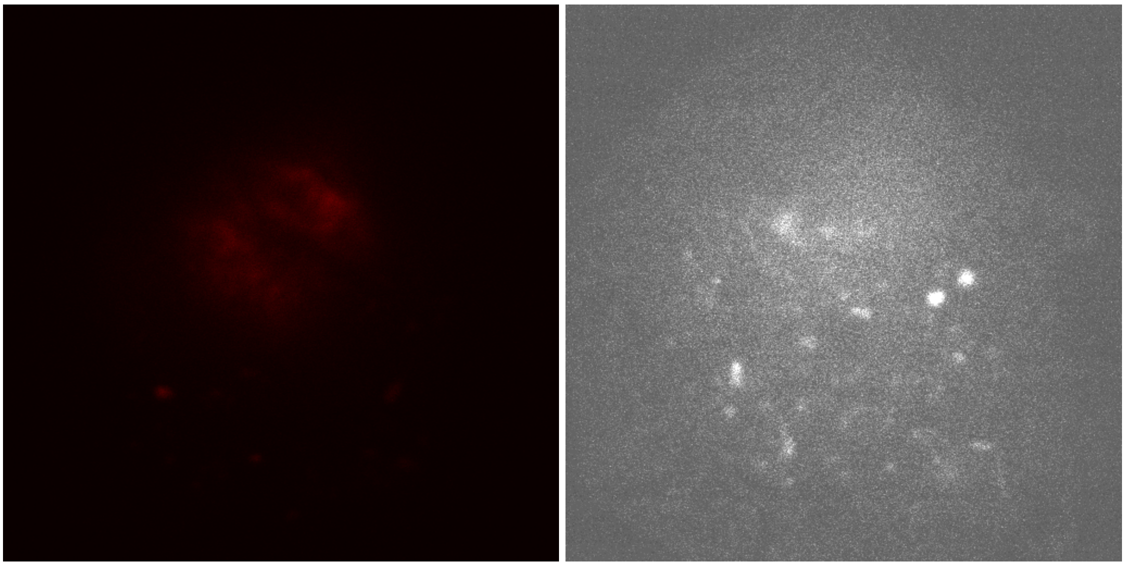

Figure 37: Left panel: confocal microscopy of an A549 cell after 8 Gy radiation. A small number of micronuclei can be observed, but visually it is not possible to detect the same number of micronuclei as in the right panel after image processing.

4.2 Calreticulin Protocol Development

Appendix 6 shows an outline of the calreticulin experiments performed during the work of this thesis. During the protocol development, the first dose given to the A549 cells was 2 Gy X-ray irradiation given as one fraction. It was then decided that one fraction of 8 Gy should be given in the following experiments.

Since the experiments were done on live cells, and the aim was to measure the membrane bound calreticulin expression, no fixation or permeabilization steps were included in the protocol for calreticulin detection. In total, twelve experiments were conducted to develop the calreticulin assay. In addition, 24 experiments were conducted to gather X-ray data to analyze the membrane bound calreticulin after ionizing radiation.

4.2.1 Autofluorescence

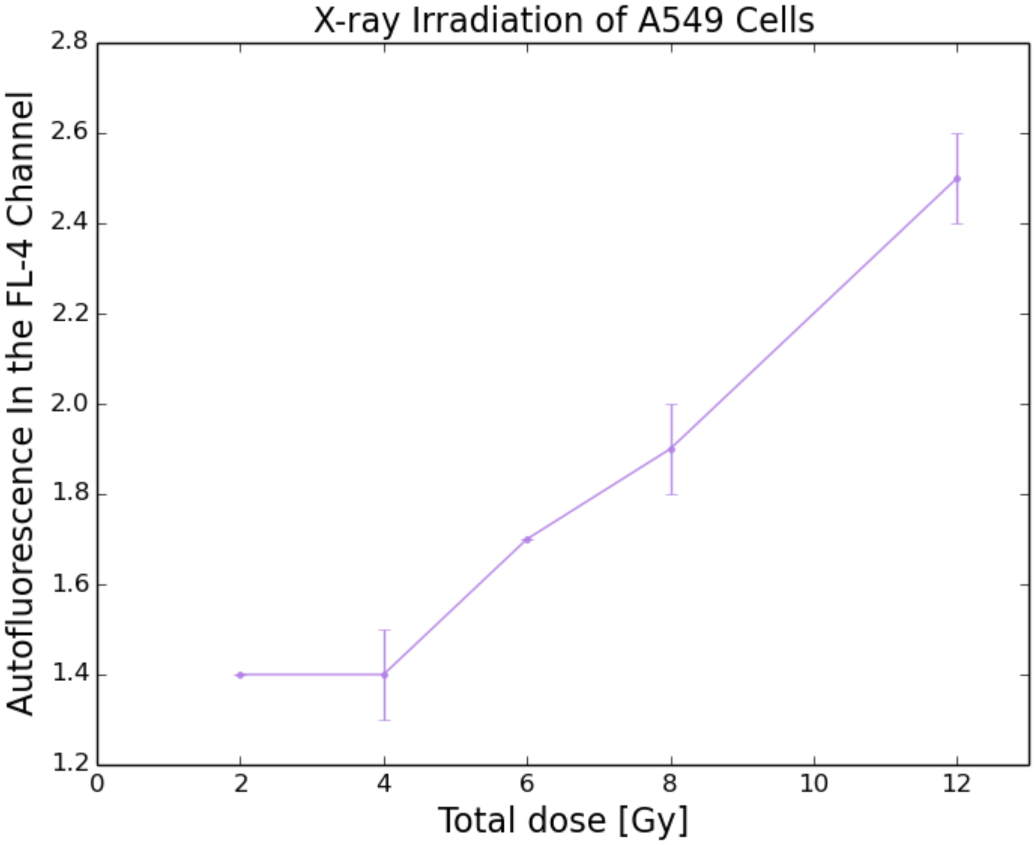

Figure 38: Autofluorescence measured in the FL-4 channel of the flow cytometer as a function of dose. Only one fraction of X-ray irradiation was given. The raw data can be found in Appendix 8.

With regards to the calreticulin assay, the goal is to investigate if there is an increase in the membrane bound calreticulin after ionizing irradiation. In Thingstad's master thesis, several tests were performed to eliminate factors which contributed to unreliable results of the irradiated cells measured calreticulin signal. Investigation of the autofluorescence of the cell line was one (Thingstad, 2019). It was discovered that there was an increase in the measured fluorescence after irradiation also in samples without any antibodies added. This effect appeared to be less pronounced for the wavelength detected in the detection channel of the flow cytometer called FL-4. To minimize the level of autofluorescence in the experiments performed during the work of this thesis, the fluorophore to be used with the calreticulin antibody was therefore changed to one emitting light detected in the FL-4 channel of the flow cytometer. This also implied changing the dye used for barcoding the controls (see section 3.6.1) from one detected in channel FL-4 to one detected in channel FL-1 in the flow cytometer.

However, despite the changes made in the protocol, autofluorescence will still occur, as seen in Figure 38 where the autofluorescence has been plotted as a function of dose. The autofluorescence was calculated by dividing the level of autofluorescence of the irradiated cells with the level of autofluorescence of the control cells (neither receiving primary or secondary antibody), using equation 15. The raw data can be found in Appendix 8.

4.2.2 Developing New Assay Protocol

Several tests with the new dye for barcoding were conducted to see if it was possible to separate the control cells from the irradiated cells. One test was to see if the use of both primary and secondary antibodies could impact the DyLight used in the assay, seen in the left panel in Figure 39. In the right panel, no antibody has been added. The use of antibodies did not impact our results.

Since we are working with non-fixated cells (i.e., cells with an intact membrane), one theory as to why the assay did not work was that the DyLight used could not penetrate the cell membrane and hence, could not stain the control cells. This would mean that the DyLight used in the assay was not functional. Another hypothesis as to why the assay did not work was that the signals in Figure 40 could be from one cell population. It could not be established if the signal to the right in Figure 40 originates from a background signal or the control cells population. However, it appears to be two individual signals, the left signal originating from the irradiated cells and the right signal originating from the control cells. To verify if this was the case, the volume of barcoded cells was changed, seen in Figure 40. A higher volume of barcoded cells should result in a change of signal in the right population of Figure 40. In Figure 40, it is possible to see that a higher volume of barcoded cells added to the cell suspension results in a change in the population to the right in Figure 40. Hence, what was found in Figure 40 was that there is a signal from two different populations (the irradiated cells and the control cells). However, the two signals are too close together in Figure 40, making it difficult to separate the two populations. That further implied that the concentration of the DyLight used to stain the control cells must also be increased. Time was spent testing different concentrations of the DyLight (Figure 41). A complete overview of the different concentrations can be found in Appendix 4. When increasing the concentration of DyLight from 0.25 µg/100 µl medium to 1.42 µg/100 µl medium (almost six times the concentration we first started with), it was possible to distinguish the control cells from the irradiated cells.

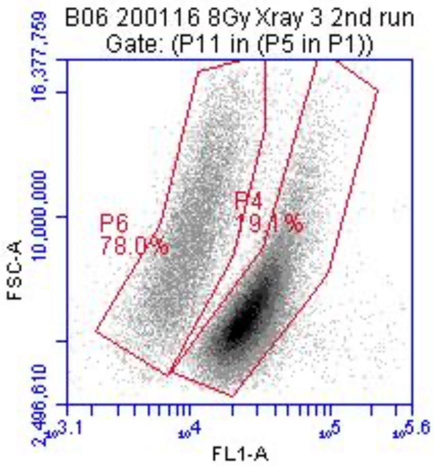

Figure 39: A concentration of 0.25 μg DyLight/ 100 μl medium was used when testing to see if adding antibodies could impact the separation between the two populations. Left panel: both primary and secondary antibody has been added to the cell suspension. Right panel: the cell suspension without primary or secondary antibody added.

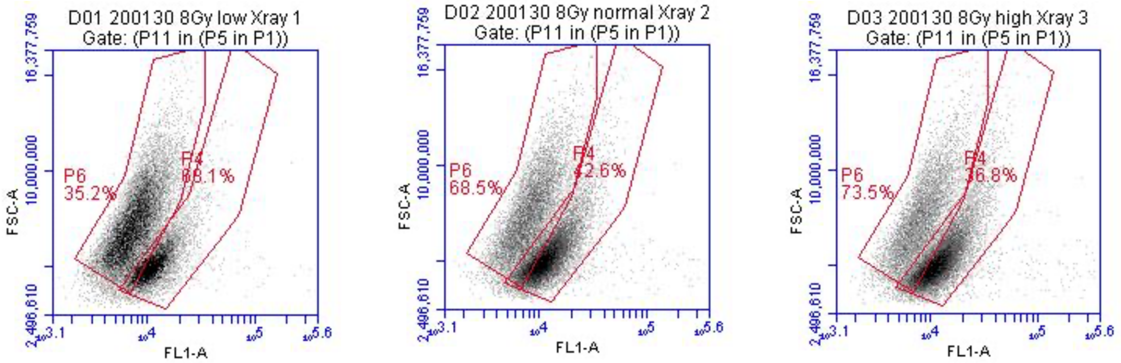

Figure 40: A concentration of 0.25 μg DyLight/ 100 μl medium was used when testing different volumes of barcoded cells added to the cell suspension. This was to see if an increase in the volume of barcoded cells would result in a change of the signal in the right panel (the control cells). In the left panel, 25 μl of barcoded cells were added to the cell suspension. In the middle panel, 100 μl of barcoded cells were added. In the right panel, 150 μl barcoded cells were added to the cell suspension. Increasing the volume of barcoded cells results in a change in the control cell signal (the population to the right).

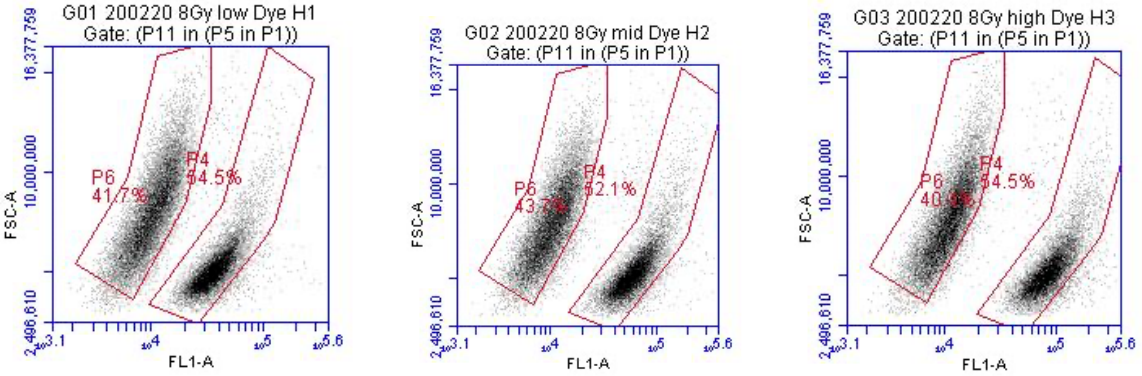

Figure 41: The panels show when different concentrations of DyLight was used to see if this could improve the separation between the control cells and the irradiated cells. Left panel, a concentration of 1.42 µl DyLight/100 µl medium has been used. Middle panel, a concentration of 4.25 µl DyLight/100 µl medium. Right panel, a concentration of 7.04 µl DyLight/100 µl medium.

4.2.3 Settings of the Gating in the Flow Cytometer Program

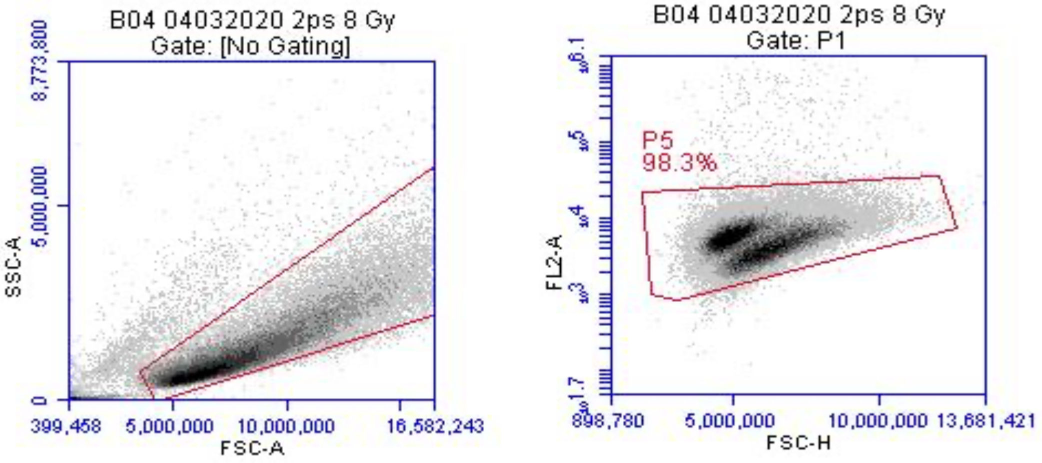

Figure 42: Left panel: the amount of forward scattered cells plotted against the amount of sideward scattered cells. This gating makes it possible to distinguish between live and dead cells. Right panel: gating which only includes the cells with a low uptake of PI, i.e., cells with an intact cell membrane.

In the left panel in Figure 42, a plot of the forward scattered cells (FSC) against the sideward scattered cells (SSC) can be seen. FSC gives the size of the cells, and SSC gives the granularity of the cells. A cell with a broken cell membrane will have a higher SSC value with the same FSC-A value (where A stands for area). By applying the gating seen in the left panel of Figure 42, we are able to include only the whole cells in our analysis.

In the analysis, only living cells, i.e., cells with an intact membrane, should be included. Right before running the flow cytometry analysis, 0.5 µl PI was added to the final cell suspension. The gating applied in the right panel of Figure 42 shows how to gate to include cells with a low uptake of PI only, as cells with a higher uptake of PI indicates a broken membrane (i.e., a dead cell).

Since cell duplets (or triplets) would compromise the counting by having a higher fluorescence signal per unit compared to the single cells, single cells were gated in a plot showing forward scatter signal height against area (Figure 43, left panel) to be included in the further analysis. The barcode signal was used to gate the control cells (high signal, marked in P6) from the irradiated cells (marked in P4) as seen in Figure 43 (right panel).

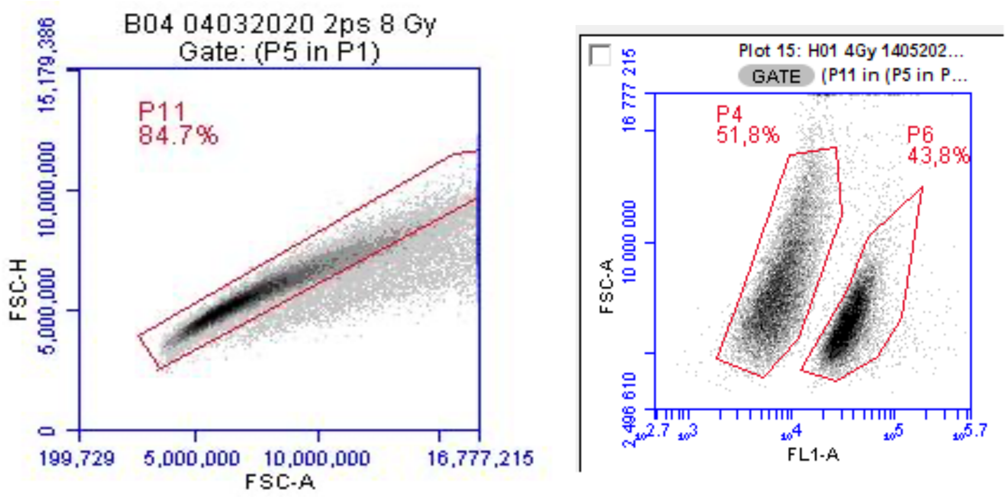

Figure 43: Left panel: gating applied when we only want to include single cells. Right panel: the gating distinguishes between irradiated and control cells. The barcoded signal is marked in P6 (right), while the irradiated signal is marked as P4 (left).

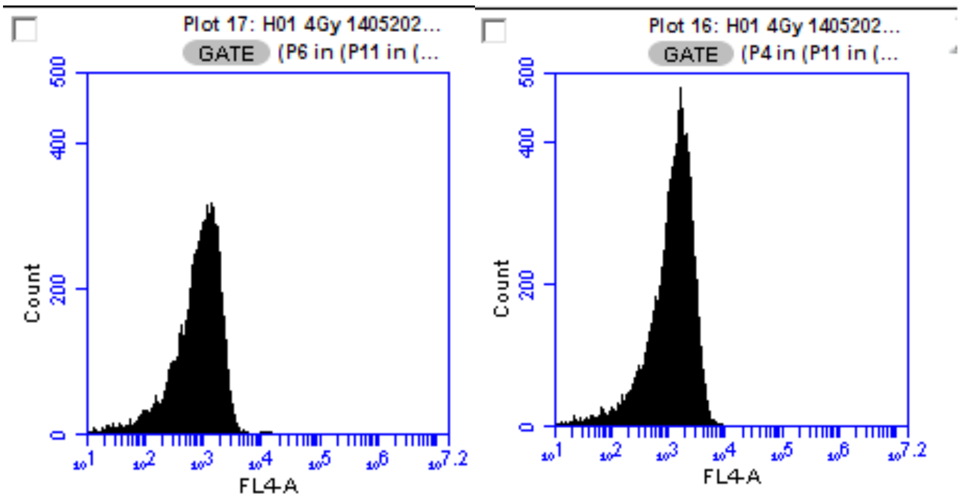

Figure 44: The X-axis shows the signal detected in the FL-4 channel of the flow cytometer, which is the fluorescence signal from the secondary antibody. In the left panel, the control cells are gated. In the right panel, the irradiated cells are gated. Note that what is of interest is the median value of the signals.

Figure 44 shows the control cells (left panel) and the irradiated cells (right panel), and their signal in the FL-4 channel of the flow cytometer. This signal is the fluorescence signal of the secondary antibody bound to the cell membrane bound calreticulin. What is of interest is the median value in the FL-4 channel.

4.3 Calreticulin Results: X-rays

4.3.1 Calculating the Membrane Bound Calreticulin After X-ray Irradiation

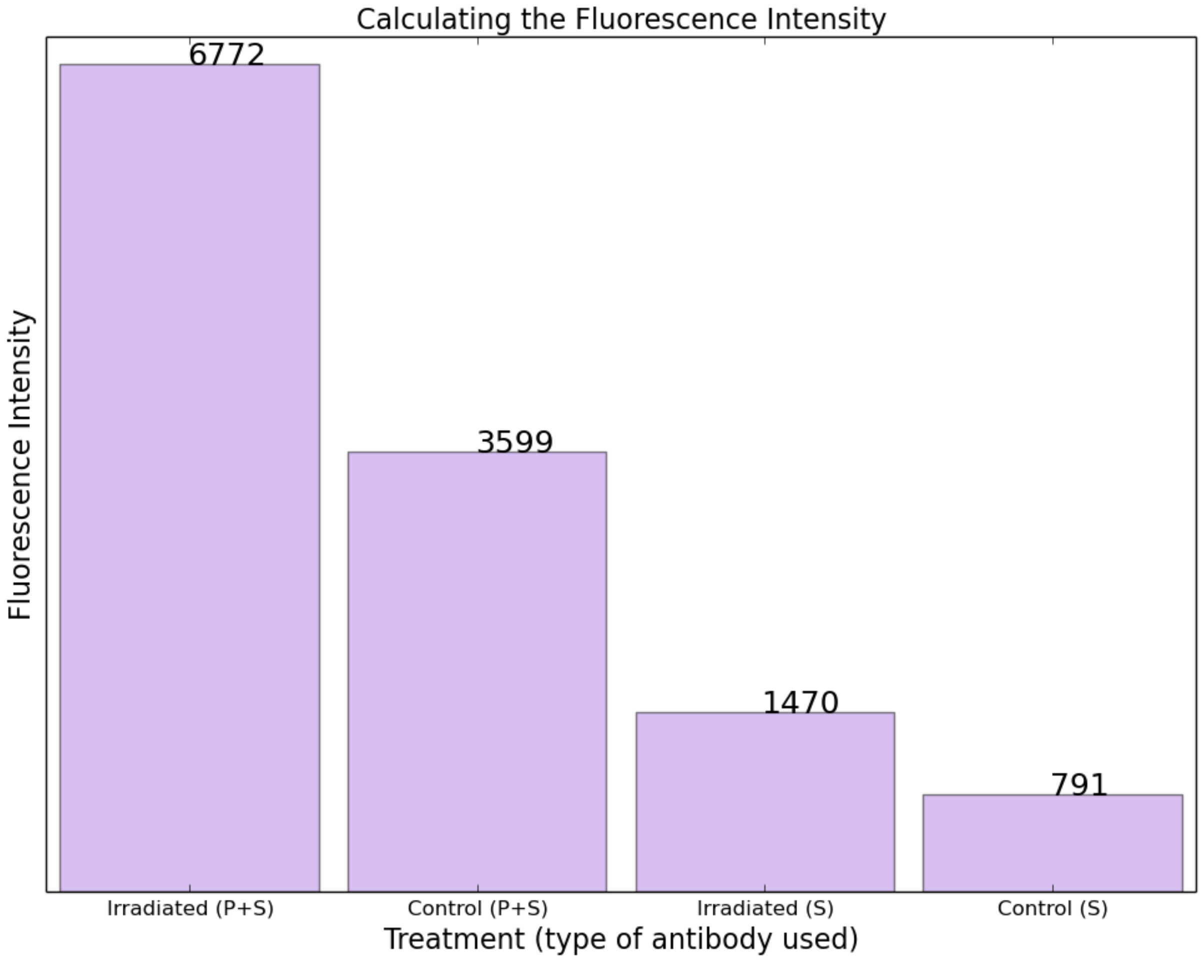

Figure 45: An example of the relative fluorescence of the irradiated cells and the control cells. To calculate the membrane bound calreticulin signal, the calreticulin expression as median fluorescence is found and corrected for unspecific binding and autofluorescence and normalized to control cells. The control cells were not irradiated, while the irradiated cells received 12 Gy as one fraction. P stands for primary antibody added, while S stands for secondary antibody added. See the text for further details on how to calculate the membrane bound calreticulin signal.

In Figure 45, the fluorescence intensity for irradiated cells (recieving 12 Gy as one fraction) given primary and secondary antibody compared to the fluorescence intensity for control cells given primary and secondary antibodies (6772 versus 3599) can be seen. Also, the fluorescence intensity for irradiated cells receiving only secondary antibody compared to the fluorescence intensity for control cells given only secondary antibody (1470 versus 791) can be seen. For estimating the calreticulin expression, the signal was calculated as the median fluorescence corrected for unspecific binding and autofluorescence, further normalized to that in control cells where no antibody has been added and no irradiation were given (using equation 15). For the data in Figure 45, it would result in fluorescence intensity of 1.89 for one experiment when running the calreticulin assay. This method makes it possible to measure the membrane bound calreticulin more precisely by excluding fluorescence signals not originating from the calreticulin bound antibodies.

4.3.2 Membrane Bound Calreticulin After X-ray Irradiation

See Appendix 1 for the raw data from all calreticulin experiments. In addition to what is presented here, two experiments with the T98G cells were conducted giving 8 Gy X-ray irradiation as one fraction. No increase in the calreticulin expression could be seen for the T98G cells.

Note that when the protocol was up and running, several individual experiments were performed at the same date due to practical reasons (such as restricted access to the lab during the corona outburst making it most practical to conduct several experiments each day to limit the number of people at the lab at the same time). The experiments repeated on the same date can be regarded as two independent experiments.

The calculated values for fluorescence intensity of the membrane bound calreticulin expression in A549 cells after X-ray irradiation as a function of dose are shown in Figure 46, the values with standard error are tabulated in Appendix 9. The dose was given either as one fraction (purple graph) and two fractions (black graph). There appears to be a region at the lower doses (2 – 6 Gy), with a slight dose dependent increase in the calreticulin expression when increasing the dose from 2 Gy to 6 Gy. When increasing the dose from 6 Gy to 8 Gy, a strong increase in the calreticulin signal is seen. Further increasing the dose from 8 Gy to 12 Gy results in a slight decrease in calreticulin expression. When the dose is split into two fractions, a similar trend is seen. However, the calreticulin signal for a certain dose appears to be higher compared to the same total dose given in one fraction, and the steep increase takes place when increasing the dose from 8 to 12 Gy with a decrease from 12 Gy to 16 Gy. The data indicates a threshold dose for the maximal effect followed by saturation or even decreased response.

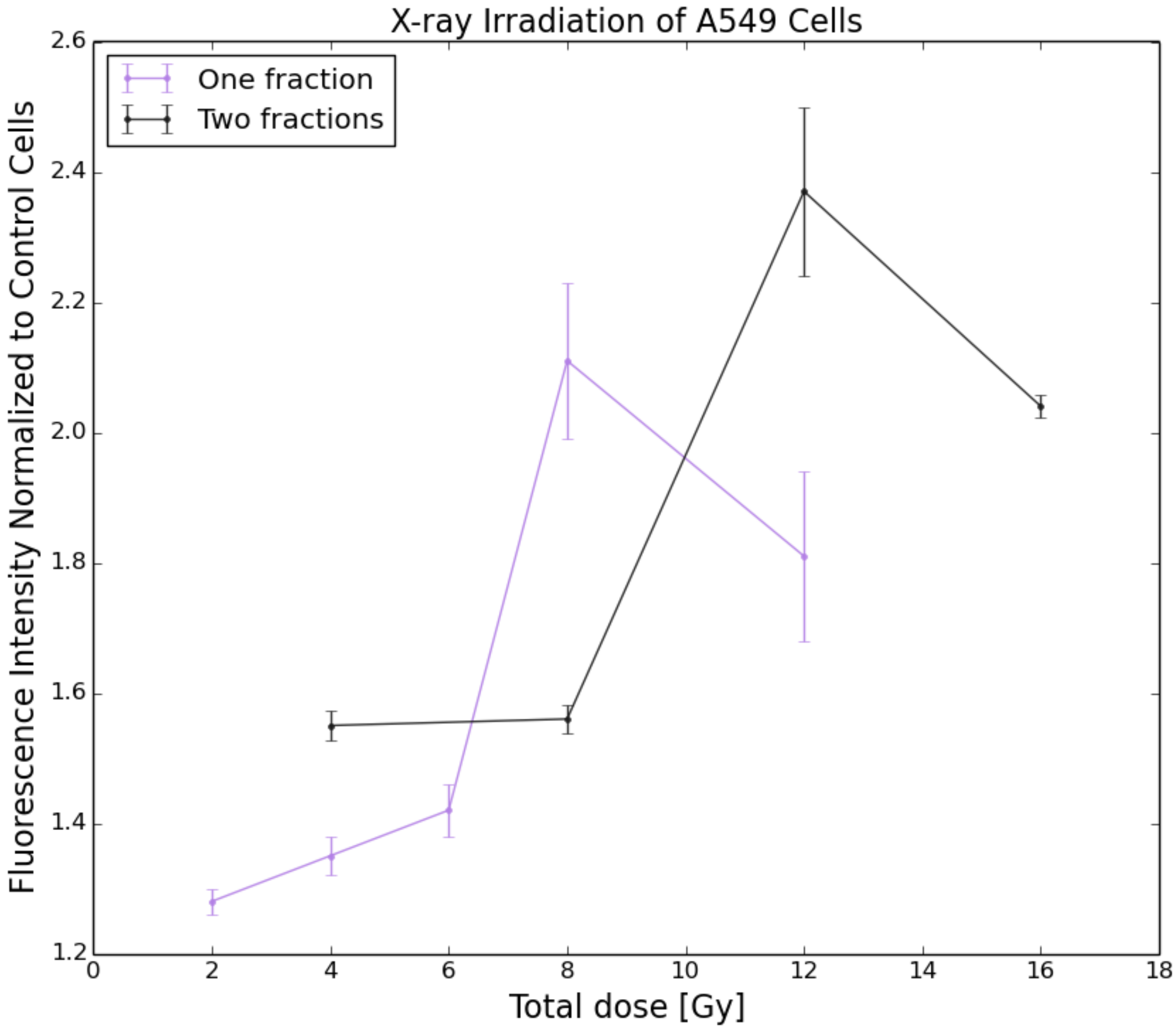

Figure 46: The calreticulin expression in A549 cells 48 hours after X-ray irradiation. The fluorescence intensity was found as median fluorescence corrected for unspecific binding and autofluorescence, normalized to control cells. The control cells were not irradiated. The black graph shows the relative fluorescence intensity when the dose was given in two fractions with 24 hours between each irradiation. The purple graph shows the data for the dose given in one fraction.

4.3.3 Statistical Analysis Results: The Mann-Whitney U Test

Using graphs to display the calreticulin results can be useful in direct comparison between samples. However, the Mann-Whitney U test provides a tool to unmask underlying patterns and dependencies, which can be hard to discover by only looking at Figure 46. In Table 8, p-values comparing calreticulin signals at different radiation exposures are listed. The test used a significance level of $\alpha = 0.05$. In total, 26 comparison gave a significant difference, while ten did not. Looking at Table 8, comparing 12 Gy, one fraction, to giving 6 Gy as two fractions, a splitting of the dose will give a higher membrane bound calreticulin expression, even when the total dose is the same.

Table 8: The p-values for comparing calreticulin signals after X-ray irradiation at different doses and fractions. Significant differences are marked in bold. White and underlined text in a given cell is when the row value is significantly higher than the corresponding column value. Black bold shows the opposite.

	2 Gy	**4 Gy**	**6 Gy**	**8 Gy**	**12 Gy**	**2+2 Gy**	**4+4 Gy**	**6+6 Gy**	**8+8 Gy**
2 Gy	-								
4 Gy	0.218	-							
6 Gy	**0.046**	0.280	-						
8 Gy	**0.005**	**0.001**	**0.005**	-					
12 Gy	**0.005**	**0.006**	**0.031**	0.230	-				
2+2 Gy	**0.005**	**0.001**	**0.031**	**0.005**	0.379	-			
4+4 Gy	**0.005**	**0.001**	**0.020**	**0.005**	0.379	0.936	-		
6 + 6 Gy	**0.005**	**0.001**	**0.005**	0.230	**0.020**	**0.005**	**0.005**	-	
8 + 8 Gy	**0.005**	**0.001**	**0.005**	0.936	0.298	**0.005**	**0.005**	0.066	-

5 Discussion

5.1 Measurements of Micronuclei

The purpose of the cytokinesis-block micronucleus (CBMN) assay was to measure micronuclei formation in A549 cells after being exposed to ionizing radiation. This is of interest since it can be used as a possible marker for an immunogenic response. The cGAS sensing of the micronuclei can trigger gene activation, which may lead to autoinflammatory or antitumor immunity (Gekara, 2017). This had not been done in our group before, and protocol development was therefore needed. The dose was 8 Gy X-rays given as one fraction. Due to time constraints, no experimental data after X-ray irradiation has been retrieved.

5.1.1 CBMN Protocol Development

The cytokinesis-block micronucleus assay (CBMN) is one of the most popular versions of micronucleus assays to measure the frequency of micronuclei after ionizing radiation to be used (Sommer et al., 2020). In the protocol developed during this thesis, cytochalasin-B (Cyt-B) has been added as a step in the protocol. Cyt-b is an inhibitor of the spindle assembly, and it prevents the cytoplasmic division after the nuclear division has occurred (Sommer et al., 2020).

Previous work has been done to visualize the micronuclei, where the cell nuclei and micronuclei were stained with propidium iodide (PI) (Luzhna et al., 2013). When PI is used to stain the nuclei, both the DNA and the ribonucleic acid (RNA) are stained. Our goal is to count only the DNA, so ribonuclease (RNase) should then be added as well to remove the RNA, as was done in the left panel of Figure 31. However, when testing PI and RNase as the staining, it was impossible to detect the cell or the cell nuclei in the confocal microscope. Note that adding RNase should not impact the staining of the micronuclei, and the results obtained could be random, as few images were taken of the cells when RNase was added. Instead of RNase, NucSpot 650 (NucSpot) was tested, as well as CellBrite 488 (CellBrite). NucSpot, without the use of RNase, made it possible to detect the cell nucleus and micronuclei in the confocal microscope. In the end, using only NucSpot and CellBrite as the staining made it possible to detect the cell nuclei, micronuclei, and membrane, respectively. Hence, there is no need to add an extra step using RNase.

To adhere the cells to the coverslip, VectaShield Mounting Medium (VectaShield) was used. It is an oil and has the appropriate refractive index. However, when using the confocal microscope to analyze the micronuclei formation, one problem occurred over and over. When too much was applied or if the VectaShield was left on for too long, the cells were not fixated on the glass and started to move when performing the analysis. If the cells move around when obtaining the images in the confocal microscope, the analysis of the micronuclei would be compromised. This could disturb the number of micronuclei counted, or it could make the images obtained unusable as the cells could move out of the image field. The movement of the cells disrupted some of our experiments, but a finalized CBMN protocol was established. However, the possible challenges of using VectaShield should be kept in mind when running the CBMN as it could potentially ruin the whole experiment.

When establishing the settings for the confocal microscopy, it was essential to keep those settings for all experiments so that the analysis of the microscope slides could be compared for different experiments. To avoid unnecessary light exposure to the sample, the intensity of the laser was kept as low as possible. However, the staining of the samples is not identical for each experiment, so for each experiment, the setting of the laser had to be adjusted to fit the staining of the cells. Some experiments required a higher laser intensity than others to be able to image the cells in the confocal microscope. By including a control sample for each experiment, it was possible to establish a baseline for each individual experiment, making it possible to compare different experiments. After several rounds of experiments, the settings which gave the best results were obtained, and the settings in the ongoing experiments were kept as close to the ones in Table 6.

To be able to reconstruct the cell in 3D after confocal microscopy analysis, it is important to take images in several planes. To obtain micronuclei surrounding the cell, the cell was measured in the confocal microscope by seeing where the cell began and where the cell ended. Each cell was approximately 28 – 35 µm, and the distance between each image was kept at approximately 3 µm. For each cell, approximately 7 – 10 images were taken, which will give a more realistic number of micronuclei compared to only analyzing one image in one plane. Note that the more images obtained, the better visualization of the cell. However, obtaining more than ten images for each cell is highly time consuming.

No developed assay where confocal microscope is used to analyze the formation of micronuclei and a data program automatically counting the micronuclei formation has been found, so one could say that our protocol development is pioneering. However, this is an in vitro method, and Nomani et al. point out that one of the main disadvantages of using this technique (other than being time consuming and labor-intensive) is that the results are only semi-quantitative, which also is the case for our intended protocol (Nomani et al., 2018). Using a microscope to accurately detect and count the number of micronuclei in each picture will produce subjective results, and the outcome is usually associated with high degrees of variability and uncertainty. Several factors could contribute to this. The staining of the micronuclei could be weak, or the confocal microscope image could be of low quality, making it difficult to observe the micronuclei.

Also, Nomani et al. highlight another shortcoming of the microscopy-based micronuclei assay, which is its inability to distinguish micronuclei from aggregated particles (Nomani et al., 2018). This is also the case when counting the micronuclei using the CBMN assay developed during the work of this thesis, either manually or by further developing the data program and using this. However, a data program could potentially be more objective when it comes to distinguishing micronuclei from aggregated particles, based on the threshold set. If one is to persist with this assay, the data program discussed under section 3.5.1 should be further developed to minimize the inability to distinguish micronuclei from noise.

To summarize, a final protocol where appropriate staining of the cell nucleus and micronuclei using NucSpot 650 and CellBrite 488 to stain the cell membrane has been developed. The protocol can be found in Appendix 2. The CBMN assay can be used to analyze the formation of micronuclei after ionizing radiation. To accurately count the number of micronuclei, further development of the software program written by Dr. Stefan Schrunner should be done.

5.2 CBMN Assay: Future Perspectives and Recommendations

With regards to the CBMN assay, future perspectives and recommendations is to further develop the program written by Dr. Stefan Schrunner. This includes setting a threshold for the program to mask out what is noise and what is micronuclei to minimize the shortcomings mentioned above. The data program should be evaluated by taking a set of images, adjusting the image contrast and brightness using, e.g. Photoshop, and manually count the micronuclei. It is then possible to compare this data to the data generated by the data program which automatically counts the micronuclei and set a threshold. One must also decide a physical threshold for the size of the micronuclei, which can be done by analyzing a set of images generated by the data program and set a lower and higher threshold of what is the physical size and shape of the micronuclei.

Experiments including different doses should also be obtained as some studies demonstrate that irradiation of lymphocytes in vitro caused a linear relationship between the dose and micronucleus induction (Luzhna et al., 2013). The same study also states that the frequency of micronuclei was much lower when the fractionated dose of X-rays was applied (Luzhna et al., 2013). Further studies verifying these results should be done. Also, previous studies have investigated the lowest dose of ionizing radiation that is detectable in the CBMN assay to induce micronuclei formation. It was found to be in the range of 0.2 Gy – 0.3 Gy. Another study found that 1 Gy was a more practical threshold (Tucker et al., 2013). In our experiments, a dose of 8 Gy was given to the cells to develop the CBMN assay. Based on the findings by Tucker et al., the lower doses should also be further investigated. One could start at 0.5 Gy and see if micronuclei can be observed using the CBMN protocol developed in this thesis.

It would also be interesting to see if high LET irradiation (such as proton irradiation) will induce a higher number of micronuclei per dose unit compared to low LET irradiation. Studies on particle radiotherapy such as protons are relatively sparse, but in 2014, Miszczyk et al. used the CBMN assay to characterize the response in human peripheral blood lymphocytes obtained from health donors irradiated in vitro in the dose range 0 – 4 Gy to therapeutic proton radiation of 60 MeV from AIC-144 isochronous cyclotron (Miszczyk et al., 2015). They studied the nuclear division index and DNA damage and compared them with X-rays. Miszczyk et al. found, among others, that protons are more effective in producing micronuclei at doses above 1.75 Gy compared to X-rays (Miszczyk et al., 2015). Experiments using both X-ray and proton irradiation should therefore be conducted and compare the formation of micronuclei.

Next, analyzing the number of micronuclei after ionizing irradiation could be obtained at different time points, e.g., 12, 24, 28, and 72 hours. This includes both high LET irradiation and low LET irradiation. One could analyze another cell line and compare the results to the A549 cells. T98G cells are available at the department of biological and medical physics and could be a good place to start.

Also, if the analysis of the formation of micronuclei is to be investigated even further, one could for example look at the size of the micronuclei (e.g., the volume) and the placement of the micronuclei in the cell after ionizing radiation. However, it appears that the break in the chromosome is random, and therefore the size of the micronuclei seems to be random as well.

No studies at this point seem to have investigated this, so it could possibly be something to explore further.

The protocol developed in this thesis is, as stated above, to be used for analyzing the formation of micronuclei after ionizing radiation. The CBMN assay could potentially be used for other purposes as well, one being as a marker to predict cancer. In 2008, El-Zein et al. reported that the CBMN assay is extremely sensitive to genetic damage caused by the tobacco-specific nitrosamine 4-(methylnitrosamino)-1-(3-pyr-idyl)-1-butanone (NNK) (a strong pulmonary carcinogen and a potent inducer of lung adenocarcinoma) and that the binucleated cells with micronuclei, nucleoplasmic bridges, and nuclear buds in lymphocytes are strong predictors of lung cancer risk (El-Zein et al., 2008), which was later confirmed by another group (McHugh et al., 2013). Thus, the CBMN protocol developed in this thesis could perhaps also be used as a marker of lung cancer, which then will provide a valuable tool for screening and lead to more effective prevention measures.

5.3 Calreticulin Protocol Development

The protein calreticulin was first discovered over 40 years ago and has been implicated in many biological processes. This includes protein folding, modulation of transcriptional pathways, apoptosis, and cancer pathology to name a few (Dudek and Michalak, 2018). More recently however, it has been seen that calreticulin could potentially be used to induce an immune response (Carvalho and Villar, 2018). When cancer cells are exposed to ionizing radiation, one response is the transfer of calreticulin from the endoplasmatic reticulum to the cell surface membrane. Here, calreticulin will act as an "eat me"-signal for phagocytosis of dying cells. This plays an essential role in activating anti-tumor immunity since radiation has the potential to initiate adaptive and innate immune responses that can result in systemic antitumorigenic effects inside and outside of the irradiation field (Carvalho and Villar, 2018).

Using radiation to increase the expression of calreticulin and other damage-associated molecular patterns (DAMPs) on the cell surface membrane seems promising with regards to induce immune responses. However, little research investigating the calreticulin dose dependency has been published. Also, no papers which address autofluorescence when using flow cytometry to measure membrane bound calreticulin expression was found. This clearly demonstrates the need for thorough research before it is possible to conclude whether radiation can induce calreticulin translocation and thereby an immune response. The initial purpose of this thesis was therefore to examine whether the cell surface-exposed protein calreticulin in A549 cells could be related to X-ray radiation in terms of dose when autofluorescence was corrected for. However, it became evident early on that further protocol development of the calreticulin assay was needed as it was not possible to separate the irradiated cells from the control cells after the dye had been changed. Time was spent developing the protocol before experiments irradiating the cells with X-rays gathering experimental data could be conducted, which are further discussed below.

5.3.1 Autofluorescence and Non-Specific Antibody Binding

During the work with Emma Thingstad's master thesis, Thingstad found that even when no antibody was added to the cell sample, significant autofluorescence was detected in the FL-1 channel. Thingstad found that the irradiated sample showed a higher fluorescence than both the untreated samples, which caused unreliable results (Thingstad, 2019). To minimize the level of autofluorescence in our experiments, the fluorophore used with the calreticulin antibody was changed to one fluorophore emitting light detected in the FL-4 channel of the flow cytometer instead of the FL-1 channel. This also implied changing the dye used for barcoding of the control cells, and DyLight Alexa Fluor 488 (DyLight) was used to stain the cells. However, changing the channel to the FL-4 did not eliminate the autofluorescence in our results, as seen in Figure 37. An increase in the autofluorescence with an increasing dose can be seen, which indicates a dose dependence of the autofluorescence.

Autofluorescence in cells occurs when live (unfixated) cells are analyzed using a flow cytometer (Mosiman et al., 1997). Autofluorescence has been shown to mostly be caused by riboflavins, flavin enzymes, and nicotinamide adenine dinucleotide (NADH) (Andersson et al., 1998). These molecules, when exposed to light, will excite over a broad range of wavelengths. Our findings in Figure 38 are corroborated by a study showing a dose dependent effect of ionizing radiation on autofluorescence in several human and murine cell types (Schaue et al., 2012). X-rays with varying doses were used, and the analysis of the cells was done using flow cytometry without adding any external markers (i.e., adding fluorophores). A clear dose-dependency was found using doses below 10 Gy. Out of the fourteen cellular lines tested, thirteen showed a striking rise in the autofluorescence. It was shown that the more radiosensitive the cell type (immune cells), the higher the autofluorescence, while more radiation-resistant tumor cells (such as U87 glioma or PC3 prostate cancer cells) showed less autofluorescence responses. Also, the exclusion of dead cells from the flow analysis only marginally had an impact on the magnitude of the autofluorescence increase after ionizing radiation (Schaue et al., 2012).

Trying to explain the increase in the autofluorescence, Schaue et al. investigated the cell metabolites flavin nucleotide cofactor (FAD) and NADH levels of the mouse dendritic cell line. FAD and NADH/NAD homeostasis are linked with mitochondrial function, metabolism changes, calcium flux, and cell death (Schaue et al., 2012). Here, they found that FAD is most likely to respond to 488 nm excitation with emission of green light, which is consistent with the signal we measure in the FL-1 channel of our flow cytometer. NADH is generally considered the major cellular source of autofluorescence but has an excitation/emission maximum of 340 nm/450 nm, which is outside the range covered by our flow cytometer.

To better understand the cellular mechanisms behind the autofluorescence in cells being exposed to ionizing radiation, Schaue et al. compared parental U87 cells and U87Rho(0) cells (the latter lack mitochondria). A direct comparison of U87 and U87Rho(0) did in fact show that the latter has a higher baseline NADH and higher baseline autofluorescence. However, giving a dose of 10 Gy, both parental U87 and U87Rho(0) showed an increase in NADH and autofluorescence, but it was less pronounced in the U87 cell line. They conclude that the dose-dependent rise in autofluorescence is linked to variations in cell metabolism and cell morphology. In summary, their observation shows a rise in autofluorescence in the cell lines investigated, however, they also state that the proposed underlying mechanisms for radiation induced increase in cellular autofluorescence is highly speculative at this point (Schaue et al., 2012).

A secondary antibody can bind non-specifically, also referred to as undesirable antibody binding, which can also give an increase in the fluorescence measurement that does not originate from the primary antibody binding (Hulspas et al., 2009). To minimize artifacts when using live cells, one should avoid using fluorochrome conjugated primary antibodies. The experimental protocol should always include a sample given only secondary antibody to correct for unspecific binding of secondary antibody as well as autofluorescence. Note that non-specific binding is usually the main concern in assays where antibodies are used, but specific bindings could also be problematic as various studies have indicated that an epitope can be shared by different antigens, which lead to specific antibody binding, which is undesirable (Hulspas et al., 2009).

5.3.2 Developing New Assay Protocol

The first change in the protocol received from Emma Thingstad was to change the fluorophore used with the calreticulin antibody to one emitting light detected in the FL-4 channel of the flow cytometer instead of the FL-1 channel to minimize the autofluorescence. This also implied changing the DyLight used to stain the control cells, from DyLight Alexa Fluor 650 to DyLight Alexa Fluor 488 (DyLight). However, it was not possible to separate the two populations in the flow cytometer analysis (seen in Figure 39) as there was too much overlap between the control cells and the irradiated cells. It was not clear as to why this problem occurred, if it was due to lack of staining of the control cells, if the DyLight was not working, or something else. Several tests were then run to improve the protocol.

Another hypothesis as to why the assay did not work was that since we are working with unfixated cells (i.e., cells with an intact membrane), the DyLight might not be able to penetrate the cell membrane, hence not be able to stain the cells. In the left panel of Figure 40, it is not easy to see if the signals originate from the stained cells or if it is a background signal. To test if we could see signals from both the irradiated cells and the control cells, the volume of barcoded cells added to the cell suspension was changed. If we then could detect a change in the cell population to the right in Figure 40, it would mean that we had signals from both cell populations. When increasing the volume of barcoded cells, a change in signal was found, as seen in the middle and right panel of Figure 40. However, the two signals are too close together, making it difficult to separate the two populations from one another. That further implied that the concentration of the DyLight used to stain the control cells must also be increased. In the end, it was discovered that the molar extinction coefficient was much lower for DyLight Alexa Fluor 488 than for DyLight Alexa Fluor 650. DyLight Alexa Fluor 650 therefore requires a lower concentration than the DyLight to be able to separate the control cells from the irradiated cells. When increasing the concentration of the DyLight almost six times, from 0.25 µg/100 µl medium to 1.42 µg/100 µl medium, a clear separation could be seen for the control cells and the irradiated cells (Figure 41). Here, it is also possible to see that the higher the concentration of DyLight used, the further the two populations are from one another, the easier it is to separate the two populations. For practical reasons, the recommended concentration of DyLight was set to 1.42 µg/100 µl medium, even though 7.04 µg/100 µl medium gives an even further separation between the irradiated cells and the control cells.

5.3.3 Settings of the Gating

When it comes to applying the gating in the flow analysis program, what is essential is to gate out cells that are not of interest. This means that dead cells must be excluded, and only barcoded and irradiated cells must be included. The preferred gating to achieve this can be seen in section 4.2.3. Note that these applied gating's are subjective and based on the preferred way to exclude cells which are not of interest. It could be beneficial to gate otherwise in some cases. However, the gating's in section 4.2.3 are applied to all the data gathered during the work of this thesis in order to be able to compare the data.

5.4 Calreticulin Results: X-Rays

It has been well known for many years that ionizing radiation has not only local action but also systemic effects by triggering many molecular signaling pathways (Carvalho and Villar, 2018). Accumulating evidence in recent years supports the role of ionizing radiation as an inducer of antitumor immunity. Sublethal doses of proton or photon irradiation has been shown to induce an increase in translocation of calreticulin to the tumor cell surface, indicating immunogenic cell death and stimulation of immune response (Carvalho and Villar, 2018). Thus, ionizing radiation can affect the generation of immune responses that are important for systemic control (Ko et al., 2018). Several radiation dose and fractionations schema have been tested during the years, both in a preclinical setting and in a clinical setting.

In this thesis, two cell lines were used. However, the two experiments conducted with T98G cells showed no apparent increase in the membrane bound calreticulin after 8 Gy X-ray irradiation. These cells were therefore not used in further experiments.

Figure 46 shows the experimental data for A549 cells measuring cell surface calreticulin using the FL-4 channel of the flow cytometer after X-ray irradiation. There is a slight increase in the level of calreticulin fluorescence as the dose is increased from 2 Gy to 6 Gy, with a sharp increase when increasing the dose from 6 to 8 Gy. A similar trend is seen for the split dose experiments with a sharp increase in calreticulin signal when the total dose is increased from 8 Gy to 12 Gy. However, when increasing the dose from 8 Gy to 12 Gy, and from 12 Gy to 16 Gy when the dose is given in two fractions, a (not significant) decrease in the membrane bound calreticulin can be observed in our experiments.

This is in line with a previous study that also found a threshold dose per fraction were further increasing the dose did not lead to a higher immune response in the cancer cells (Ko et al., 2018). There appears to be a window of radiation dosing that is more effective in supporting the tumor immunity.

The decrease in the fluorescence signal could either reflect saturation of the fluorescence signal or an actual decrease in the calreticulin translocation to the cell membrane at this threshold dose. One can speculate that the latter could be due to other forms of cell death that are not immunogenic taking over when the dose is increased above this threshold dose.

However, it is possible that our experiments have been conducted at the wrong time points and that the maximum fluorescence signal has not been reached for the highest doses. During the work of this thesis, there were consistently 48 hours between the last dose given, and when the assay has been run. One could speculate that the maximum calreticulin expression after ionizing radiation depends on the dose and is at another time point than 48 hours for the highest doses. Perhaps running the calreticulin assay 36 or 72 hours after X-ray irradiation would give an increase in the membrane bound calreticulin expression for 12 Gy and two fractions of 8 Gy (total dose of 16 Gy).

Another interesting finding from Figure 46, is that there is a more considerable difference in fluorescence between the irradiated sample compared to the control samples when the dose is given in two fractions. Thus, splitting the dose into two fractions appears to increase the membrane bound calreticulin expression in the cancer cells. A speculation could be that some cellular processes will be initiated after the first dose has been given, which influences the translocation of calreticulin. An explanation could be that the cells which start to express the calreticulin on the cell surface send out other signals to the surrounding cells. Then, by following up with the second dose after 24 hours, one could speculate that this would lead to increased calreticulin translocation or perhaps inhibition of the mechanisms that led to the decrease seen for doses above 8 Gy for single doses.

Another impact of giving a fractionated dose is that the cells will receive a lower dose in each fraction. This should implicate less damage to the cell and time for repair of damage before the next dose. Hence, one would expect less immunogenic cell death and less calreticulin expression on the cell surface when splitting the dose. However, as seen in Figure 46, this is not the case. It seems that there must be another reason why the same total dose gives an increase in the membrane bound calreticulin after ionizing radiation when splitting the dose with a time interval of 24 hours between each radiation.

In a study conducted by Rubner et al. using T98G glioblastoma cells, the different types of cell death were analyzed after 2 Gy given as five fractions with a total dose of 10 Gy. This increased the number of both apoptotic and necrotic cells compared to single dose irradiation when analyzed 48 hours after the last dose was given (Rubner et al., 2014). Rubner et al. state that ionizing radiation is known to induce an arrest of tumor cells in the G_2 phase of the cell cycle, a phase which leaves the cells highly susceptible to further irradiation. In their study, they found that one third of T98G cells were arrested in the G_2 phase of the cell cycle four hours after irradiation was given, which lasted at least 48 hours post irradiation (Rubner et al., 2014). In contrast, when only one fraction of 10 Gy was given, the G_2 arrest of the T98G cells could not be seen when the cells were observed 4 – 72 hours post irradiation (Rubner et al., 2014). Their findings demonstrate the clinical relevance of the effect of using a fractionated regime when using radiotherapy to treat cancer.

To a certain extent, this could support the results obtained in this thesis and perhaps explain why we see an increase in the membrane bound calreticulin when a fractionated dose regimen is given. Adding a second dose 24 hours after the first dose appears to render the cells in a more radiosensitive phase, the G_2 phase, and this might increase the number of cells which undergo immunogenic cell death. This, in turn, could result in an increase in the membrane bound calreticulin as our data does, in fact, show an increase in the membrane bound calreticulin when splitting the dose.

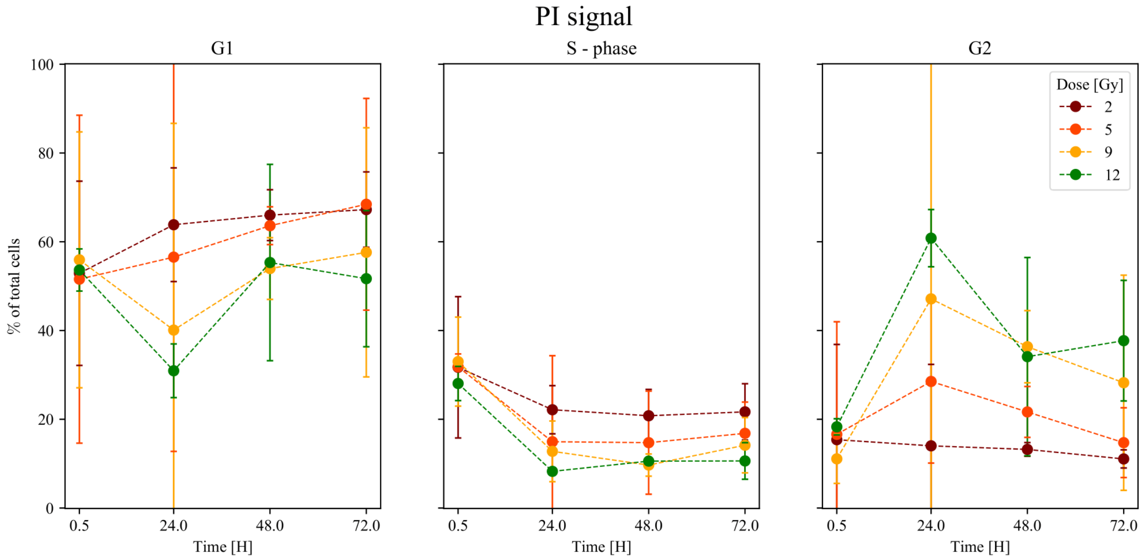

Figure 47: Unpublished data from the work of Hilde Solesvik Skeie's master thesis. The figure shows the percentage of cells in different cell cycle phases as a function of harvest time after irradiation. The percentage of G_1 cells increase from 0.5 h to 24 h for lower doses (2 and 5 Gy) and stabilized after 24 h time point. Higher doses of 9 and 12 Gy decrease the percentage of G_1 cells towards 24 h, before increasing again. G_2 and G_2

arrest are complementary of the G_1 plot in the left panel. High doses (5, 9, and 10 Gy) lead to an increase in the G_2 arrest before declining again after 24 hours. Of interest to this thesis is the arrest after 24 hours.

The study by Rubner et al. is based on data from T98G cells. During the work of her master thesis, Hilde Solesvik Skeie has investigated cell cycle arrest after ionizing radiation for A549 cells. Figure 47 shows her unpublished data, showing the percentage of cells in different cell cycle phases as a function of harvest time after irradiation. After 24 hours, cells which have been given a higher dose (5, 9, and 12 Gy) have a higher percentage of G_2 arrest compared to cells given a lower dose (2 Gy), which are mainly arrested in the G_1 phase of the cell cycle.

As previously mentioned, cells are most sensitive during the G_2/M phase of the cell cycle and most resistant to radiation during the late S phase and G_1 phase. Thus, cells irradiated while in the G2 state may be expected to have a higher induction of cell death. It can be speculated that the immunogenic cell death process only occurs until a certain threshold of damage is reached, but that this damage threshold is higher when the dose is fractionated. When the dose exceeds this threshold, other death processes take over.

There are not many studies measuring calreticulin translocation after irradiation. In addition, it is important to know if there was a correction for radiation induced autofluorescence before comparing results. An example of a study using a fluorochrome-conjugated calreticulin antibody, which means it cannot be corrected for autofluorescence, is a study using H522 lung cancer cells (Gameiro et al., 2014). Gameiro et al. found that radiation induced secretion of ATP and HMGB1 (two other markers of immunogenic cell death) in both dying and surviving tumor cells, in addition to upregulation of membrane bound calreticulin (Gameiro et al., 2014). Gameiro et al. exposed cells 10 Gy gamma radiation using a ^{137}Cs source and analyzed the cells by flow cytometry 72 hours post treatment. Here, they observed a significant translocation of the endoplasmatic reticulum chaperone calreticulin to the cell surface. In non-irradiated cells, calreticulin membrane staining was 34.7 % +/- 20.4 %, while in tumor cells, the calreticulin membrane staining was 78.8 % +/- 13.1 % (Gameiro et al., 2014). In another study, prostate carcinoma cells exposed to photon irradiation had a 47 % increase in surface and intracellular expression of calreticulin. Here, they used a conjugated calreticulin antibody (Gameiro et al., 2016). Also, Golden et al. identified a dose-dependent increase in the ATP release, cell surface translocation of calreticulin, and HMGP1 release of dying cancer cells using TSA murine mammary carcinoma cells. Here, a single fraction of 2 – 20 Gy of ionizing radiation was given in vitro (Golden et al., 2014). In their article, it is not clear if Golden et al. have corrected for autofluorescence and/or unspecific bindings when measuring the membrane bound calreticulin. However, it appears that they have used the FL-1 channel to measure the fluorescence intensity. As previously discussed, the FL-1 channel has been shown to produce less reliable results. One must therefore assume that at least part of the increase in the signal could be due to autofluorescence and not an actual increase in the membrane bound calreticulin after ionizing radiation.

As seen, the protein calreticulin and its functions are complex and not fully understood. It is even argued that it could possibly be a mistake to consider calreticulin as one protein (Varricchio et al., 2017). One should thus be careful when interpreting the results obtained during the work of this thesis. However, internationally, it is recognized that the assay measuring the membrane bound calreticulin after ionizing radiation is difficult to conduct and that it is hard to reproduce the data obtained (Nina F. J. Edin, personal communication, 2020). One could therefore say that the protocol developed during the work of this thesis, which corrects for unspecific binding and address the autofluorescence, produces more reliable results and data which can be reproduced.

5.5 Calreticulin Assay: Future Perspectives and Recommendations

Although most studies have used X-rays to investigate the immune response in cells after ionizing radiation, there are also examples of studies using particle irradiation. In 2016, Malamas et al. investigated the response in prostate carcinoma cells treated with 10 Gy of ^{223}Ra and found that the surface translocation of calreticulin was increased compared to untreated cells (Malamas et al., 2016). Also, Gameiro et al. found that 8 Gy of proton irradiation increased the cell surface translocation of calreticulin in several carcinoma cell lines, including lung cancer cells, similar to those cells treated with 8 Gy photon irradiation (Gameiro et al., 2016). In their article, Carvalho et al. state that particle beams may be as effective as photon beams (or even more advantageous) in immune combination therapy (Carvalho and Villar, 2018). They state that the same relative biological effectiveness dose induced different biological responses when particles are used (such as protons) compared to photon beams (3 times more efficient). It is therefore interesting to investigate the calreticulin expression after proton radiation and compare the results to X-ray radiation. This was an original objective in this thesis, but because the cyclotron at UiO broke down, it was not possible to do these experiments. They should therefore be prioritized when the cyclotron is functioning again.

Also, only two experiments using the T98G cells have been included in this thesis. No increase in the membrane bound calreticulin could be found, but only one fraction of 8 Gy was given. Based on this, we are not able to state that the T98G cells in general do not show an increase in the membrane bound calreticulin expression after being exposed to X-ray irradiation. Further experiments should therefore be conducted. Both one and two fractions should be given, varying the dose from 2 Gy to 16 Gy and compare them to the data for the A549 cells obtained during the work with this thesis. Including experiments with calreticulin translocation after proton irradiation of the T98G cells could also be interesting, as this has not yet been tested.

The analysis performed during this thesis was consistently done at 48 hours post irradiation. Varying the time points, performing the assay, e.g. 12, 24, and 72 hours after both X-ray and proton irradiation, is recommended to see if this has any implications on the results. Varying the time points could also be done to investigate if there is a threshold per dose where further increasing the dose becomes less effective in supporting the tumor immunity, as stated by Ko et al. (Ko et al., 2018).

Another interesting experiment could be to implement confocal microscopy to analyze the membrane bound calreticulin after both proton and X-ray irradiation. The confocal microscopy analysis is to get a better visual representation of the distribution of the calreticulin. One can then compare the images obtained with the confocal microscopy analysis to the data from the flow cytometry, which perhaps could give a better understanding of the membrane bound calreticulin.

6 Conclusion

This thesis aimed to investigate immune responses in A549 cells (lung cancer cells) in response to ionizing radiation by measuring the micronuclei formation and the membrane bound calreticulin in A549 cells after ionizing radiation.

A protocol for the cytokinesis-block micronucleus (CBMN) assay was established. By using NucSpot 650 to stain the cell nucleus and micronuclei, and CellBrite 488 to stain the cell membrane, it is possible to use the confocal microscope (Leica SP2, Germany) to visualize the cell, the cell nuclei, and the micronuclei. Manually counting the micronuclei formation after ionizing radiation proved to be difficult, not to mention highly time consuming. A program written by Dr. Stefan Schrunner was only tested for a few images, however, preliminary results indicate that this program could potentially be more subjective when it comes to distinguishing micronuclei from aggregated particles. The CBMN counting software that automatically counts the micronuclei after ionizing radiation should be further developed before experimental data is to be retrieved.

A protocol for measuring the membrane bound calreticulin expression after ionizing radiation was established. Autofluorescence will occur when using flow cytometry to analyze the A549 cells after the calreticulin assay because the cells are not fixated. The wavelength for the fluorochrome should be as far as possible from the autofluorescence wavelength. In addition, the autofluorescence must be corrected for when calculating the membrane bound calreticulin expression after ionizing radiation.

A549 cells were found to have an increase in the membrane bound calreticulin in response to X-ray radiation. There seemed to be a slight increase after the lowest doses of 2 – 6 Gy followed by a steep rise for 8 Gy. When increasing the dose further, a slight decrease in calreticulin signal was observed. The same curve shape was obtained when the dose was given in two fractions 24 hours apart. However, the level of calreticulin was higher for the fractionated dose compared to when the same dose was given in one fraction, and the steep increase occurred for 12 Gy.

Our data indicate that the membrane bound calreticulin expression in A549 cells is dose dependent with a threshold dose for induction and another for saturation.

No increase in the membrane bound calreticulin was found for T98G cells following 8 Gy X-ray radiation.

References

abcam. (2020). Introduction to flow cytometry. Retrieved from https://www.abcam.com/protocols/introduction-to-flow-cytometry (07.10.2020)

Adan, A., Alizada, G., Kiraz, Y., Baran, Y., & Nalbant, A. (2017). Flow cytometry: basic principles and applications. *Crit Rev Biotechnol, 37*(2), 163-176. doi:10.3109/07388551.2015.1128876

Alberts, B. (2015). *Molecular biology of the cell* (Sixth edition. ed.). New York, NY: Garland Science, Taylor and Francis Group.

Andersson, H., Baechi, T., Hoechl, M., & Richter, C. (1998). Autofluorescence of living cells. *J Microsc, 191*(Pt 1), 1-7. doi:10.1046/j.1365-2818.1998.00347.x

Attix, F. H. (1986). *Introduction to radiological physics and radiation dosimetry*. New York: John Wiley & Sons

Bai, J., & Liu, F. (2019). The cGAS-cGAMP-STING Pathway: A Molecular Link Between Immunity and Metabolism. *Diabetes, 68*(6), 1099-1108. doi:10.2337/dbi18-0052

Bailey, D. L., Humm, J. L., Todd-Pokropek, A., Van Aswegen, A., International Atomic Energy, A., & American Association of Physicists in, M. (2014). *Nuclear medicine physics : a handbook for teachers and students*.

Biotium. (2015). Cellular Stains. In: Biotium.

Bose, D. (2017). cGAS/STING Pathway in Cancer: Jekyll and Hyde Story of Cancer Immune Response. *Int J Mol Sci, 18*(11). doi:10.3390/ijms18112456

Cai, X., Chiu, Y. H., & Chen, Z. J. (2014). The cGAS-cGAMP-STING pathway of cytosolic DNA sensing and signaling. *Mol Cell, 54*(2), 289-296. doi:10.1016/j.molcel.2014.03.040

Carvalho, H. A., & Villar, R. C. (2018). Radiotherapy and immune response: the systemic effects of a local treatment. *Clinics (Sao Paulo), 73*(suppl 1), e557s. doi:10.6061/clinics/2018/e557s

Chao, M. P., Jaiswal, S., Weissman-Tsukamoto, R., Alizadeh, A. A., Gentles, A. J., Volkmer, J., . . . Weissman, I. L. (2010). Calreticulin is the dominant pro-phagocytic signal on multiple human cancers and is counterbalanced by CD47. *Sci Transl Med, 2*(63), 63ra94. doi:10.1126/scitranslmed.3001375

Cossarizza, A., Chang, H. D., Radbruch, A., Akdis, M., Andrä, I., Annunziato, F., . . . Zimmermann, J. (2017). Guidelines for the use of flow cytometry and cell sorting in immunological studies. *Eur J Immunol, 47*(10), 1584-1797. doi:10.1002/eji.201646632

Das, I. J., & Chopra, K. L. (1995). Backscatter dose perturbation in kilovoltage photon beams at high atomic number interfaces. *Med Phys, 22*(6), 767-773. doi:10.1118/1.597594

Dobosz, P., & Dzieciątkowski, T. (2019). The Intriguing History of Cancer Immunotherapy. *Front Immunol, 10*, 2965. doi:10.3389/fimmu.2019.02965

Doll, R., & Hill, A. B. (1950). Smoking and carcinoma of the lung; preliminary report. *Br Med J, 2*(4682), 739-748. doi:10.1136/bmj.2.4682.739

Dudek, E., & Michalak, M. (2018). Calreticulin. In S. Choi (Ed.), *Encyclopedia of Signaling Molecules* (pp. 682-689). Cham: Springer International Publishing.

El-Zein, R. A., Fenech, M., Lopez, M. S., Spitz, M. R., & Etzel, C. J. (2008). Cytokinesis-blocked micronucleus cytome assay biomarkers identify lung cancer cases amongst smokers. *Cancer Epidemiol Biomarkers Prev, 17*(5), 1111-1119. doi:10.1158/1055-9965.Epi-07-2827

Gameiro, S. R., Jammeh, M. L., Wattenberg, M. M., Tsang, K. Y., Ferrone, S., & Hodge, J. W. (2014). Radiation-induced immunogenic modulation of tumor enhances antigen processing and calreticulin exposure, resulting in enhanced T-cell killing. *Oncotarget, 5*(2), 403-416. doi:10.18632/oncotarget.1719

Gameiro, S. R., Malamas, A. S., Bernstein, M. B., Tsang, K. Y., Vassantachart, A., Sahoo, N., . . . Hodge, J. W. (2016). Tumor Cells Surviving Exposure to Proton or Photon Radiation Share a Common Immunogenic Modulation Signature, Rendering Them More Sensitive to T Cell-Mediated Killing. *Int J Radiat Oncol Biol Phys, 95*(1), 120-130. doi:10.1016/j.ijrobp.2016.02.022

Gekara, N. O. (2017). DNA damage-induced immune response: Micronuclei provide key platform. *J Cell Biol, 216*(10), 2999-3001. doi:10.1083/jcb.201708069

Giard, D. J., Aaronson, S. A., Todaro, G. J., Arnstein, P., Kersey, J. H., Dosik, H., & Parks, W. P. (1973). In Vitro Cultivation of Human Tumors: Establishment of Cell Lines Derived From a Series of Solid Tumors2. *JNCI: Journal of the National Cancer Institute, 51*(5), 1417-1423. doi:10.1093/jnci/51.5.1417

Golden, E. B., Frances, D., Pellicciotta, I., Demaria, S., Helen Barcellos-Hoff, M., & Formenti, S. C. (2014). Radiation fosters dose-dependent and chemotherapy-induced immunogenic cell death. *Oncoimmunology, 3*, e28518. doi:10.4161/onci.28518

Hall, E. J., & Giaccia, A. J. (2019). *Radiobiology for the radiologist* (Eighth edition. ed.). Philadelphia: Wolters Kluwer.

Hanson, I. (2018). Solid Stress and Nanoparticle Microdistribution in Xenografts: Effects of Ultrasound and Microbubble Cavitation.

Harada, K., Takenawa, T., Ferdous, T., Kuramitsu, Y., & Ueyama, Y. (2017). Calreticulin is a novel independent prognostic factor for oral squamous cell carcinoma. *Oncol Lett, 13*(6), 4857-4862. doi:10.3892/ol.2017.6062

Hinton, P. R., McMurray, I., & Brownlow, C. (2014). *SPSS explained, 2nd ed*. New York, NY, US: Routledge/Taylor & Francis Group.

Hooke, R. (1667). *Micrographia, or, Some physiological descriptions of minute bodies made by magnifying glasses : with observations and inquiries thereupon*: London : Printed for James Allestry.

Houghton, A. N., & Guevara-Patiño, J. A. (2004). Immune recognition of self in immunity against cancer. *J Clin Invest, 114*(4), 468-471. doi:10.1172/jci22685

Huang, Y., Dong, Y., Zhao, J., Zhang, L., Kong, L., & Lu, J. J. (2019). Comparison of the effects of photon, proton and carbon-ion radiation on the ecto-calreticulin exposure in various tumor cell lines. *Ann Transl Med, 7*(20), 542. doi:10.21037/atm.2019.09.128

Hulspas, R., O'Gorman, M. R., Wood, B. L., Gratama, J. W., & Sutherland, D. R. (2009). Considerations for the control of background fluorescence in clinical flow cytometry. *Cytometry B Clin Cytom, 76*(6), 355-364. doi:10.1002/cyto.b.20485

International Atomic Energy Agency. (2000). Absorbed dose determination in external beam radiotherapy : an international code of practice for dsimetry based on standards of absorbed dose to water. In *Technical reports series* (pp. 229). Austria: International Atomic Energy Agency.

International Atomic Energy Agency. (2010). Implementation of the International Code of Practice on Dosimetry in Radiotherapy (TRS 398): Review of Testing Results. In. Vienna: International Atomic Energy Agency.

Kielberg, V., Brünner, N., Briand, P. . (2001). *Celledyrkning. En praktisk håndbog i dyrkning af mammalske celler*. København: Gads Forlag.

Kieranmaher. (2001). Retrieved from https://commons.wikimedia.org/wiki/File:XrtSpectrum.jpg (23.09.2020))

Kierano. (2012). Retrieved from https://commons.wikimedia.org/wiki/File:Cytometer.svg (23.09.2020) (23.09.2020))

Kim, S., Palta, Jatinder. (2015). *The Pysics of Stereotactic Radiosurgery* Springer, New York, NY

Ko, E. C., Benjamin, K. T., & Formenti, S. C. (2018). Generating antitumor immunity by targeted radiation therapy: Role of dose and fractionation. *Adv Radiat Oncol, 3*(4), 486-493. doi:10.1016/j.adro.2018.08.021

Kreftregisteret. (03.03.2020). Lungekreft. Retrieved from https://www.kreftregisteret.no/Temasider/kreftformer/Lungekreft/

Krutzik, P. O., Clutter, M. R., Trejo, A., & Nolan, G. P. (2011). Fluorescent cell barcoding for multiplex flow cytometry. *Curr Protoc Cytom, Chapter 6*, Unit 6.31. doi:10.1002/0471142956.cy0631s55

Krysko, D. V., Garg, A. D., Kaczmarek, A., Krysko, O., Agostinis, P., & Vandenabeele, P. (2012). Immunogenic cell death and DAMPs in cancer therapy. *Nat Rev Cancer, 12*(12), 860-875. doi:10.1038/nrc3380

Kubitscheck, U. (2013). *Fluorescence microscopy : from principles to biological applications*. Weinheim: Wiley-Blackwell.

Linz, U. (2012). *Ion Beam Therapy*. Springer-Verlag Berlin Heidelberg.

Liu, Y., Dong, Y., Kong, L., Shi, F., Zhu, H., & Yu, J. (2018). Abscopal effect of radiotherapy combined with immune checkpoint inhibitors. *J Hematol Oncol, 11*(1), 104. doi:10.1186/s13045-018-0647-8

Loeffler, J., Shih, H., & Khandekar, M. (2012). Chapter 45 - Application of Current Radiation Delivery Systems and Radiobiology. In (Third Edition ed., pp. 697-706): Elsevier Inc.

Lu, Y. C., Weng, W. C., & Lee, H. (2015). Functional roles of calreticulin in cancer biology. *Biomed Res Int, 2015*, 526524. doi:10.1155/2015/526524

Luzhna, L., Kathiria, P., & Kovalchuk, O. (2013). Micronuclei in genotoxicity assessment: from genetics to epigenetics and beyond. *Front Genet, 4*, 131. doi:10.3389/fgene.2013.00131

Malamas, A. S., Gameiro, S. R., Knudson, K. M., & Hodge, J. W. (2016). Sublethal exposure to alpha radiation (223Ra dichloride) enhances various carcinomas' sensitivity to lysis by antigen-specific cytotoxic T lymphocytes through calreticulin-mediated immunogenic modulation. *Oncotarget, 7*(52), 86937-86947. doi:10.18632/oncotarget.13520

Martino, S. D., Grescente, G., De Lucia, V., Di Paolo, M., Marotta, G., De Lucia, D., Abbadessa, A. . (2017). The Emerging Role of Calreticulin In Cancer Cells. *World Cancer Research Journal*

Mayles, P., Nahum, A., Rosenwald, J.C. (2007). *Handbook of Radiotherapy Physics, Theory and Practice*. Taylor & Francis Group, LLC.

McHugh, M. K., Lopez, M. S., Ho, C. H., Spitz, M. R., Etzel, C. J., & El-Zein, R. A. (2013). Use of the cytokinesis-blocked micronucleus assay to detect gender differences and genetic instability in a lung cancer case-control study. *Cancer Epidemiol Biomarkers Prev, 22*(1), 135-145. doi:10.1158/1055-9965.Epi-12-0435

Mehta, S. R., Suhag, V., Semwal, M., & Sharma, N. (2010). Radiotherapy: Basic Concepts and Recent Advances. *Med J Armed Forces India, 66*(2), 158-162. doi:10.1016/s0377-1237(10)80132-7

Miszczyk, J., Rawojć, K., Panek, A., Swakoń, J., Prasanna, P., & Rydygier, M. (2015). Response of human lymphocytes to proton radiation of 60 MeV compared to 250 kV X-rays by the cytokinesis-block micronucleus assay. *Radiotherapy and Oncology, 115*. doi:10.1016/j.radonc.2015.03.003

Mosiman, V. L., Patterson, B. K., Canterero, L., & Goolsby, C. L. (1997). Reducing cellular autofluorescence in flow cytometry: an in situ method. *Cytometry, 30*(3), 151-156.

Motwani, M., Pesiridis, S., & Fitzgerald, K. A. (2019). DNA sensing by the cGAS-STING pathway in health and disease. *Nat Rev Genet, 20*(11), 657-674. doi:10.1038/s41576-019-0151-1

Mukherjee, S. (2010). *The Emperor of All Maladies: A biography of Cancer.* . New York: Scribner.

Neely, J. G., Hartman, J. M., Forsen, J. W., Jr., & Wallace, M. S. (2003). Tutorials in clinical research: VII. Understanding comparative statistics (contrast)--part B: application of T-test, Mann-Whitney U, and chi-square. *Laryngoscope, 113*(10), 1719-1725. doi:10.1097/00005537-200310000-00011

Newbold, P., Carlson, W., Thorne, B. . (2010). *Statistics for Business and Economics* (Vol. 8th Edition). England: Pearson.

Nomani, A., Chen, X., & Hatefi, A. (2018). Evaluation of genotoxicity and mutagenic effects of vector/DNA nanocomplexes in transfected mesenchymal stem cells by flow cytometry. *Acta Biomater, 74*, 236-246. doi:10.1016/j.actbio.2018.05.029

Parham, P., & Janeway, C. (2015). *The immune system* (Fourth edition. ed.). New York, NY: Garland Science, Taylor & Francis Group.

Percuoco, R. (2014). *Chapter 1 - Plain Radiographic Imaging* (3 ed.). Saint Louis: Mosby.

Podgoršak, E. B. (2005). *Radiation Oncology Physics: A Handbook for Teachers and Students*. Vienna: International Atomic Energy Agency.

Podgoršak, E. B. (2010). *Radiation Physics for Medical Physicists* Springer Heidelberg Dordrecht London New York.

Rodríguez-Ruiz, M. E., Vanpouille-Box, C., Melero, I., Formenti, S. C., & Demaria, S. (2018). Immunological Mechanisms Responsible for Radiation-Induced Abscopal Effect. *Trends Immunol, 39*(8), 644-655. doi:10.1016/j.it.2018.06.001

Rubner, Y., Muth, C., Strnad, A., Derer, A., Sieber, R., Buslei, R., . . . Gaipl, U. S. (2014). Fractionated radiotherapy is the main stimulus for the induction of cell death and of Hsp70 release of p53 mutated glioblastoma cell lines. *Radiat Oncol, 9*(1), 89. doi:10.1186/1748-717x-9-89

Samstein, R. M., & Riaz, N. (2018). The DNA damage response in immunotherapy and radiation. *Adv Radiat Oncol, 3*(4), 527-533. doi:10.1016/j.adro.2018.08.017

Schaue, D., Ratikan, J. A., & Iwamoto, K. S. (2012). Cellular autofluorescence following ionizing radiation. *PLoS One, 7*(2), e32062. doi:10.1371/journal.pone.0032062

Sommer, S., Buraczewska, I., & Kruszewski, M. (2020). Micronucleus Assay: The State of Art, and Future Directions. *Int J Mol Sci, 21*(4). doi:10.3390/ijms21041534

Stangroom, J. (2020). Mann-Whitney U Test Calculator Retrieved from https://www.socscistatistics.com/tests/mannwhitney/default2.aspx (17.10.2020)

Stein, G. H. (1979). T98G: an anchorage-independent human tumor cell line that exhibits stationary phase G1 arrest in vitro. *J Cell Physiol, 99*(1), 43-54. doi:10.1002/jcp.1040990107

Thermo Fisher Scientific. (2020). TrypLE Reagents. Retrieved from https://www.thermofisher.com/no/en/home/life-science/cell-culture/mammalian-cell-culture/reagents/trypsin/tryple-express.html (23.09.2020)

Thingstad, E. (2019). *Immunogenic calreticulin signaling in lung and glioblastoma cancer cells after x-ray and proton irradiation.* (Master Thesis). University of Oslo,

Thomas, P., & Fenech, M. (2011). Cytokinesis-block micronucleus cytome assay in lymphocytes. *Methods Mol Biol, 682*, 217-234. doi:10.1007/978-1-60327-409-8_16

Tian, X., Liu, K., Hou, Y., Cheng, J., & Zhang, J. (2018). The evolution of proton beam therapy: Current and future status. *Mol Clin Oncol, 8*(1), 15-21. doi:10.3892/mco.2017.1499

Tucker, J. D., Vadapalli, M., Joiner, M. C., Ceppi, M., Fenech, M., & Bonassi, S. (2013). Estimating the lowest detectable dose of ionizing radiation by the cytokinesis-block micronucleus assay. *Radiat Res, 180*(3), 284-291. doi:10.1667/rr3346.1

Universitites, O. R. A. (1999). Coolidge X-ray Tubes. Retrieved from https://www.orau.org/ptp/collection/xraytubescoolidge/coolidgeinformation.htm (24.06.2009) (23.09.2020))

Vallabhajosula, S. (2009). *Molecular imaging - radiopharmaceuticals for PET and SPECT*: Springer-Verlag Berlin Heidelberg.

Varricchio, L., Falchi, M., Dall'Ora, M., De Benedittis, C., Ruggeri, A., Uversky, V. N., & Migliaccio, A. R. (2017). Calreticulin: Challenges Posed by the Intrinsically Disordered Nature of Calreticulin to the Study of Its Function. *Frontiers in Cell and Developmental Biology, 5*(96). doi:10.3389/fcell.2017.00096

Wenstøp, F. (2003). *Statistikk og dataanalyse*. Norway Universitetsforlaget AS

Whitley, E., Ball, Jonathan. . (2002). Statistics review 6: Nonparametric methods. 4. doi:10.1186/cc1820

Wikipedia contributors. (2020a). DBSCAN. Retrieved from https://en.wikipedia.org/w/index.php?title=DBSCAN&oldid=984688632 (20.11.2020)

Wikipedia contributors. (2020b). Otsu's method. Retrieved from https://en.wikipedia.org/wiki/Otsu%27s_method (17.11.2020)

Wynder, E. L., & Graham, E. A. (2005). Tobacco smoking as a possible etiologic factor in bronchiogenic carcinoma. *Bulletin of the World Health Organization, 83*(2), 146-153. Retrieved from https://apps.who.int/iris/handle/10665/269342

Zaorsky, N. G., Churilla, T. M., Egleston, B. L., Fisher, S. G., Ridge, J. A., Horwitz, E. M., & Meyer, J. E. (2017). Causes of death among cancer patients. *Ann Oncol, 28*(2), 400-407. doi:10.1093/annonc/mdw604

Zhou, J., Wang, G., Chen, Y., Wang, H., Hua, Y., & Cai, Z. (2019). Immunogenic cell death in cancer therapy: Present and emerging inducers. *J Cell Mol Med, 23*(8), 4854-4865. doi:10.1111/jcmm.14356

Appendix 1

Table 9: Raw data of the A549 cells running the calreticulin assay. Also, two experiments running the T98G cells has been listed. The flow cytometry is run 48 hours after the last irradiation. When e.g. 12 Gy is written, it means only one fraction was given 48 hours before flow cytometry. When e.g. 6 + 6 Gy is written, it means two fractions each giving a dose of 6 Gy is given with a time interval of 24 hours between each irradiation. Abbreviations: P+S AB = cells have been treated with primary and secondary antibody. SAB only = cells have only been treated with secondary antibody. No AB = cells have not been treated with antibody. Note that experiments which have been outlined are excluded from data analysis, due to e.g. missing cells in the sample or inconsistency in the data.

08.05.2020A	**P+S AB**		**SAB only**		**No AB**	
Dose	12 Gy	Control	12 Gy	Control	12 Gy	Control
	4477	2372	1534	687	1139	495
	3311	1851	1542	634		
	2678	1570	1343	624		
08.05.2020B	P+S AB		SAB only		No AB	
Dose	12 Gy	Control	12 Gy	Control	12 Gy	Control
	2935	1301	2137	864	1374	508
	3204	1453	1873	816		
	3107	1327	2133	898		
30.04.2020A	P+S AB		SAB only		No AB	
Dose	12 Gy	Control	12 Gy	Control	12 Gy	Control
	~~1848~~	~~735~~	~~2133~~	~~828~~	~~1184~~	~~471~~
	~~1929~~	~~746~~	~~2498~~	~~960~~		
	~~2109~~	~~861~~	~~2025~~	~~799~~		
30.04.2020B	P+S AB		SAB only		No AB	
Dose	8 Gy	Control	8 Gy	Control	8 Gy	Control
	7112	3152	1642	761	1008	492

	1791	823	1722	794		
	2272	1021	1254	612		
24.04.2020	P+S AB		SAB only		No AB	
Dose	8 Gy	Control	8 Gy	Control	8 Gy	Control
	6772	3599	1470	791	937	519
	7499	3994	1483	771		
	7033	3906	1472	702		
14.05.2020A	P+S AB		SAB only		No AB	
Dose	4 Gy	Control	4 Gy	Control	4 Gy	Control
	2454	1763	903	659	670	447
	2691	1791	921	595		
	2675	1808	970	638		
14.05.2020B	P+S AB		SAB only		No AB	
Dose	4 Gy	Control	4 Gy	Control	4 Gy	Control
	~~931~~	~~615~~	~~982~~	~~646~~	~~682~~	~~460~~
	~~935~~	~~620~~	~~877~~	~~578~~		
	~~963~~	~~628~~	~~911~~	~~628~~		
22.05.2020A	P+S AB		SAB only		No AB	
Dose	2 Gy	Control	2 Gy	Control	2 Gy	Control
	3112	2380	2412	1819	735	534
	3667	2781	1946	1509		
	3014	2280	2499	1862		
22.05.2020B	P+S AB		SAB only		No AB	
Dose	2 Gy	Control	2 Gy	Control	2 Gy	Control
	2433	1881	886	677	572	416

	2467	1948	827	657		
	2372	1828	858	642		
29.05.2020A	P+S AB		SAB only		No AB	
Dose	4 + 4 Gy	Control	4 + 4 Gy	Control	4 + 4 Gy	Control
	4093	2452	1361	766	836	467
	4631	2809	1237	660		
	3678	2190	1245	668		
29.05.2020B	P+S AB		SAB only		No AB	
Dose	4 + 4 Gy	Control	4 + 4 Gy	Control	4 + 4 Gy	Control
	3883	2364	1674	851	782	438
	4670	2754	2055	1047		
	3672	2077	1787	875		
04.06.2020A	P+S AB		SAB only		No AB	
Dose	2 + 2 Gy	Control	2 + 2 Gy	Control	2 + 2 Gy	Control
	2071	1412	954	660	607	404
	2100	1419	1041	704		
	1811	1232	878	634		
04.06.2020B	P+S AB		SAB only		No AB	
Dose	2 + 2 Gy	Control	2 + 2 Gy	Control	2 + 2 Gy	Control
	2230	1438	948	652	595	433
	2176	1422	1148	771		
	2367	1523	1007	665		
05.06.2020A	P+S AB		SAB only		No AB	
Dose	6 + 6 Gy	Control	6 + 6 Gy	Control	6 + 6 Gy	Control
	3808	1601	1700	724	1099	472

	5102	2025	1443	726		
	3878	2210	1055	452		
05.06.2020B	P+S AB		SAB only		No AB	
Dose	6 + 6 Gy	Control	6 + 6 Gy	Control	6 + 6 Gy	Control
	~~5242~~	~~2966~~	~~1548~~	~~861~~	~~No data~~	~~No data~~
	~~5830~~	~~2517~~	~~1700~~	~~780~~		
	~~5219~~	~~2210~~	~~1055~~	~~452~~		
10.07.2020A	P+S AB		SAB only		No AB	
Dose	6 Gy	Control	6 Gy	Control	6 Gy	Control
	1243	764	1164	708	763	458
	1372	904	1120	740		
	1237	802	1047			
10.07.2020B	P+S AB		SAB only		No AB	
Dose	6 Gy	Control	6 Gy	Control	6 Gy	Control
	~~3266.5~~	~~2027~~	~~1405~~	~~937~~	~~757~~	~~456.5~~
	~~3401~~	~~2350~~	~~No data~~	~~No data~~		
	~~No data~~	~~No data~~	~~No data~~	~~No data~~		
14.07.2020A	P+S AB		SAB only		No AB	
Dose	6 Gy	Control	6 Gy	Control	6 Gy	Control
	2966	2025	1166	741	823	480
	3584	2436	1172.5	714		
	3286	2019	1316	727		
14.07.2020B	P+S AB		SAB only		No AB	
Dose	~~6 Gy~~	~~Control~~	~~6 Gy~~	~~Control~~	~~6 Gy~~	~~Control~~
	~~1103~~	~~665~~	~~1119~~	~~677~~	~~812~~	~~547~~

	~~940~~	~~565~~	~~1092~~	~~654~~		
	~~954~~	~~592~~	~~1097~~	~~654~~		
04.09.2020A	P+S AB		SAB only		No AB	
Dose	4 Gy	Control	4 Gy	Control	4 Gy	Control
	3638	2887	1032	794	687	523
	3546	2714	1036	816		
	3631	2767	991	800		
04.09.2020B	P+S AB		SAB only		No AB	
Dose	4 Gy	Control	4 Gy	Control	4 Gy	Control
	3972	3204.5	988	736	640	496
	4312	3522	886	722		
	4446	3479	883	680		
10.09.2020	P+S AB		SAB only		No AB	
Dose	4 Gy	Control	4 Gy	Control	4 Gy	Control
	2995	2115	914	673	685	486
	2908	2033	935	656		
	2815	1996	906	617		
25.09.2020	P+S AB		SAB only		No AB	
Dose	8 + 8 Gy	Control	8 + 8 Gy	Control	8 + 8 Gy	Control
	6593	3020	1759	676	1391	488
	5875,5	2711	1750	651		
	6122	2863	1727	631		
20.10.2020	P+S AB		SAB only		No AB	
Dose	8 + 8 Gy	Control	8 + 8 Gy	Control	8 + 8 Gy	Control
	5673	2614	1455	586	1328	497

	5313	2415	1410	558		
	4294	2004	1389	578		
Calreticulin assay run on T98G cells						
03.09.2020A	P+S AB		SAB only		No AB	
Dose	8 Gy	Control	8 Gy	Control	8 Gy	Control
	3462	5247	1050	940	803	690
	2453	4527	942	971		
	2314	4799	1038	965		
03.09.2020B	P+S AB		SAB only		No AB	
Dose	8 Gy	Control	8 Gy	Control	8 Gy	Control
	2162	2509	1102	985	671	698
	2372	3269	1004	1040		
	1929	2714	1066	1127		

Appendix 2

The following is the final protocol developed for the CBMN assay to be used for future CBMN experiments.

CBMN – assay for confocal microscopy

1. 5×10^4 cells are seeded in coverglass flask 24h prior to treatment
2. Treatment: Irradiation
3. Cytochalasin B added to cell cultures at a final concentration of 3 µg/ml directly after irradiation
4. Fix and stain nuclei (NucSpot 650) and membranes (CellBrite Fix 488):
   a. Remove medium.
   b. Wash twice with PBS (37℃).
   c. Add 1 mL working solution (1X in PBS) of CellBrite 488 (37℃) to flask.
   d. Incubate at 37℃ for 30 min.
   e. Wash twice with PBS (37℃).
   f. Fixate with 2 mL methanol/glacial acetic acid (3:1).
   g. Incubate 10 min.
   h. Wash twice with PBS.
   i. Add 1 mL NucSpot in PBS (1 µL/mL).
   j. Incubate 10 min.
   k. Remove NucSpot.
   l. Break flask of cover glass and let the cells dry.
5. Mount with approximately 5 - 10 µL VectaShield Mounting Medium. Add cover slip and use nail polish to fix it on the glass. Shield from light.
6. Image with CLSM

Stock dilution of Cyt-B

Cytochalasin B from *Drechslera dematioidea*, ≥98 % (HPLC), powder (#C6762, Sigma-Aldrich)

Dissolve 1 mg Cyt-B solid in 1.67 ml DMSO to give a Cyt-B solution concentration of 600 mg/ml as follows:

(1) Remove the Cyt-B vial from -20 ◦C and allow to reach room temperature. Do not remove the seal.

(2) Sterilize the top of the rubber seal with ethanol and allow the ethanol to evaporate.

(3) Pipette 1.67 ml of DMSO into a 50 ml sterile Falcon tube.

(4) Vent the vial seal with a 25 G needle and a 0.2 mm hydrophobic filter to break the vacuum.

(5) Using a 1/2 ml sterile syringe and another needle, inject 0.8ml of the 1.67 ml DMSO through the seal.

(6) Mix contents gently. Cyt-B should dissolve readily in DMSO. Leave syringe and needle in place.

(7) Remove the 4 ml from the vial into the syringe and eject into a labeled sterile tube.

(8) Aspirate the remaining 0.87 ml of DMSO into the syringe and inject into the vial as before.

(9) Remove this final volume from the vial and eject into the labeled tube.

(10) Mix and dispense 100 µl aliquots into sterile, 5 ml polystyrene capped tubes (5 mL flow tubes or 10mL polystyrene tubes in drawer in lab behind kitchen) labeled Cyt-B with the date.

(11) Store at -20°C for up to 12 months. The vials of powder are guaranteed by Sigma for 2 years if stored at -20°C.

1

Vent vial with 25G needle and 0.2µm hydrophobic sterile filter.

2

Sterile filter 1.67ml DMSO

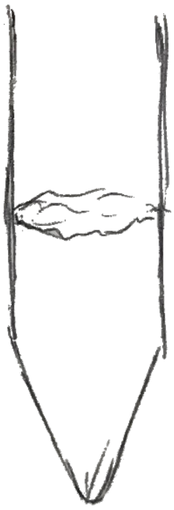

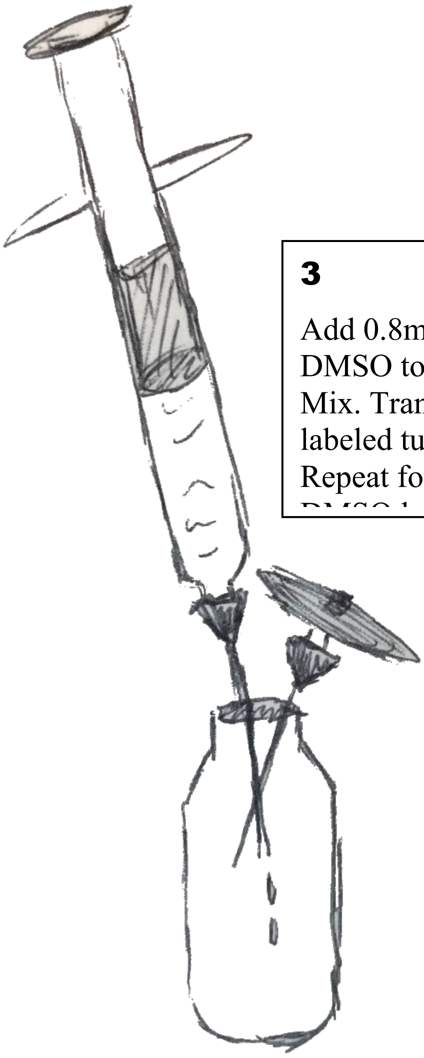

3

Add 0.8ml of the DMSO to vial. Mix. Transfer to labeled tube. Repeat for

4

1.67ml DMSO with 600µg/ml Cyt-B.

Distribute in 50µg/100µg

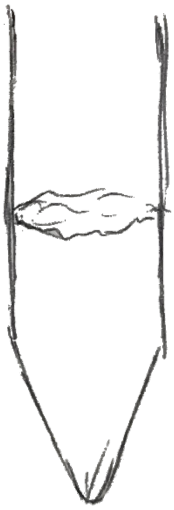

Appendix 3

The following is the final protocol developed for the calreticulin assay used for the experiments in this thesis.

CRT assay for flow cytometry

Compound	Amount/sample (3 T25)	Amount/control (1 T75)	Amount/total
PBS	150 ml	30 ml	180 mL
PBS w/BSA	1100 µl	-	1100 µL
TrypLE	6 ml	4 ml	10 mL
Medium	12 ml	11 ml	23 mL
DyLight	-	3 µl/350 µl medium	-
Primary antibody	1,75 µl in 350 µl PBS w/BSA (0,5 µL/100 µL PBS w/BSA)	-	-
Secondary antibody	1,75 µl in 700 µl PBS w/BSA (0,25 µL/100 µL PBS w/BSA)	-	-

Barcoding with ***DyLight 488 NHS-Ester dye***:

Stock: 50 µg dissolved in 30 µl DMSO (500 µg/100µL), vials á 3 µl stored at -20°C.

Mix stock solution in original vial and use several steps of centrifuge and vortex to ensure good mixture.

Primary antibody **Anti-Calreticulin antibody (ab2907), rabbit polyclonal (Freezer)**

Secondary antibody **Alexa Fluor 647 goat anti-rabbit IgG (H+L) (Fridge)**

PBS and Medium at room temperature

Ice from Ice machine

1. **Harvest control** (1 T75)

   Remove medium

Flush with 7.5 ml PBS (room temp.)

Add 4 ml TrypLE, flush a few times and incubate for about 4 min

Suspend to single cells with 2 ml pipette

Add 10 ml medium and transfer to tube.

Centrifuge 200xg, 4 min

2. **Stain control**

   Make dye mix: 3 µl in 350 µl medium.

   Aspirate supernatant and resuspend the cell pellet in dye mix. Mix well, avoid making foam.

   Incubate in dark with aluminum foil for 30 minutes, at room temperature.

3. **Harvest sample** (3 T25)

   Remove medium

   Flush with 5 ml PBS

   Add 2ml TrypLE, flush a few times and incubate for about 4 min

   Suspend to single cells with 2 ml pipette

   Add 4 ml medium and transfer to tube.

   Centrifuge 200xg, 4 min

   Aspirate and resuspend in 10 ml PBS

4. **Wash and distribute stained control**

   Add PBS to the DyLight stained control up to 10 ml

   Centrifuge 200 xg, 4 min.

   Aspirate.

   Add 10 ml PBS and mix, centrifuge and aspirate again.

   Resuspend in (number of samples x 100 µl + 50 µl) PBS

   Add 100 µl to each sample. Mix well.

5. **Split samples in two**

   Split each sample so each have a secondary antibody control.

   Fill three tubes with 5 mL PBS first.

   Add 5 mL of sample to each.

   Add 5 mL PBS to original sample tubes.

You now have 6 sample, 3 shall have primary + secondary antibody, 3 will only have secondary antibody.

Centrifuge 200 xg, 4 min, put on ice and aspirate before adding primary antibody.

6. **Primary Antibody**

   Mix: number of samples x (0, 5 µl primary ab/100 µl PBS w/BSA).

   - 3 sample: add 1,75 µl to 350 µl PBS w/BSA.

   Add mix to the 3 samples and add 100 µl PBS w/BSA to the secondary ab controls.

   Incubate in dark for 30 min on ice.

7. **Wash**

   Add 3ml PBS to each sample, centrifuge 200 xg, 4 min.

   Aspirate supernatant.

   Repeat once more.

8. **Secondary Antibody**

   Mix: number of samples x (0,25 µl primary ab/100 µl PBS w/BSA).

   - 3x2 = 6 sample: add 1,75 µl to 700 µl

   Resuspend all pellets in 100 µl mix.

   Incubate in dark for 30 minutes on ice.

9. **Wash**

   Add 3ml PBS to each sample, centrifuge 200 xg, 4 min.

   Aspirate supernatant.

   Repeat once more.

   Resuspend the pellets in 250 µl PBS and store at 4°C until flow cytometry analysis.

10. **Live/dead staining, filtering and flow analysis**

    Prior to flow cytometry analysis, add 0.5µl propidium iodine (PI) 1.0 mg/ml to the samples for live/dead staining, right before filtering into tubes and running flow.

Abbreviation	Name	Substance	Channel
PA	Primary Antibody	Anti-Calreticulin antibody (ab2907), rabbit polyclonal	

SA	Secondary Antibody	Alexa Fluor 647 goat anti rabbit IgG (H+L)	FL4
BC	Barcooding	Dylight 488 NHS-Ester dye	FL1
PI	Live/Death	Propidium iodide solution	FL2, FL3

Appendix 4

Table 10: The different concentrations of DyLight 488 tested in the experiments performed during the work of this thesis. Excluding the first experiment, 8 Gy X-ray irradiation was used. When increasing the concentration of the DyLight 488 from 0.25 µg/100 µl medium to 1.42 µg/100 µl medium (almost increasing the concentration six times), it was possible to distinguish the control cells from the irradiated cells. Note that in the experiments performed to test for different concentrations needed for the DyLight, Julia Marzioch and Anne Marit Rykkelid helped with the experiments.

Stock solution	Amount of DyLight in control cells	Final concentration	Dose (X-ray)	Comment
25 µg dissolved in 100 **µl DMSO**	3.5 µl DyLight/350 µl medium	0.25 µg/100 µl	2 Gy	Tested one time
25 **µg** dissolved in 100 **µl DMSO**	7 µl DyLight/350 µl medium	0.49 µg/100 µl	8 Gy	Tested three times
25 **µg** dissolved in 100 **µl DMSO**	3.5 µl DyLight/350 µl PBS w/BSA	0.25 µg/100 µl	8 Gy	Tested one time
25 **µg** dissolved in 100 **µl DMSO**	3.5 µl DyLight/625 µl medium	0.14 µg/100 µl	8 Gy	Tested two times
167 **µg** dissolved in 100 **µl DMSO**	3 µl DyLight/350 µl medium	1.42 µg/100 µl	8 Gy	Tested one time
500 **µg**/100 **µl**	1 µl DyLight/350 µl medium	1.42 µg/100 µl	8 Gy	Tested two times
500 **µg**/100 **µl**	3 µl DyLight/ 350 µl medium	4.25 µg/100 µl	8 Gy	Tested one time
500 **µg**/100 **µl**	5 µl DyLight/350 µl medium	7.04 µg/100 µl	8 Gy	Tested one time

Appendix 5

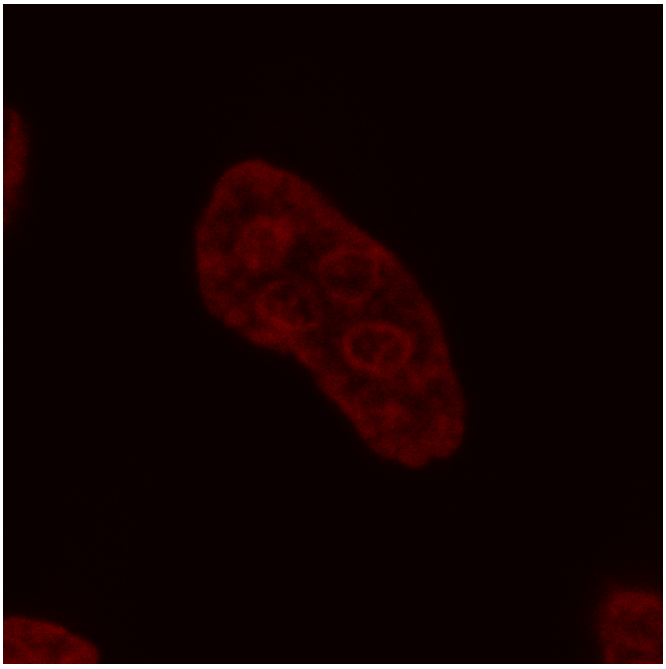

Figure 48: Unedited version of Figure 34.

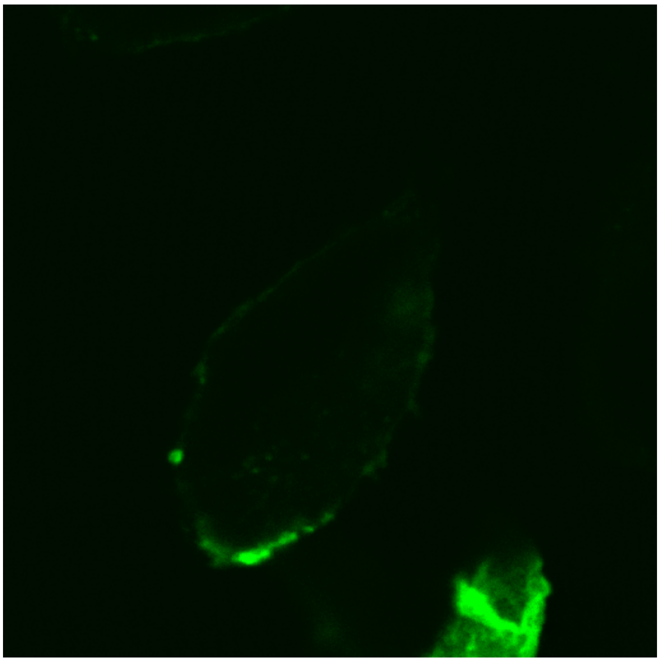

Figure 49: Unedited version of Figure 35.

Appendix 6

Table 11: A detailed list of the calreticulin (CRT) experiments done at the cell lab with comments. The X-ray irradiation was done 48 hours before the assay began. Unless explicitly stated, only one fraction of irradiation was given.

Type of assay	Number	Date	Comment
CRT	1	12.09.2019	Assay with Anne Marit Rykkelid, protocol development
CRT	2	02.10.2019	Abrupted mid-way, protocol development
CRT	3	24.10.2019	Protocol development
CRT	4	29.10.2019	Protocol development
CRT	5	04.11.2019	Protocol development
CRT	6	06.11.2019	Protocol development
CRT	7	13.11.2019	Protocol development
CRT	8	15.11.2019	Assay with Nina F. J. Edin, protocol development
CRT	9	06.02.2020	Protocol development
CRT	10	16.02.2020	Changed the volume of barcoded cells added to sample, Protocol development
CRT	11	20.02.2020	Changed the stock solution of DyLight: 500 µg/100 µl, Protocol development with Julia Marzioch
CRT	12	04.03.2020	Repeated experiment from 20.02.2020, Protocol development
CRT	13	23.04.2020	8 Gy
CRT	14	30.04.2020	12 Gy
CRT	15	30.04.2020	8 Gy
CRT	16	08.05.2020	12 Gy

CRT	17	08.05.2020	12 Gy
CRT	18	14.05.2020	4 Gy
CRT	19	14.05.2020	4 Gy
CRT	20	22.05.2020	2 Gy
CRT	21	22.05.2020	2 Gy
CRT	22	29.05.2020	2 fractions, 4 Gy (8 Gy total)
CRT	23	29.05.2020	2 fractions, 4 Gy (8 Gy total)
CRT	24	04.06.2020	2 fractions, 2 Gy (4 Gy total)
CRT	25	04.06.2020	2 fractions, 2 Gy (4 Gy total)
CRT	26	05.06.2020	2 fractions, 6 Gy (12 Gy total)
CRT	27	05.06.2020	2 fractions, 6 Gy (12 Gy total)
CRT	28	10.07.2020	6 Gy
CRT	29	10.07.2020	6 Gy
CRT	30	14.07.2020	6 Gy
CRT	31	14.07.2020	6 Gy
CRT	32	03.09.2020	8 Gy, T98G cells
CRT	33	03.09.2020	8 Gy, T98G cells
CRT	34	10.09.2020	4 Gy
CRT	35	25.09.2020	8 + 8 Gy, assay performed by Anne Marit Rykkelid
CRT	36	20.10.2020	8 + 8 Gy, assay performed by Anne Marit Rykkelid

Appendix 7

Table 12: A list of experiments during the protocol development of the CBMN assay. Abbreviations: PI = propidium iodide, RNA = ribonucleic acid.

Date	Comment
22.11.2019	Assay with Ingunn Hanson to test the assay using NucSpot
04.12.2019	Used PI and RNase instead of NucSpot
04.02.2020	Used NucSpot 650, the staining did not work
07.02.2020	Used NucSpot 650 only, and CellBrite488, and RNase
11.02.2020	Repeated experiment from 07.02.2020, with less saturation when obtaining images of the cells
18.02.2020	Used NucSpot 650 only
25.02.2020	Used NucSpot 650 and Cytochalasin-B
26.02.2020	Used NucSpot 650. The cells moved, could not be analyzed
29.04.2020	Testing for membrane staining with CellBrite488 (no results)
29.04.2020	Testing for membrane staining with CellBrite488 (no results)
06.05.2020	Testing for membrane staining with CellBrite488
06.05.2020	Testing for membrane staining with CellBrite488, not using Trypsin

Appendix 8

Table 13: The autofluorescence level in the FL-4 channel after X-ray irradiation of the A549 cells.

See the text for further details on how the ratio of the autofluorescence was calculated. No AB means that no antibody was added to the cell suspension.sss

	FL-4 Channel		
22.05.2020A	No AB		Ratio
Dose	2 Gy	Control	-
	735	534	1.4
22.05.2020B	No AB		-
Dose	2 Gy	Control	-
	572	416	1.4
14.05.2020A	No AB		-
Dose	4 Gy	Control	Ratio
	670	447	1.5
04.09.2020A	No AB		-
Dose	4 Gy	Control	Ratio
	687	523	1.3
04.09.2020B	No AB		-
Dose	4 Gy	Control	Ratio
	640	496	1.3
14.07.2020A	No AB		-
Dose	6 Gy	Control	Ratio
	823	480	1.7
10.07.2020A	No AB		-
Dose	6 Gy	Control	Ratio

	763	458	1.7
30.04.2020B	No AB		-
Dose	8 Gy	Control	Ratio
	1008	492	2.0
24.04.2020	No AB		-
Dose	8 Gy	Control	Ratio
	937	519	1.7
08.05.2020A	No AB		-
Dose	12 Gy	Control	Ratio
	1139	495	2.3
08.05.2020B	No AB		-
Dose	12 Gy	Control	Ratio
	1374	508	2.7

Appendix 9

Table 14: The relative fluorescence intensity of the A549 cells after X-ray irradiation with standard error, given either as one or two fractions.

1 fraction	
Dose	**Relative Fluorescence Intensity**
2 Gy	1.28 +/- 0.02
4 Gy	1.35 +/- 0.03
6 Gy	1.42 +/- 0.04
8 Gy	2.11 +/- 0.12
12 Gy	1.81 +/- 0.13
2 fractions	
Dose	**Relative Fluorescence Intensity**
2 + 2 Gy	1.55 +/- 0.02
4 + 4 Gy	1.56 +/- 0.02
6 + 6 Gy	2.37 +/- 0.12
8 + 8 Gy	2.04 +/- 0.02